University of Nevada, Reno

Thermal Analysis and Experiment Design for Seismic Performance Evaluation of Ice and Water Contaminated Friction Pendulum Bearings

A thesis submitted in partial fulfillment of the
requirements for the degree of Master of Science in
Civil and Environmental Engineering

by

Rolando Grijalva Alvarado

Dr. Keri L. Ryan/Thesis Advisor

August, 2021

THE GRADUATE SCHOOL

We recommend that the thesis
prepared under our supervision by

Rolando Grijalva Alvarado

entitled

Thermal Analysis and Experiment Design for Seismic Performance Evaluation of Ice and Water Contaminated Friction Pendulum Bearings

be accepted in partial fulfillment of the
requirements for the degree of

MASTER OF SCIENCE

Keri L. Ryan, Ph.D
Advisor

Floriana Petrone, Ph.D
Committee Member

Mustafa Hadj Nacer, Ph.D
Graduate School Representative

David W. Zeh, Ph.D., Dean
Graduate School

August, 2021

Abstract

Thermal Analysis and Experiment Design for Seismic Performance Evaluation of Ice and Water Contaminated Friction Pendulum Bearings

Over the past few years, there have been several reports on water contaminated Friction Pendulum System (FPS) bearings across the country. Additionally, there is a concern in Alaska that water will freeze inside the bearing during the winter, potentially restraining the slider from moving along the bottom concave surface. The motivation for this project comes from the lack of experimental work to examine the effects of ice and water in FPS bearings.

The objectives of the project are to assess the influence of water and ice contamination on the frictional properties and seismic response of FPS bearings, relative to uncontaminated bearings. This assessment may lead to modified analytical models to account for the effects of water and ice contamination, and recommendations to account for water and ice contamination in the design process and/or recommendations for mitigation. However, the scope of this thesis includes test setup and load frame design for shake table tests; and analysis and experiments to assess the feasibility, optimize the insulation arrangement, and estimate the time needed to freeze the water to a temperature of -30°F (239°K).

A steel test frame was designed to transmit axial load to the bearing and to restrain the top plate of the bearing from displacement in all directions. The test frame consists of three pieces that form an “A”: 2 legs that are connected to rigid steel columns by a pin to

allow for rotation, and 1 middle element that transmit axial load to the bearing. The frame was designed in accordance to AISC 360 to transmit an axial load of 100 kips to the bearing and to withstand a shear force of 23 kips, calculated using the maximum displacement capacity (11 in.) of Susitna Bridge bearing.

A thermal finite volume model was developed to simulate the freezing process of a water-filled bearings placed inside an insulation box filled with dry ice. Two different approaches were used to model dry ice's cooling capacity: Source Term and Temperature BC. In addition, two freezing tests were conducted to validate the results from the finite volume model.

The freezing tests revealed that Source Term approach underestimates the dry ice cooling capacity while Temperature BC overestimates dry ice cooling capacity. Air gaps must be minimized in the final design of the insulation box, and insulation must be added above and below the bearing to achieve temperatures below -30°F or lower. The freezing tests also revealed that the insulation box needs to be refilled with dry ice after the water has changed phase from liquid to solid.

Acknowledgements

This study was sponsored and funded by Alaska Department of Transportation (DOT). Any opinions, finding and recommendations expressed in this material are mine and do not necessarily express those of Alaska DOT. I am grateful for this research funding and support for my education.

I would like to show my gratitude to my advisor Dr. Keri Ryan for the opportunity to work on this project. She has been a mentor that guided me during my graduate program, I have learn a lot from her in the past two years. Thank you for your support.

I would also like to thank Dr. Mustafa Hadj Nacer for his valuable guidance during this project and Dr. Floriana Petrone for her feedback and support. I also acknowledge Leslie Daugherty, Anna Bosin and the rest of Alaska DOT staff for their valuable feedback. And finally I would like to thank my colleagues from the graduate program for all the help along this past two years.

Table of Contents

List of Tables

List of Figures

Chapter 1. Introduction

1.1. Problem Statement

Seismic isolation is a passive earthquake protection concept that has been widely used to improve the performance of buildings and bridges subjected to seismic loads. In bridges, seismic isolation devices between the bridge piers and superstructure lengthen the natural period of the structure, thus reducing the spectral acceleration demands.

A spherical sliding bearing is a seismic isolation device composed of a top plate, a bottom plate and one or more spherical sliding surface(s). When the device is subjected to lateral force demands, sliding occurs and energy is dissipated through friction between the slider(s) and the spherical sliding surface(s); hence, the effectiveness of these devices depends directly on their friction properties. This study will focus on Friction Pendulum System (FPS) bearings, which are spherical sliding bearings manufactured by Earthquake Protection Systems.

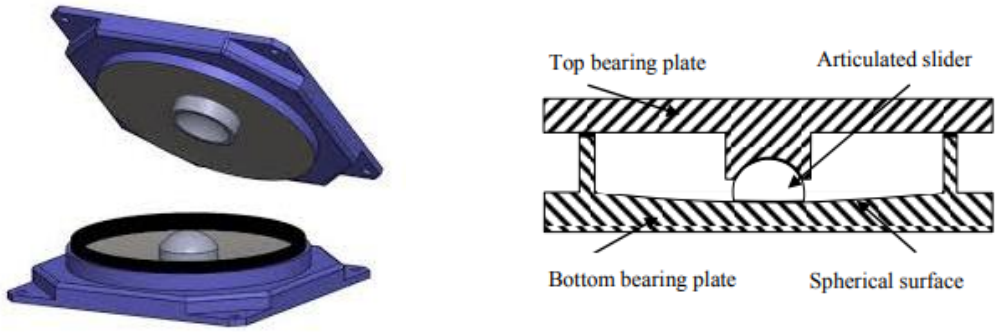

(a) (b)

Figure 1.1. Single pendulum bearing (a) 3D view and (b) section view (Gillich et al, 2018)

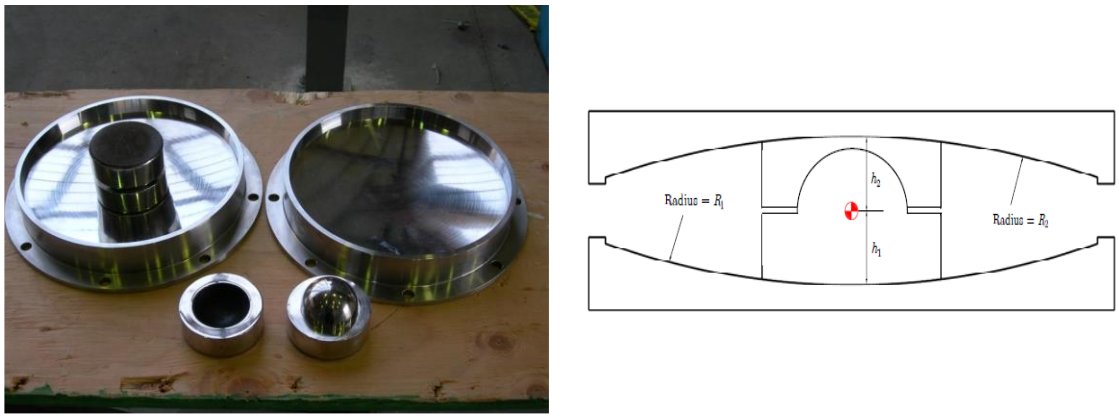

(a) (b)

Figure 1.2. Double pendulum bearing (a) Disassembled and (b) section view (Morgan and Mahin, 2011)

There are several types of FPS bearings. Single pendulum bearings (SPB) and double pendulum bearings (DPB) are the focus of this study. SPBs have only one sliding surface. As shown in Figure 1.1, sliding between the bottom spherical surface and the slider. The top plate is fixed to the slider, hence moving along with it. The DPBs have two independent sliding surfaces (Figure 1.2), one on top of the slider and another one below the slider. The slider moves along the bottom spherical surface and the top spherical sliding plate moves relative to the slider. To achieve a comparable displacement capacity, DPBs are more compact than SPBs since displacements occur on two sliding surfaces.

Several factors influence the friction characteristics of FPS bearings, such as lubrication, slide velocity, pressure, temperature, surface roughness, contamination, corrosion, load dwell and cumulative travel. These effects are generally well known and are described in more detail in Section 2.1. One factor that has not been addressed adequately in the literature is water contamination. Water can turn to ice in cold climates. Frozen water may obstruct the movement of the bearing, and the resulting shear demand

increase to a point that could be damaging for the structure. There is growing concern about how friction characteristics and the overall response of FPS bearings will be affected by such water or ice contamination. Alaska Department of Transportation and Public Facilities (DOT&PF) have reported water contamination in several SPB and DPB bearings from Susitna River Bridge, Nenana River Bridge and Robertson River Bridge. Figure 1.3 shows water contamination in a bridge in Alaska.

Figure 1.3. Water contamination in Alaska bridge (Alaska DOT, 2019)

The consequences of water and ice contamination in the bearings must be studied to determine their effects on the seismic performance of the devices, and to develop procedures to account for these effects in the design process. Also, mitigation options should be explored.

1.2. Scope and Objectives

To date, almost no experimental work has been conducted to examine the effects of ice and water contamination in FPS or generally in spherical sliding bearings. In this project, the seismic response of 1 SPB and 3 DPB will be evaluated under dry, wet and frozen conditions. The goal of the testing is to characterize how water and ice contamination affects FPS bearings performance. One bearing at a time will be placed within a setup on the shake table and constrained by a load frame on top. The shake table will be used as an actuator to apply cyclic and earthquake loading. For all tests, a controlled axial load will be applied to the bearing using an hydraulic ram and transmitted through the load frame.

Other long term objectives of this research are: 1) to develop modified analytical models to account for the effects of water and ice contamination on the bearing friction properties, 2) to investigate the response of isolated bridges under water and ice contamination relative to uncontaminated bearings, and 3) provide recommendations to account for contamination in the design process and/or provide mitigation recommendations.

In order to achieve a realistic representation of ice contamination in the bearings, an efficient way of freezing water within the bearing in situ (within the test setup) must be developed. The scope of this thesis includes a detailed literature review on variables that affect frictional properties of the spherical sliding bearings, water and ice contamination effects on friction surfaces and ice physical properties that are relevant to understand how ice contamination may affect FPS bearings response. This thesis includes a finite volume

model that simulates the heat transfer occurring in the bearing as it is being cooled down, prior to shake table test, in order to be able to assess the feasibility of different insulation and cooling arrangements. Part of the scope of this thesis is also a pre-freezing test conducted on one of the bearings to validate the results from the simulation.

Chapter 2. Literature Review

The seismic performance of FPS bearings depends on the frictional properties of the devices. Hence, the effects of different variables on frictional properties are reported in this chapter. Such variables include temperature, sliding velocity, lubrication, apparent pressure, corrosion and load dwell. As little information on the effects of ice and water contamination on FPS bearing performance can be found, the effects of water lubrication on frictional properties of general steel – PTFE interfaces and ice general physics are also reviewed.

2.1. Prior Documented Influences on Friction in Spherical Sliding Bearings

A thorough study on variables that affect friction, and how these variables influence the behavior of friction pendulum bearings, was conducted by Constantinou et al (2007). The most relevant findings regarding frictional behavior of spherical sliding bearings are summarized below.

Friction is defined as the resistance to movement of one body relative to another. For a sliding bearing, the friction force is directly proportional to the normal force *N*:

$$F = \mu N \tag{2.1}$$

where μ is the friction coefficient. There are four main sources of friction in sliding bearings: adhesion, plowing, third body effects and viscoelastic effects. Adhesion refers to an atomic bond between two solids materials when they come into contact. The regions of contact between the surfaces are referred to as junctions, and friction by adhesion is the

product of the real contact area and the shear strength of the junctions. When surfaces come into contact, their asperities are subjected to elastic and plastic deformation. The plowing component of friction is the energy dissipated by plastic deformation. Third body effects are generated when the slider contacts other particles that contribute to the friction in the sliding interface. Third body effects play an important role when the bearing is contaminated with debris and other particles, as will be discussed in more detail later. When a hard material slides over a viscoelastic material (e.g. stainless steel (SS) sliding over polytetrafluoroethylene (PTFE)), energy is dissipated through deformation of the viscoelastic material, contributing another component to friction.

The coefficient of friction depends on the materials of the slider and its sliding surface. The most common interface for spherical sliding bearings is PTFE – polished SS. Some bimetallic interfaces have been used in the past as well, such as SS – bronze, steel – steel and bronze – bronze. This report focuses on PTFE – polished SS interfaces. There are several types of PTFE materials and composites. Unfilled PTFE refers to virgin or pure PTFE, without any other material or component added. Filled PTFE refers to PTFE mixed or filled with some other material (e.g. glass or carbon). Another form of PTFE used in FPS bearings is woven PTFE, which is made from unfilled PTFE threads woven into a fabric in a manner similar to weaving other synthetic materials into fabric.

2.1.1. Lubrication Effects

Lubrication reduces the coefficient of friction. Spherical sliding bearings are generally lubricated by grease stored in dimples under hydrostatic pressure. Lubricated

bearings have the same response as nonlubricated bearings at the beginning of movement. After some movement, the coefficient of friction drops due to the spread of the lubricant from the dimples along the sliding surface (Constantinou et al., 2007).

Like unlubricated bearings, the friction in lubricated bearings is velocity dependent. The sliding coefficient of friction for an unfilled and unlubricated PTFE sliding surface is about 1.7 times higher than for a lubricated PTFE sliding surface. Dolce et al. (2005) reported that velocity has little effect on the coefficient of friction for lubricated bearings.

Generally, as temperature decreases, the coefficient of friction increases. This low temperature effect is more notable in lubricated bearings because the friction is lower on lubricated surfaces, leading to less frictional heating. With less frictional heating, the temperature on the sliding surfaces of lubricated bearings will be lower than on unlubricated bearings.

2.1.2. Friction Dependence on Sliding Velocity

Two types of friction are generated in sliding bearings: static or breakaway friction and sliding friction. The breakaway friction is the force that needs to be overcome to start movement, while the sliding friction is the friction generated during motion, which is velocity dependent. After movement starts, the friction coefficient generally drops to a value of f_{min}; then, as velocity increases, friction increases up to a value of f_{max} (Fig. 2.1).

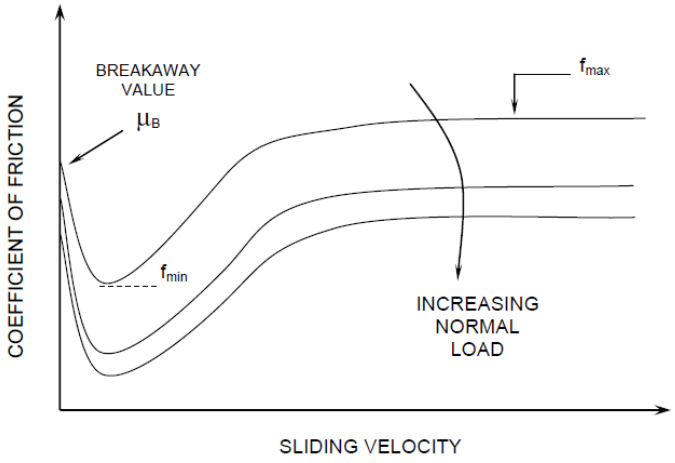

Figure 2.1. Coefficient of friction dependence on sliding velocity (Constantinou et al., 2007)

Mokha et al (1988, 1990) and Constantinou et al. (1990) reported the ratio of breakaway friction μ_B to f_{min} in spherical sliding bearings to be in the range of 1.3 to 1.4 for PTFE–polished SS surfaces. Tests from Campbell et al (1991) on PTFE–polished SS surfaces showed μ_B/f_{min} to range from 2.0 to 7.0. Mokha et al. (1990) and Campbell et al. (1991) also reported that for woven PTFE, μ_B/f_{min} ranged from 2.0 and 3.0. In general, μ_B/f_{min} is of the order of 1.20 for the filled PTFE used in FPS bearings with PTFE–polished SS surfaces. According to tests from Constantinou et al. (1993) and Tsopelas et al. (1996), the sliding friction at large velocities f_{max} is higher than the breakaway friction μ_B.

Mokha et al. (1988) and Constantinou et al. (1990) developed the following equation to describe the dependence of the coefficient of friction on sliding velocity *V*, for a constant value of apparent pressure:

$$\mu = f_{max} - (f_{max} - f_{min})e^{-aV} \qquad (2.2)$$

where a ranges from 20 to 30 s/m for unfilled PTFE and is about 100 s/m or larger for filled PTFE. According to Equation (2.2), the friction coefficient μ ranges from f_{min} at zero

velocity to f_{max} at peak velocity, which means it does not represent the initial effect of the breakaway friction. The transition between f_{max} and f_{min} is determined by the coefficient a. For a lower value of a, a higher velocity is needed to reach an asymptotic behavior tending to f_{max}. The minimum a = 20 s/m implies that the friction coefficient μ tends to its maximum f_{max} for sliding velocities no larger than 150 mm/s (Equation 2.2). The increase in sliding friction f_{max} above f_{min} depends on the sliding velocity, but is normally, for seismic applications, about 5 or 6 times f_{min} (Constantinou et al. 2007).

2.1.3. Effect of apparent pressure

From adhesion theory, Constantinou et al. (2007) deduced the following equation relating friction coefficient to pressure, for a PTFE sliding surface:

$$\mu = \frac{s_0}{p_r} + \alpha \tag{2.3}$$

where s_0 is the minimum shear strength at the interface, p_r is the pressure in the real area of contact and α is a constant that relates shear strength with pressure. In Equation 2.3, friction is assumed to be proportional to shear strength and inversely proportional to pressure. The real area of contact is assumed to be approximately the same as apparent or gross area (A_o) of contact due to plastic deformation of the surface that is produced by a high normal load, as expected in bridge bearings. Noting that p_r is the ratio between normal load N and A_o, if α is very small compared to $\frac{s_0}{p_r}$ in Equation (2.3), the relationship between $1/\mu$ and N/A_o is linear for a fixed area of contact. Hwang et al. (1990) was the first to observe the linear relationship between $1/\mu$ and N/A_o based on data from Taylor (1972)

and Long (1974). Figure 2.2 shows the inverse linear relation between sliding coefficient of friction μ and apparent pressure N/A_o as recorded from different authors.

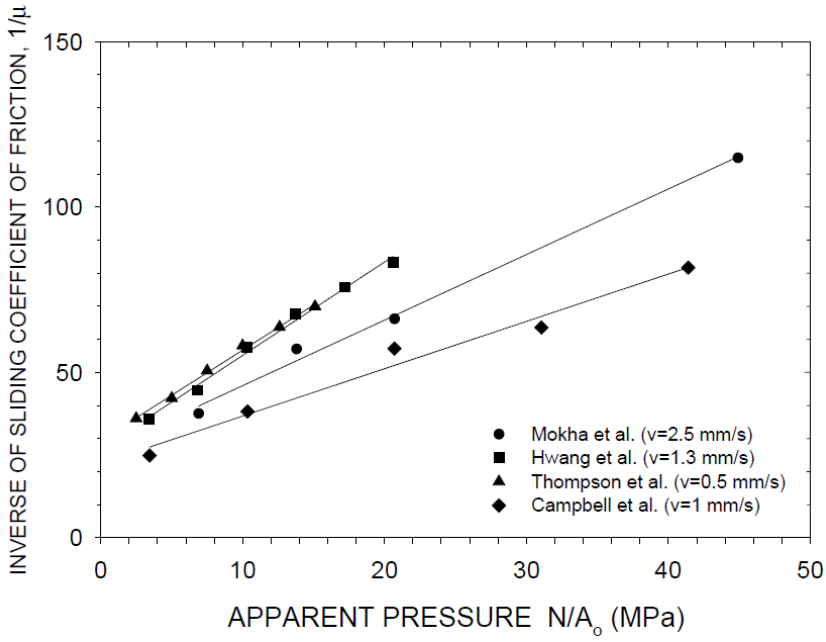

Figure 2.2. Coefficient of friction dependence on apparent pressure (Constantinou et al., 2007)

2.1.4. Effects of Temperature

Temperature greatly influences breakaway friction and coefficients of friction at very low velocities, but due to frictional heating, has a much smaller effect on sliding friction at high velocities (Campbell et al. 1991). Constantinou et al. (1999) conducted tests on spherical sliding bearings with unfilled and filled PTFE sliding interfaces, at temperatures ranging from -40°C to 50°C. Each specimen was subjected to a continuous normal load of 147 kN for 311 hours before testing. To perform the cold temperature tests, the bearing in its test rig was surrounded by an insulating box. Before testing, the box was filled with dry ice, and chilled for five hours until the bearing reached a stable temperature

of -42°C. To measure temperature, thermocouples were embedded in the stainless steel plate. After the stable temperature was reached, the insulating box was removed and the test was performed. At the end of the test, the temperature was -32°C, so the bearing was chilled down to -39°C and another test was conducted. This procedure was repeated 9 times, with the same conditions. To test at high temperatures, heating elements were installed around the test rig. For all tests, the bearing was not contaminated and was in dry conditions, with relative humidity of the environment reported to be about 20%. For high velocities, the values of sliding friction coefficient increased by 60% as temperature decreased from 50°C to -40°C. On the other hand, the sliding friction coefficient at low velocities increased by about 400 to 500% with decreasing temperature, within the same temperature bounds. Figure 2.3 illustrates the effect of temperature for low and high velocities (Constantinou et al. 1999).

For an unfilled PTFE-SS interface, f_{max} varied from 0.113 to 0.118 at 22°C, and increased to 0.178 to 0.189 at -39°C (Constantinou et al. 1999). The same test was also conducted for a bearing with a filled PTFE - SS interface. The tests on unfilled PTFE were conducted in the months of January and February while tests on filled PTFE were conducted in April and May, with a relative humidity in the lab of 20% and between 25 and 40%, respectively. By comparison, the effect of temperature is even more notable for filled PTFE than unfilled PTFE, because the heat flux in filled PTFE is greater than the heat flux in unfilled PTFE. The heat flux was concluded to be greater in filled PTFE because the temperature measured in the thermocouples was lower, suggesting that most of the heat went to the filled PTFE and not into the steel plate. Constantinou et al. (1999)

mentions that the increased heat flux observed in filled PTFE may be due to the minimal thickness of the filled PTFE (0.25 mm).

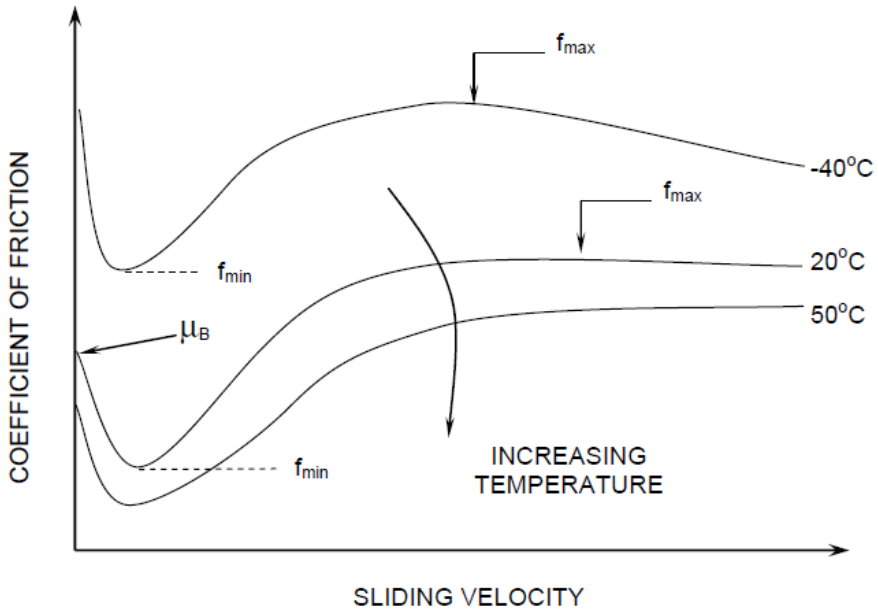

Figure 2.3. Effect of temperature on frictional properties of PTFE–polished SS interfaces (Constantinou et al., 2007)

2.1.5. Contamination

Contamination of the bearing with debris, for example, increases friction due to third body effects and corrosion of the SS surface. Contamination may affect the friction considerably. The effect of contamination is greater in lubricated than unlubricated bearings since contamination interferes with the spread of the lubricant. According to Constantinou et al (2007), contamination is very unlikely when bearings are delivered to the site pre-assembled. However, evidence suggests otherwise, as water contamination of FPS bearings has been reported in several bridges across the country. For instance, Washington Department of Transportation reported that 14 of 29 bearings from Snohomish

River Bridge had significant water contamination; as a result some of these bearings showed corrosion byproducts (WSDOT, 2015). In New York's Tappan Zee Bridge, 64 of the bearings (13%) exhibited some level of water intrusion within the environmental seals after erection and subjected to construction loading (Tappan Zee Constructors, 2017). The likely impacts of contamination, corrosion and surface roughness, are described next.

2.1.6. Corrosion and Surface Roughness

Corrosion of stainless steel in an atmospheric environment is possible, and appears as a form of white stains over the surface. This corrosion can be associated with increased surface roughness, which can increase the resistance to sliding and thus increase the effective friction coefficient. Constantinou et al. (2007) reported an experiment that imposed control of the surface roughness in bearings with PTFE-SS sliding interface, with SS having surface roughness of 0.03, 0.30 and 0.50 μm. A surface roughness of 0.03 μm corresponds to that of a commercially polished to mirror finished SS sheet, while surface roughness of 0.30 μm corresponds to that of an as-rolled SS sheet. For the surface roughness of 0.50 μm, Constantinou et al. (2007) used a wire brush to uniformly roughen an as-rolled SS sheet. The results showed a substantial increase in the coefficient of friction, approximately 100%, due to surface roughness at low velocities of sliding. This friction increase was probably due to plowing of the PTFE by the rough stainless steel and third body effects from wear particles. On the other hand, surface roughness was found to have less effect on the coefficient of friction at high sliding velocities, wherein the friction coefficient increased by approximately 15%. Unfilled PTFE was almost unaffected by

surface roughness at high sliding velocities, with an increase in friction coefficient of about 3%.

With regard to the natural development of corrosion in bearings, Constantinou et al. (2007) observed corrosion of the stainless steel in a test bearing that had been tested extensively over 9 years, and was stored indoors disassembled some of the time. The bearing showed rust stains that covered about 15% of the stainless steel surface. The rust surface measured a surface roughness of 0.3 μm and the rest of the surface (clean surface) measured a surface roughness of 0.03 μm. From this data, Constantinou et al. (2007) concluded, conservatively, that surface roughness values of 0.30 and 0.50 μm would develop after 30 years of exposure in industrial/urban and industrial/chemical environment, respectively. Based on the data and assumptions presented in this section, Constantinou et al. (2007) suggest that friction coefficients for high velocity sliding be amplified by factors shown in Table 2.1 to account for surface roughness. These factors are proposed to account for the corrosion in the bearing produced by exposure to different environments after 30 years.

Table 2.1. Factors of amplification for high velocity sliding coefficient of friction (Constantinou et al, 2007)

	Installation Method of Stainless Steel Plate in Sliding Bearing		
Environment	Sealed Facing Down	Sealed Facing Up	Unsealed Facing Down
Rural	1.10	1.20	1.20
Industrial/Urban	1.20	1.30	1.30
Marine	1.30	1.40	1.40
Industrial/Chemical	1.40	>1.40	>1.40

Reports of corrosion effects due to freshwater contamination have not been identified; however, Zhao et al. (2019) performed tests to identify effects of corrosion for a spherical sliding bearing in a marine environment. Two test arrangements were used; the first test arrangement consisted of bearing specimens periodically sprayed with salt, while for the second test arrangement, the bearing specimens were submerged in saline water and allowed to dry up. The results for the second test arrangement are shown in Figure 2.4. The observed wave-like behavior is a result of the salinity forming a smoother layer on top of the sliding surface that is disrupted by the next wet-drying cycle. The coefficient of friction decreases when the smooth layer is formed and increases as the salt layer is disrupted and the roughness increases (Zhao et al., 2019). Overall, the tendency is that coefficient of friction increases with corrosion associated with saltwater intrusion, due to an increase in surface roughness relative to the initial roughness. Freshwater intrusion is expected to influence the friction less significantly, as a salt layer would not form.

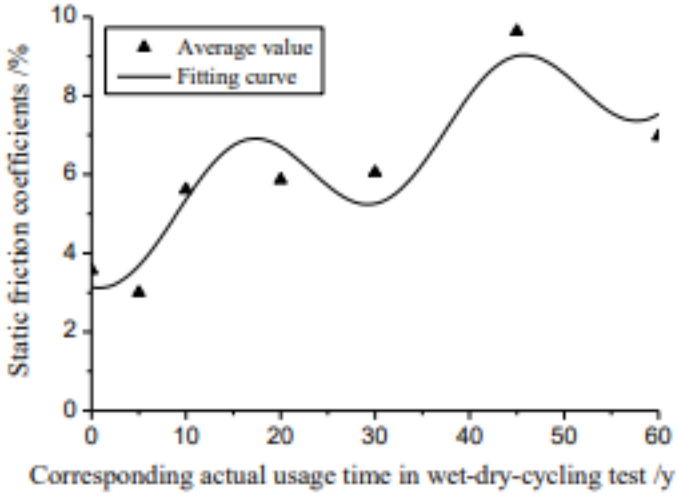

Figure 2.4. Effect of saline water corrosion in SPB (Zhao et al. 2019)

2.1.7. Load Dwell

Load dwell refers to the duration of stationary static loading without any relative movement across the sliding interface. For an interface with bimetallic surfaces (e.g. steel-steel), load dwell or time of loading can cause the static friction to increase. For a PTFE-SS interface, the effect of load dwell is not significant. Experiments on PTFE–polished SS surfaces showed that for load dwell between 0.2 and 118.4 hours the static friction is unaffected (Constantinou et al. 2007).

2.1.8. Effects of Travel

The accumulated distance of relative movement between the bearing slider and sliding surfaces is defined as travel. Constantinou et al. (2007) estimated the cumulative movement of a typical bridge bearing due to traffic loads to be in the order of 5 km, with the following assumptions: steel girder bridge, average speed of traffic of 60 km/h, span length of 100 feet, 30 years of service and 10 crossings per hour.

Kauschke and Baigent (1986) presented travel test results on unlubricated bearings with PTFE-polished SS sliding interface. The results showed that the coefficient of friction increased a little for a travel of 2 km. In contrast, in cumulative movement tests conducted by Long (1969, 1974) on the same sliding interfaces, a small decrease in sliding coefficient of friction was observed for a travel of 5 km. Despite the different trend, the change of the coefficient of friction for travel range of 2 to 5 km was small. According to Eggert and Kauschke (2002), after a travel of about 10 km the coefficient of friction increased due to

contamination and loss of lubrication, which led to an increase in the coefficient of friction at low temperatures. The tests were conducted at a temperature range of -35 to 20°C. Greater temperature sensitivity could be manifested in low temperature testing of bearings removed from service relative to new bearings.

2.2. Influence of Water Contamination on Friction Properties

The response of spherical sliding bearings during a seismic event depends greatly on their frictional properties. In the previous section, the different parameters that affect the friction coefficient of spherical sliding bearings were discussed. However, there is little documented data, if any, that shows how water contamination affects the frictional properties of spherical sliding bearings. The influence of water contamination on the breakaway and sliding friction coefficients between different materials is of great interest, especially PTFE in contact with SS, since this is the most common condition for the sliding interface of FPS bearings.

2.2.1. Effect of Water Lubrication on Sliding Friction

Several authors have performed tests to determine the friction coefficient of water-lubricated polymers in contact with steel (Mens and Gee 1991, Wang et al. 2009 and Jia et al. 2005). These studies examined the friction coefficients of PTFE and other polymers in contact with steel using the test arrangement shown in Figure 2.5. In this setup, a specimen with dimensions a x b x c is loaded using pressurized air while the rotating ring rotates at a

constant velocity, generating friction between the specimen and the ring. To accommodate for the difference in shape between the ring and the specimen, the ring is rotated until the specimen takes the shape of the ring. Table 2.2 summarizes the various test parameters considered by the authors mentioned above.

Table 2.2. Test parameters for ring tribometer test

Author(s)	Rotating Ring		Polymer	Test Dimensions (mm)					Axial Load (N)	Velocity (m/s)
	Material	Roughness (µm)	Material	a	b	c	d	e		
Mens and Gee (1991)	N/St	0.10	PA 66 + PTFE	10	10	10	N/S	N/S	500	0.25
Mens and Gee (1991)	N/St	0.10	POM + PTFE	10	10	10	N/S	N/S	500	0.25
Mens and Gee (1991)	N/St	0.10	PETP + PTFE	10	10	10	N/S	N/S	500	0.25
Mens and Gee (1991)	N/St	0.10	PEEK + PTFE	10	10	10	N/S	N/S	500	0.25
Mens and Gee (1991)	N/St	0.10	PPS + PTFE	10	10	10	N/S	N/S	500	0.25
Mens and Gee (1991)	N/St	0.10	PEI + PTFE	10	10	10	N/S	N/S	500	0.25
Wang et al. (2009)	AISI 52100	0.15	PTFE	19	12	12	49.22	43.45	100	0.50
Jia et al. (2005)	SS	0.10	PTFE + CF	30	7	6	40.00	28.00	200	0.43

*N/S = Not specified
**N/St = Not specified steel type

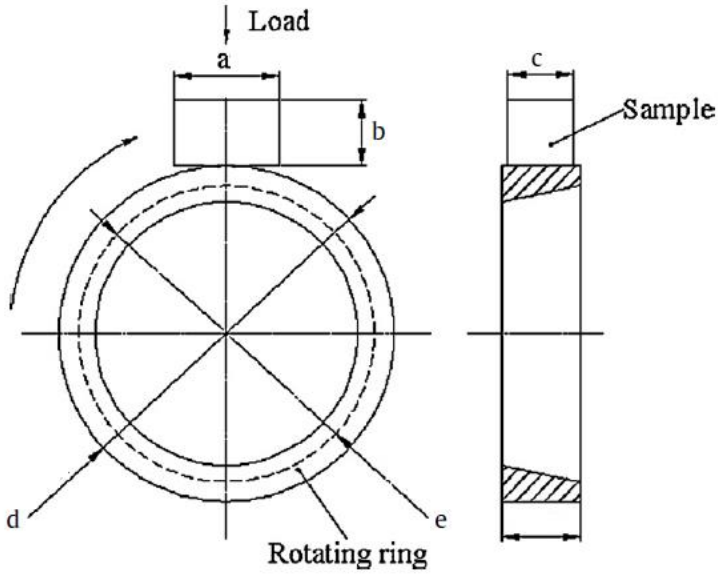

Figure 2.5. Rotating ring tribometer (Wang et al., 2009)

Mens and Gee (1991) conducted tests on the following polymers reinforced with PTFE: polyamide 66 (PA 66), polyoxymethylene (POM), polyethyleneterephthalate (PETP), polyetheretherketone (PEEK), polyphenylenesulphide (PPS) and polyetherimide (PEI). Among the polymers tested, POM is frequently used in applications with relative sliding between parts and has properties very similar to PTFE. The tests were performed and sliding friction was measured in dry and wet conditions. Table 2.3 tabulates the friction coefficients that were observed when thermal equilibrium was reached, which occurred after 0.5 hours of testing for all the specimens. The coefficient of friction was lower in wet conditions, but more variability was experienced than for dry conditions. For instance, for POM – PTFE composite, sample friction coefficients of 0.21 and 0.22 were observed during dry tests, while corresponding coefficients of 0.15 and 0.20 were observed during wet tests.

Table 2.3. Coefficient of friction at thermal equilibrium for dry and wet conditions (Mens and Gee, 1991)

Material	Dry friction coefficient	Wet friction coefficient
PA 66 - PTFE	0.13 0.14	0.19 0.08
POM - PTFE	0.22 0.21	0.15 0.20
PETP - PTFE	0.16 0.13	0.10 0.12
PEEK - PTFE	0.19 0.17	0.10 0.08
PPS - PTFE	0.31 0.29	0.10 0.09
PEI - PTFE	0.22 0.21	0.16 0.15

Wang et al. (2009) explored the variation in water contaminated friction of PTFE on steel imposed by freshwater versus saltwater conditions. The test variations included dry conditions (Air), distilled water lubrication (Distilled), sea water lubrication (Sea), and three additional solutions (S1, S2 and S3) that account for the variation in sea water composition. The Distilled condition is considered of greatest interest for this study. Tests results showed that coefficient of friction is about 3 times smaller in Distilled (0.05) compared to Air (0.17), and is essentially invariant with time for a sliding time less than 5 minutes (Figure 2.6).

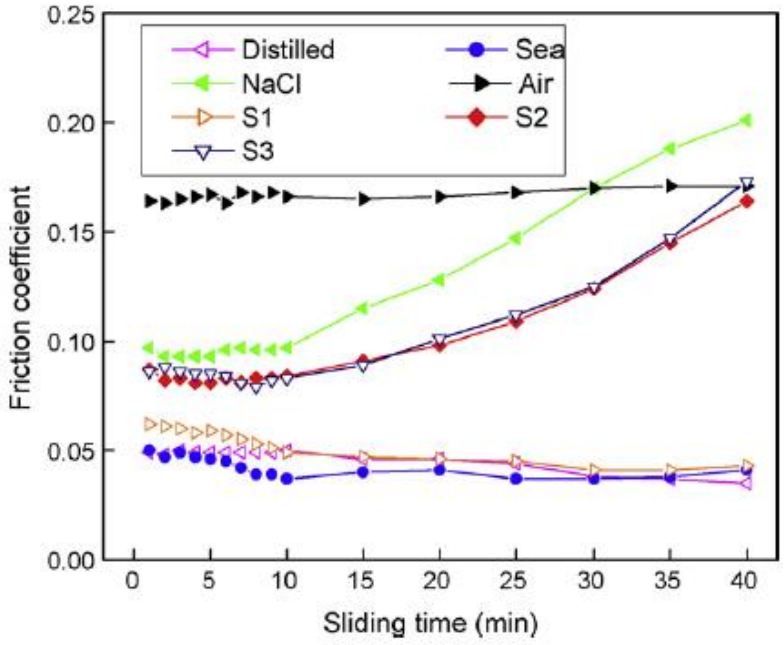

Figure 2.6. Variation of friction coefficient with sliding time (Wang et al., 2009)

Jia et al. (2005) conducted tests on 4 different composites sliding on stainless steel, in wet and dry conditions. These composites were: PTFE reinforced by 15% carbon fiber (CF), Polyimide (PI) reinforced by 15% CF and 5% PTFE, PI reinforced by 15% CF and 5% MoS_2, PEEK reinforced by 15% CF and 5% PTFE. Wet friction was observed to be 3 times smaller than dry friction for PTFE, which agrees with Wang et al. (2009). It was also observed that wet friction was about 60% of dry friction comparable to results obtained by Mens et al. (1991). Table 2.4 summarizes the results.

Table 2.4. Coefficient of friction for dry and wet conditions. (Jia et al., 2005)

Material	Dry friction coefficient	Wet friction coefficient
PTFE + 15% CF	0.20	0.07
PI + 15% CF + 5% PTFE	0.16	0.12
PI + 15% CF + 5% MoS_2	0.18	0.10
PEEK + 15% CF + 5% PTFE	0.15	0.09

A different test arrangement to assess wet friction was used by Golchin et al. (2013). The test setup consisted of a stationary polymer pin in contact with a SS rotating disc submerged in distilled water, as shown in Figure 2.7. An axial load was applied to the pin using dead weights. Polymers tested were: ultra high molecular weight polyethylene (UHMWPE), POM, polyethylene therephthalate (PET), polyamide 6 (PA6), PA66, PTFE, polypropylene (PP), polyvinylidene fluoride (PVDF), PEEK, polycarbonate (PC) and polymethyl methacrylate (PMMA). The test parameters are summarized in Table 2.5.

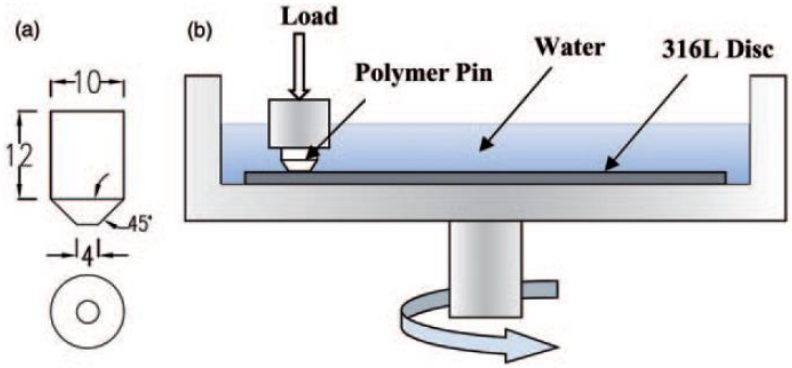

Figure 2.7. Schematic diagram of (a) pin and (b) test configuration (Golchin et al., 2013)

Table 2.5. Test parameters

(Golchin et al., 2013)

Load	62.8 N
Sliding velocity	0.13 m/s
Test duration	20 h
Steel surface roughness	0.2 μm

The results by Golchin et al. (2013) are shown in Figure 2.8. The objective of the research was to compare friction of different polymers with water lubrication, hence only water lubrication or wet friction tests were conducted. The plot in Figure 2.8 shows that coefficient of friction for PTFE was about 0.07, constant almost along all the duration of

the test, which is in agreement with results by Jia et al. (2005) and is about half the wet friction coefficient obtained by Wang et al. (2009). The difference in friction coefficients produced by different test can be attributed to the different test arrangements, and to the fact that Jia et al. (2005) tested filled PTFE while Golchin et al. (2013) tested unfilled PTFE.

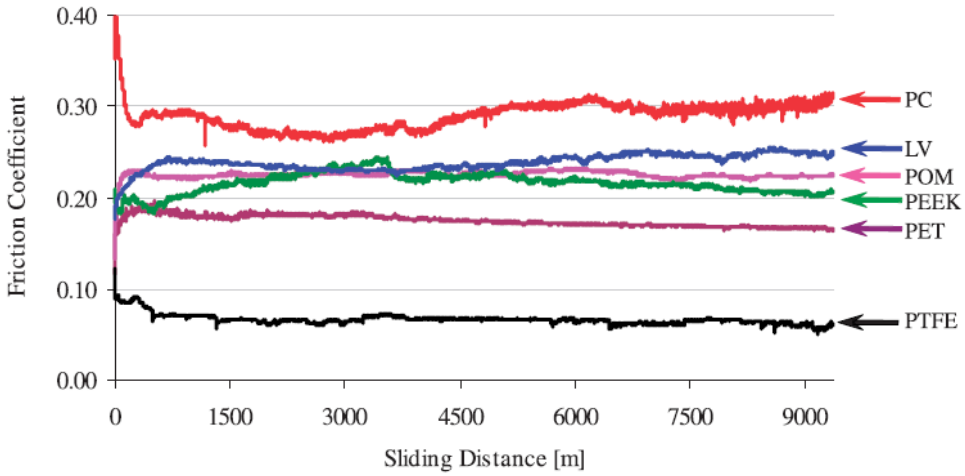

Figure 2.8. Coefficient of friction for water lubrication on different polymers (Golchin et al., 2013)

2.2.2. Effect of Water Lubrication on Breakaway Friction

Fewer tests have been conducted to document breakaway friction of water lubricated PTFE in contact with SS in comparison to sliding friction. However, Benabdallah (2007) conducted tests on POM-based polymers designated as DE20076, DE100KM and DE12017; and Nylon-66 designated ZY103HSL, sliding on a steel platform. As described in Section 2.2.1, POM applications and properties are very similar to PTFE. The test setup consisted of a 95 x 12 x 3 mm polymer plate resting on top of a rotating platform, as shown in Figure 2.9, with an LED transmitter on top of the plate.

Stationary photodiode receivers were placed on top of the arrangement to measure the displacement of the polymer plate. The contact surface of the polymer plate was polished to get a surface roughness of 0.3 μm, and the surface roughness of the ANSI 1045 steel platform was 1.78 μm (much higher than SS in FPS bearings). A weight of 2 N was fixed on top of the polymer plate to apply an axial load.

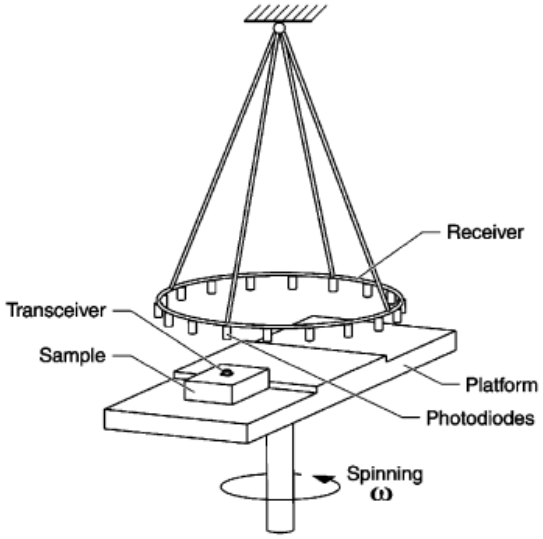

Figure 2.9. Break away friction test arrangement (Benabdallah, 2007)

On average, most sliding interfaces experienced about a 60% increase in breakaway friction when lubricated with water (Figure 2.10). This increase in friction was attributed to an increase in the adhesion between the polymer and the steel surface due to the formation of meniscus forces, a consequence of the presence of water. No correlation is observed with friction coefficients measured by Golchin et al. (2017) when the distance is 0 (Figure 2.8), nor with Wang et al. (2009) when the time is 0 (Figure 2.6). However, test set ups used by Golchin et al. (2017) and Wang et al. (2009) were designed to measure sliding friction, which may be the reason for the discrepancy.

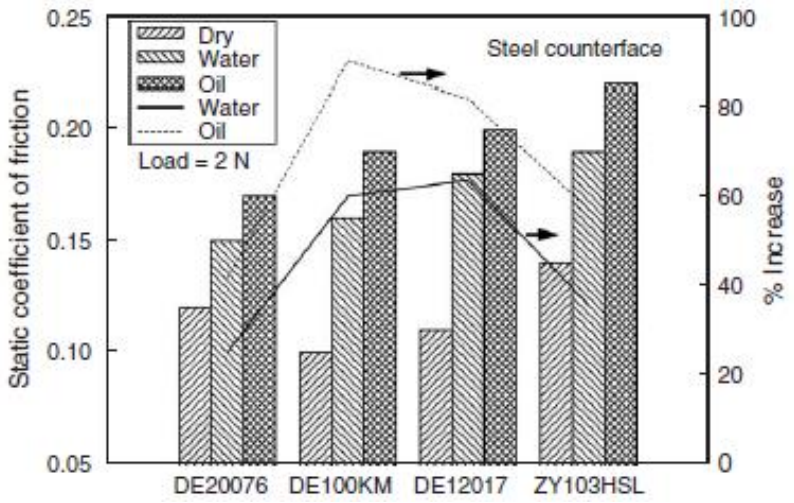

Figure 2.10. Effects of lubrication on breakaway friction coefficient (Benabdallah, 2007)

In summary, sliding coefficient of friction decreases with water lubrication. Results shown in Section 2.2.1 suggest that there is more variability in wet friction than in dry friction and that the reduction in coefficient of friction depends on the type of PTFE (e.g. unfilled PTFE, PTFE filled with carbon). Only one author studied breakaway friction in a way relatable to this study, and in that study breakaway friction increased with water lubrication.

2.3. Influence of Frozen Water on Frictional Properties

So far, discussion has focused on how water contamination may affect frictional properties of different sliding surfaces. However, at low temperatures, water inside the bearings will freeze, causing a problem of a different nature.

For the slider to move or slide along the concave plate of a bearing contaminated with frozen water, the slider will have to either break the bond between the concave plate

and the ice or break the ice itself. The first type of failure is denoted adhesive failure while the latter is known as cohesive failure of the ice. From here on, the material of the concave plate or sliding surface will be referred to as "substrate". The ice failure mechanism depends on several variables such as the ice temperature, substrate and freezing process.

2.3.1. Ice Adhesive and Cohesive Strength

Adhesive strength is defined as the maximum force required to mechanically separate ice from any substrate or contact surface. Cohesive strength refers to the shear strength of the ice as a material. When the adhesive strength of the bond is greater than the cohesive strength of the ice, the ice will break before the adhesive bond breaks and a layer of ice will remain bonded to the substrate.

Only one known experiment has documented ice adhesive strength specifically in FPS bearings. In conjunction with EPS, Tappan Zee Constructors (2017) conducted tests on ice contaminated triple pendulum bearings (TPB). In-service bearings that had experienced water contamination were removed from the Tappan Zee Bridge and shipped to EPS. Two of the bearings were tested with different levels of ice, wherein freezing was induced by pumping liquid nitrogen directly into the bearing cavity. Bearing 8833-06 was tested with water levels as received (1/2" layer of ice in the lower concave sliding cavity and ¼" layer of ice in the inner slider cavity) and bearing 8833-08 was tested with water filled to the top of the rim in both the lower concave (3") and inner sliding cavities. Force vs displacement hysteresis loops for both bearings are shown in Figure 2.11, and testing conditions are summarized in Table 2.6. A small increase of shear force was observed at

small displacements just before the ice broke. When compared with a clean bearing, shear force in the ice contaminated bearing increased by about 10%. In both cases, the authors observed that the "initial calibration of the test machine may have broken the ice". Although not ideal, cracking of ice due to the presumably low level forces associated with calibration does not suggest an inherent problem in testing, since the much higher level lateral forces should easily accomplish the same. However, as discussed later, rapid freezing can negatively affect the ice strength. In general, the report lacks sufficient detail to understand the freezing and testing protocol, and freezing by liquid nitrogen may have led to ice conditions that vary substantially from those under the natural environmental conditions in an in-service bridge. The authors also commented that "no movement was observed between the interior slider and the interior bottom concave plate." It is unclear whether this refers to the bottom most concave sliding surface or the inner sliding surface that would be expected to engage at low levels of friction. Inability to engage sliding on the bottom most concave sliding surface would not necessarily significantly impede movement in a DPB or TPB since ice most likely cannot penetrate the top most concave sliding surface. The same would not be true of an SPB.

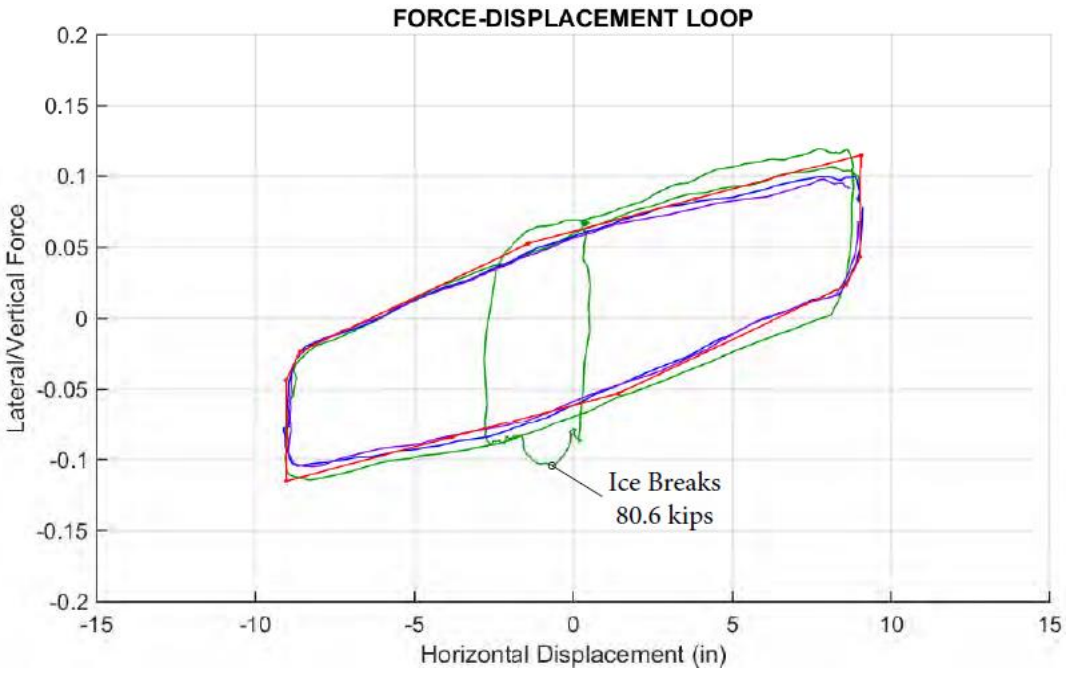

(a)

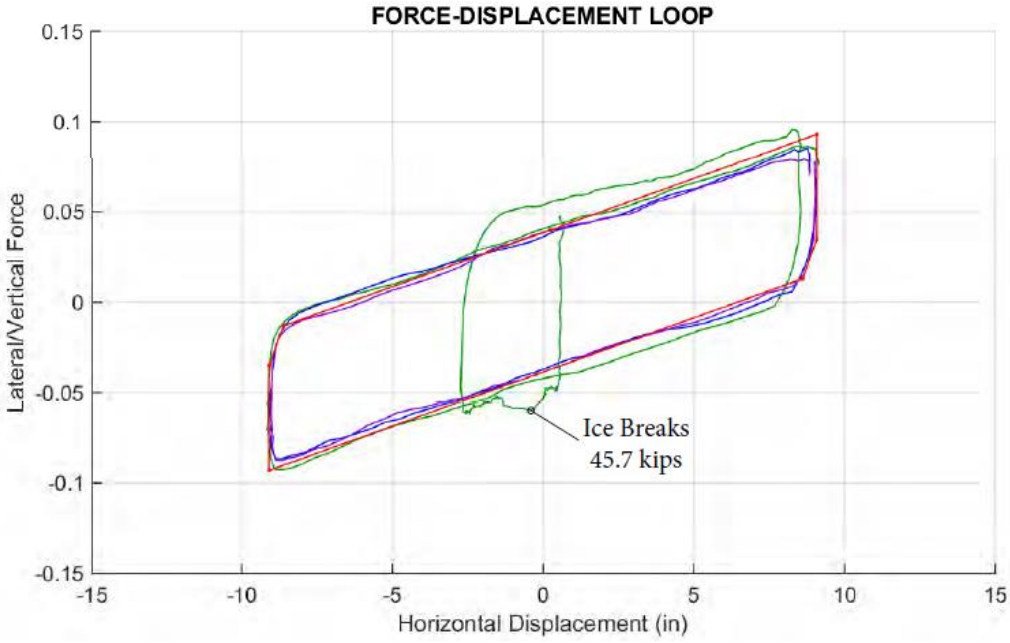

(b)

Figure 2.11. Ice contaminated bearing hysteresis loop (a) Bearing 8833-08 (b) Bearing 8833-06 (Tappan Zee Constructors, 2017)

Table 2.6. Ice contaminated bearings test Conditions

(Tapan Zee Constructors, 2017)

Bearing	8833-08	8833-06
Target displacement	8 in	8 in
Target vertical load	700 kips	700 kips
Ice thickness	3 in	0.5 in
Number of cycles	3	3

Besides the specific data pertinent to FPS bearings mentioned above, some authors have experimentally determined ice adhesive strength, cohesive strength, or both. Varying experimental set ups and sampling methods have been applied, and varying environmental conditions and substrates have been considered. The adhesive strength of ice depends greatly on the testing method. Fortin and Perron (2012) compiled the results of tests conducted by different authors regarding ice adhesive strength (Table 2.7). Much of the variability in the results of Table 2.7 can be associated with the different testing methods and different substrates tested. Other factors affecting ice adhesion are ice purity, nature/texture of the substrate, and temperature. In their own experiments, Fortin and Perron (2012) found that the ice started to fail at a stress of about 0.50 MPa.

Table 2.7. Ice adhesive shear strength from different authors (Fortin and Perron, 2012)

Author (s)	Ice	Method	Substrate	Adhesion shear stress (MPa)		
				Minimum	Average	Maximum
Lughborough and Haas	Frozen water	Centrifuge	Aluminum	-	1.52	-
			Copper	-	0.85	-
			Polymers	1.03	-	1.17
Laforte et al.	Rime and glaze		Aluminum	0.067	-	0.4
Itagaki	Artificial ice	Centrifuge	Aluminum	0.002	-	0.11
Jellinek	Ice from snow	Torsion	Stainless Steel	-	0.48	-
Scavuzzo et al.	Artificial ice	Centrifuge	Aluminum	0.05	-	0.30
Raraty and Tabor	Frozen water	Centrifuge	Stainless steel		1.96	
Bascom et al.	Frozen water	Centrifuge	Stainless steel		1.63	
Ford and Nichols	Frozen water	Axial loading	Stainless steel		0.24	
Stallabrass and Price	Artificial Ice	Centrifuge	Aluminum	0.03		0.13
Reich	Frozen water	Axial loading	Aluminum	0.83		0.93

Ice adhesive strength can be experimentally determined through use of a centrifuge. The centrifuge test procedure was described by Fortin et al. (2010). As a first step, samples were generated by freezing water on 340 mm x 31.75 mm x 6.4 mm beams using a Freezing Drizzle Climatic (FDC) chamber. The samples were frozen to a temperature of -8.0 ± 1.0 ºC. Prepared samples were tested on a centrifuge apparatus installed in the FDC chamber. The beam was rotated at a controlled increasing rate correlated to the centrifugal force. When the centrifugal force became sufficiently large, ice detachment was observed, and the adhesive strength was inferred. Figure 2.12 shows the centrifuge apparatus.

Figure 2.12. Centrifuge apparatus (Fortin et al., 2010)

Raraty and Tabor (1958) also conducted centrifuge type experiments on ice adhesion to SS using an annular interface (Figure 2.13). The SS surface was polished, filled with tap water, and frozen slowly. Adhesive strength versus temperature is shown in Figure 2.14, wherein the black dots and associated fitted curve represent the experiment described above. For temperatures below -7°C, ice adhesion was independent of the temperature. Raraty and Tabor (1958) concluded that the low temperature failures below -7°C represented cohesive failures.

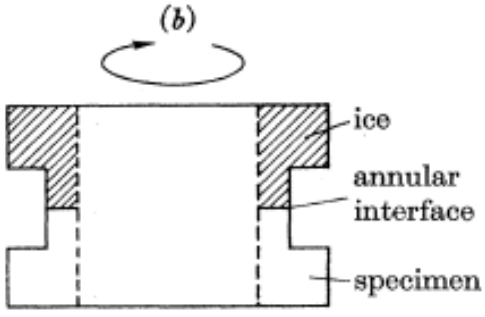

Figure 2.13. Test specimen (Raraty and Tabor, 1958)

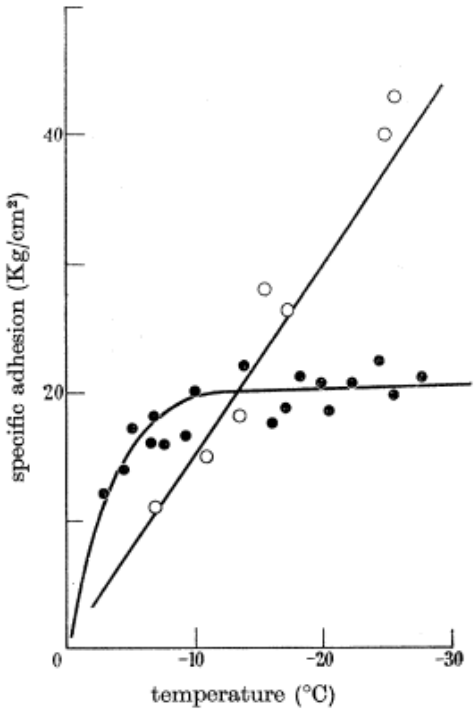

Figure 2.14. Adhesive strength of ice to clean stainless steel (Raraty and Tabor, 1958)

Alternatively, Andrews and Lockington (1983) conducted tests using two different axial loading set up arrangements to determine adhesive and cohesive strength, respectively. The layout shown in Figure 2.15 was used. For the adhesion tests (Fig. 2.15(a)), ice was formed over the height F and bonded to the substrate on zone E, and a thin PTFE disk was located on position B to create an initial crack. Axial load was applied to the specimen by pressurizing the orifice D using a pump. The test arrangement for cohesive failure (Figure 2.15 (b)) was the same as that for adhesive failure, with the PTFE disk located at a height "C" from the ice – SS interface, generating a cohesive type of failure along height "h". For ice on SS substrate, these experiments showed an adhesive failure for temperatures above -5 ºC and a cohesive failure for temperatures below -5 ºC, which was asymptotic and not dependent on temperature (Figure 2.16).

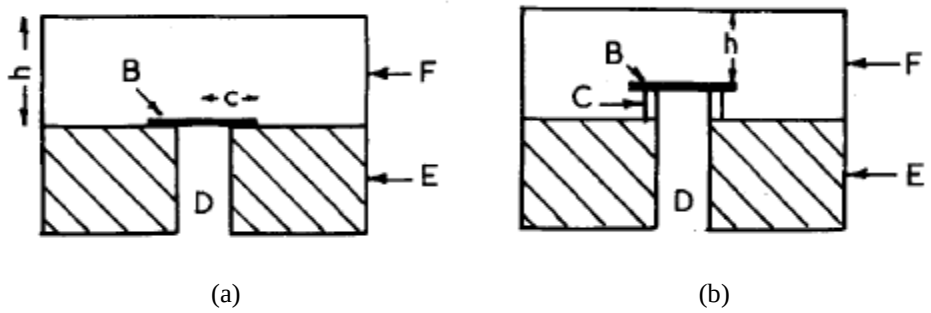

(a) (b)

Figure 2.15. (a) Adhesive test arrangement, (b) cohesive test arrangement (Andrews and Stevenson, 1978)

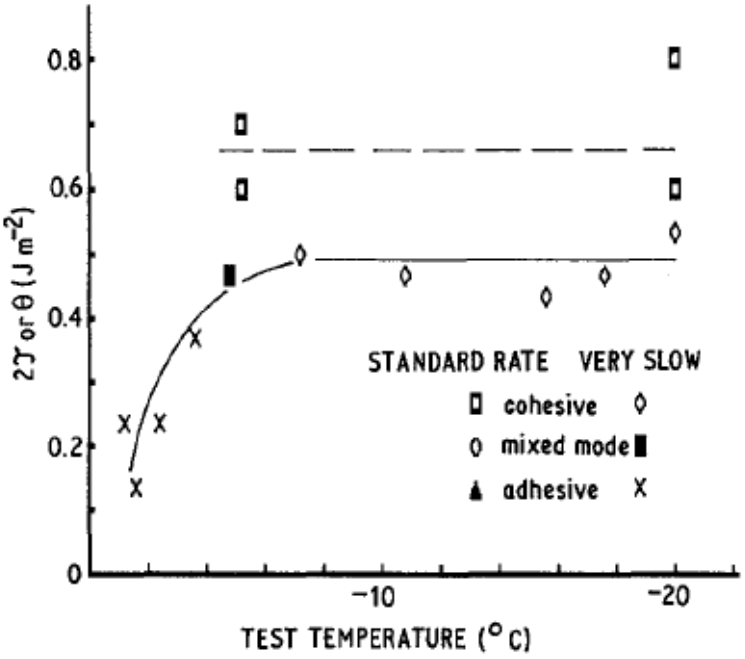

Figure 2.16. Variation of failure energy with temperature for stainless steel (Andrews and Lockington, 1983)

Makkonen (2012) reported experiments conducted by VTT Technical Research Centre of Finland on ice adhesive strength using a different procedure. In these experiments, a 30 mm diameter plastic cylinder filled with water was frozen on top of a 100 mm x 100 mm x 10 mm aluminum plate coated with a substrate of interest. Each

sample was placed in a freezer for at least 24 hours, and after that a horizontal load was slowly applied to the frozen cylinder. Different substrates were considered and led to different adhesive strengths, as shown in Figure 2.17. The substrate considered most relevant is steel, since the sliding surface of an FPS bearing is commonly made of SS. Note that the peak adhesive strength occurs at -15°C and gets lower as temperature drops. The adhesive strength was found to vary from 0 to 1 MPa, wherein the higher values are comparable to cohesive shear strength of the ice. For cohesive type of failures, the axial loading method is expected to better represent the conditions of a bearing slider breaking through ice. However, the methodology presented by Makkonen (2012), which applied a transverse or shear loading between the ice and its substrate, is closer to the conditions of the contaminated sliding bearing in the case of an adhesive failure of ice.

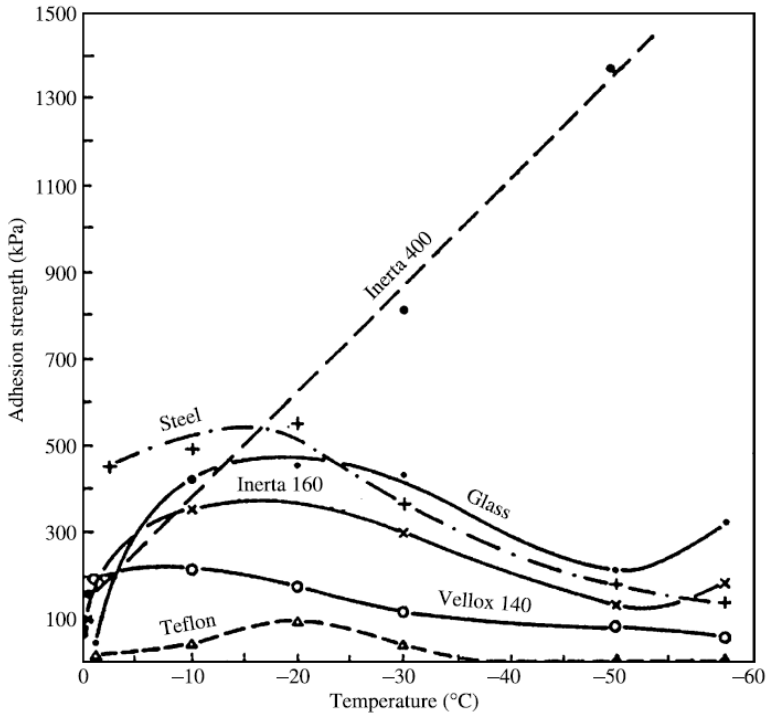

Figure 2.17. Effects of temperature in ice adhesion for shear testing (Makkonen, 2012)

Several studies emphasized freezing process and freezing time in their experimental methodology. For example, in Makonnen (2012), slow freezing was applied to avoid cracking of ice due to thermal contraction while freezing and secure the strongest bond possible. Adjacent materials with different specific heat properties experience temperature change at different rates from each other, in this context generating thermal differential stresses between ice and the substrate.

Ice adhesive strength is also affected by the time the sample is kept frozen before testing. Sukhorukov et al. (2013) conducted experiments on ice adhesion using 50 mm inner diameter by 95 mm high cylinder samples. The time needed for the samples to reach thermal equilibrium is given by:

$$t = \frac{d_{cyl}^2}{\frac{k_i}{c_i p_i}} \tag{2.4}$$

where d_{cyl} is the diameter of the sample, k_i is the coefficient of thermal conductivity, c_i is the specific heat capacity and p_i is the density of ice. For the specimen with d_{cyl} = 5x10^{-2}m, k_i = 2.1 W/m K, c_i = 2100 J/kg K, and p_i = 916 kg/m^3, the characteristic time was computed to be 40 min.

In the only known freezing tests of FPS bearings, the bearings were frozen rapidly using liquid nitrogen and kept frozen for an unknown length of time. As a consequence, ice may have cracked prematurely; hence, the results may not represent accurately the behavior of FPS bearings in the field (Tappan Zee Constructors, 2017).

2.3.2. Adhesive and Cohesive Strength Model

Fortin and Perron (2012) have developed a set of equations to model combined ice strength τ due to adhesion and cohesion. The equation includes both an adhesive strength term and a cohesive term:

$$\tau_{tot} = \alpha_{ice}\frac{4\gamma_{LV}}{\delta_{0-ice}}\left[f_{RMS} + \frac{\delta_{0-ice}}{k}(1 - f_{RMS})\left(1 - f_{cramp}\right)\right] + (1 - f_{RMS})f_{cramp}\tau_{coh} \tag{2.5}$$

$$\alpha_{ice} = \frac{\varepsilon_{water}\delta_{0-water}^2}{\varepsilon_{ice}\delta_{0-ice}^2} \tag{2.6}$$

where:

$\boldsymbol{\delta_{0\text{-water}}}$	=	Molecular distance between water and base substrate
$\boldsymbol{\delta_{0\text{-ice}}}$	=	Molecular distance between ice and base substrate
$\boldsymbol{\varepsilon_{water}}$	=	Relative permittivity of water
$\boldsymbol{\varepsilon_{ice}}$	=	Relative permittivity of ice
$\boldsymbol{\gamma_{LV}}$	=	Surface tension
$\boldsymbol{f_{RMS}}$	=	Fraction of ice in contact with base substrate
$\boldsymbol{k}$	=	Root mean square of roughness height
$\boldsymbol{f_{cramp}}$	=	Fraction of mechanical locking
$\boldsymbol{\tau_{coh}}$	=	Ice cohesive strength

The model idealizes the surface roughness as a regular surface with the geometry shown in Figure 2.18. Since every surface has some roughness, water will fill the cavities and after freezing a fraction of ice is locked in these cavities. The model assumes that adhesive failure occurs on top of the substrate asperities (first term of Equation 2.4), and cohesive strength governs the ice locked in the cavities (second term of Equation 2.4).

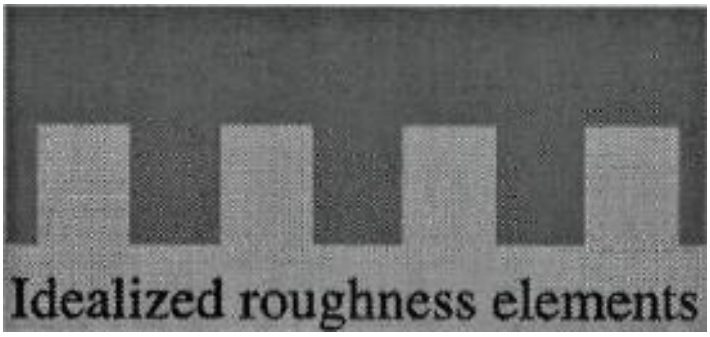

Figure 2.18. Idealized surface roughness. (Fortin and Perron, 2012)

Consider an ice contaminated FPS bearing as the one shown in Figure 2.19, if the slider displaces from point A to point B adhesive and cohesive strength of ice on the concave surface can be described using Equation 2.5. However, in order for the slider to move, cohesive strength of ice along L1 and L2 (Figure 2.19) must be overcome, hence the second term of the sum in Equation 2.5 needs to be modified to account for the extra cohesive strength along these lines.

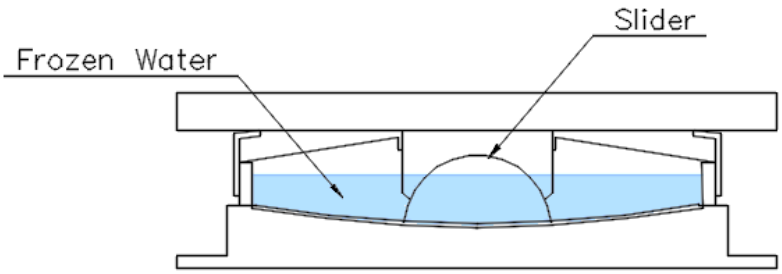

(a)

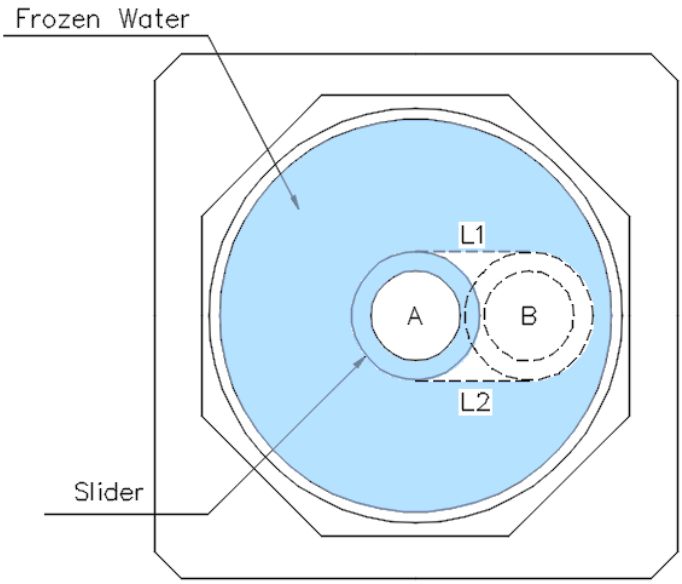

(b)

Figure 2.19. Ice contaminated FPS bearing drawing (a) Elevation (b) Plan view

Fortin and Perron (2011) also conducted a centrifugal test to validate the model, where the results showed an adhesive strength of 0.50 MPa for ice density of 773 kg/m^3 at -10 ºC on an aluminum substrate with surface roughness of 0.7 µm. Due to the low roughness of the material, the fraction of mechanical locking was assumed to be 0 (pure adhesion).

2.3.3. Ice Crushing

Another failure mechanism is possible in a friction pendulum bearing with ice trapped in a confined space. Ice spalling caused by the load of an object moving into the ice (e.g. an indenter or the bearing slider) is known as ice crushing. Joordan and Timco (1988) conducted experiments on ice crushing by pushing a 63.5 mm wide indenter into a 7000 mm x 16000 mm x 9 mm ice sheet with walls on all perimeter faces except the loaded face, as shown in Figure 2.20, which is a non-scaled schematic representation of the experiment. From the data, a model was developed for ice stiffness and crushing force. The model assumed that a crushed or pulverized layer formed at the contact zone and the rest of the ice was undamaged.

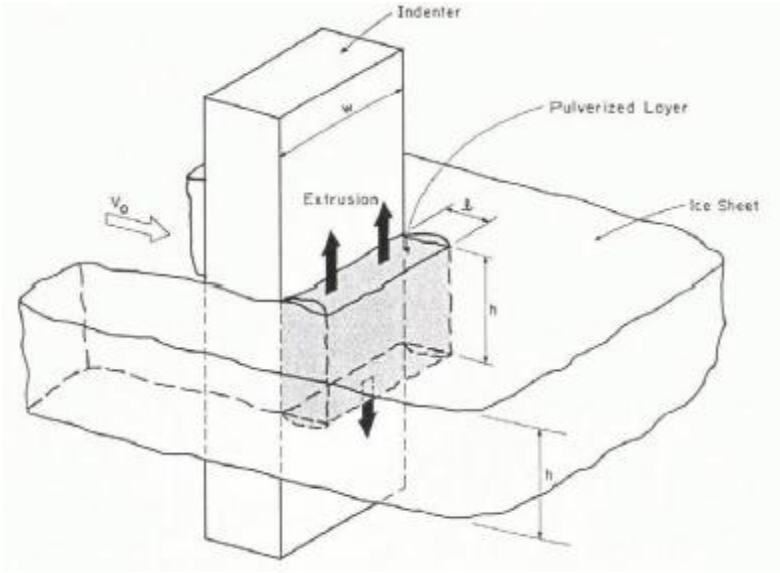

Figure 2.20. Schematic illustration of pulverized ice layer in continuous indentation experiment (Joordan and Timco, 1988)

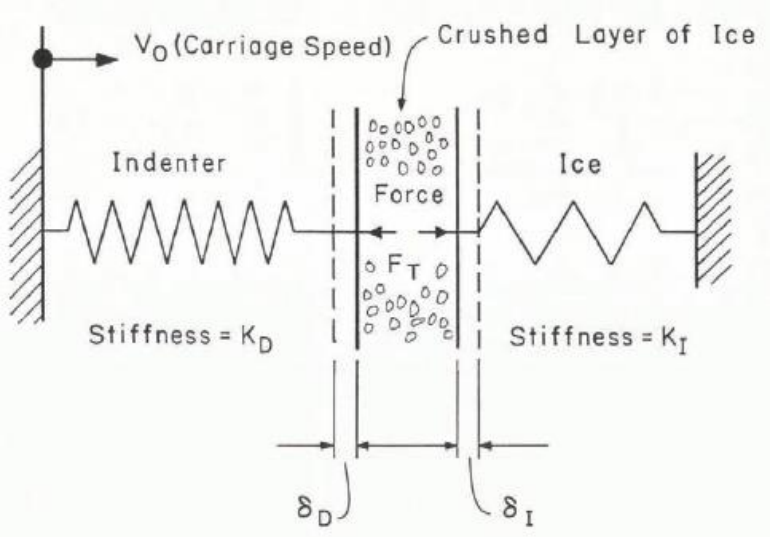

Figure 2.21. Mechanical model for pulverized ice layer, indenter and ice (Joordan and Timco, 1988)

Based on the idealized system shown in Figure 2.21, from elasticity theory, the ice stiffness K_I is:

$$K_I = 0.085\pi Eh \tag{2.6}$$

The reaction force F per unit width produced by the crushed layer into the indenter is computed as:

$$F = \vartheta v_0 \left(\frac{h}{l}\right)^3 \tag{2.7}$$

where:

E = Ice elastic modulus (assumed as 10000 MPa)
h = Thickness of ice layer
ϑ = Viscosity of crushed layer
l = Length of crushed layer

The mechanical models for adhesion and ice crushing are starting points, and may need to be modified and combined to represent the effects of ice in FPS bearings.

2.3.4. Ice Friction

If the adhesive strength of ice exceeds its cohesive strength, the ice will fail first, and an ice layer will remain on the surface. In this case, the concave sliding surface in FPS bearings will be covered by a thin ice layer, and the slider is expected to slide over the ice layer. Hence, the frictional properties between ice and different substrates (e.g. SS or PTFE) are relevant.

The friction coefficient of ice in contact with different substrates is still under study by the tribology community due to the complexity of the system and the variables that affect it. Four regimes on friction within ice are recognized: dry friction, boundary friction, mixed friction and hydrodynamic friction (Kietzig et al., 2010). Dry friction refers to the state where ice behaves as any other solid, with no lubrication between ice and the other substrate. Boundary friction is the state where a liquid-like layer has formed on the surface of ice and the temperature is just slightly lower than the melting point. In addition, the liquid-like layer thickness is much smaller than the characteristic roughness of the ice. Mixed friction is almost the same as boundary friction, except that the temperature at some locations is higher than the melting point. Finally, the hydrodynamic regime is achieved when the liquid-like layer thickness is greater than the characteristic roughness of the ice surface, and significant melting has initiated. Figure 2.22 illustrates the variation of the friction coefficient as ice transitions through the different friction regimes. Experimental

data by Dosch et al. (1995) and Furukawa et al. (1987) suggests that the liquid like layer on ice disappears at temperatures around -15°C and colder.

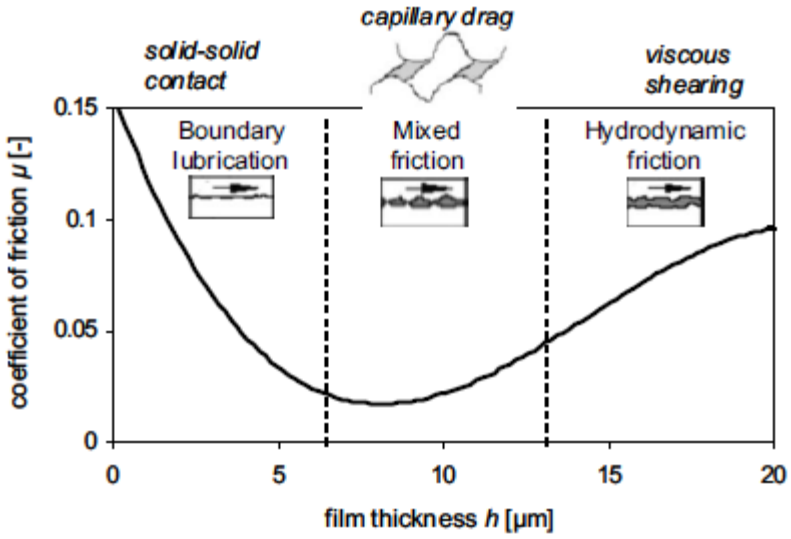

Figure 2.22. Friction regimes relevant to ice friction (Kietzig et al., 2010)

Velkavrh et al. (2019) tested a steel slider over an ice surface at -8°C and ambient temperature of -4°C. The samples were stored in a freezer for about 24 hours prior to testing and the velocities of testing ranged from 0.02 to 0.38 m/s. For SS samples with different surface roughness, the coefficient of friction was observed to increase with decreasing surface roughness. This trend was attributed to higher viscous friction, which is a characteristic of the hydrodynamic regime. The results are shown in Figure 2.23; gray lines correspond to SS with surface roughness below 0.1 μm, which corresponds to the surface roughness of commercially polished to mirror finished SS sheets. The friction coefficient for this surface roughness ranges from 0.14 to 0.08 as velocity increases. Colored lines in Figure 2.22 correspond to SS with surface roughness ranging from 0.8 to 3 μm.

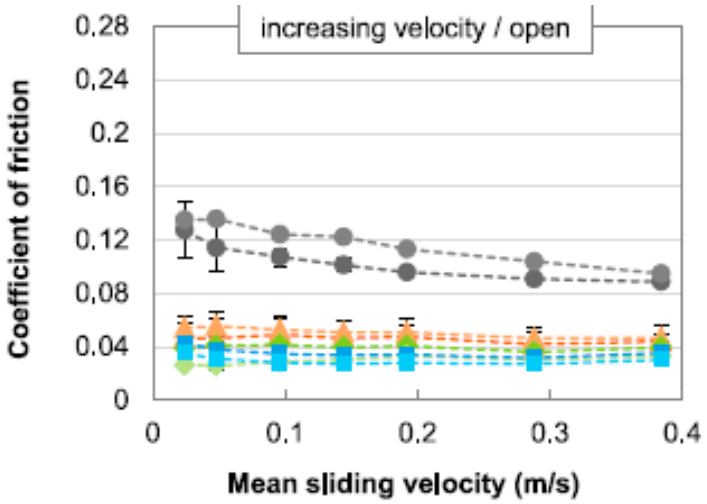

Figure 2.23. Coefficient of friction of SS with different surface roughness for different velocities (Velkavrh et al., 2019)

Marmo et al. (2005) took measurements of friction coefficient for ice on steel over a temperature range from -27°C to 0.5°C and a velocity range 0.008 to 0.37 m/s at a normal force of 2.10 to 4.20 N. The coefficient of friction ranged from 0.042 to 0.17. A strong dependence of friction coefficient on temperature was observed for temperatures below -15°C. At temperatures higher than -15°C the coefficient of friction was less than 0.05, and for temperature and velocity above -18.5°C and 0.006 m/s, respectively, the coefficient of friction decreased rapidly. The observations were presented in an ice friction map (Figure 2.24).

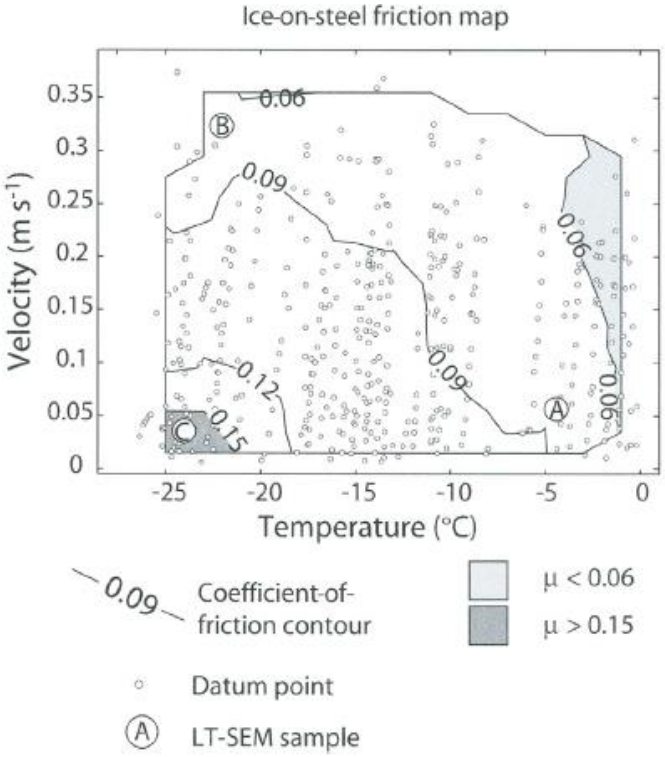

Figure 2.24. μ–V-T map for ice on steel (Marmo et al., 2005)

Makkonen and Tikanmaki (2014) developed a model to predict the coefficient of friction of ice in contact with different substrates. To validate the model, the analytical results were compared with the experimental results obtained by Marmo et al. (2005) (Figure 2.24) and they showed good agreement. An important consideration is that when the slider is much warmer than the ice surface, the friction between slider and ice should be modeled through conventional lubrication theory, which was not considered in Makkonen and Tikanmaki (2014) model. Figure 2.25 plots the modeled friction coefficient vs velocity for ice on different sliding interfaces.

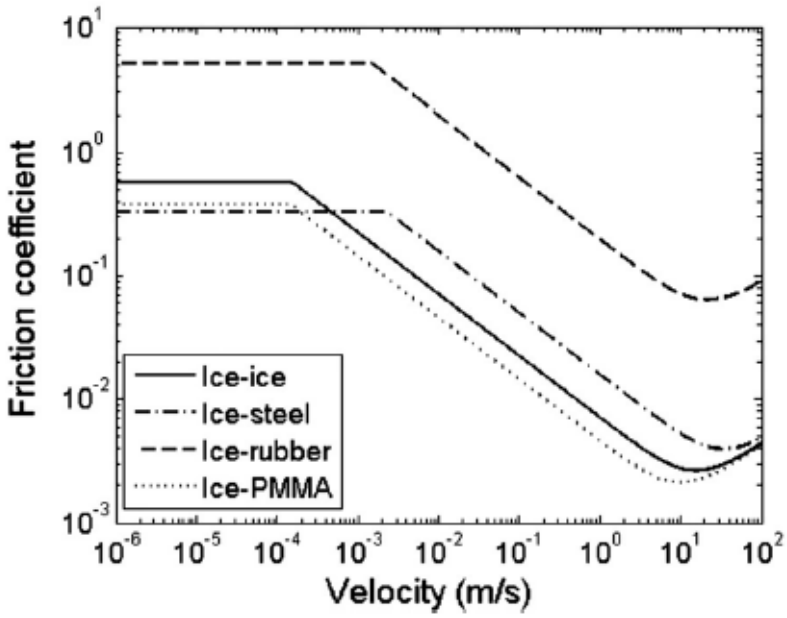

Figure 2.25. Modeled ice friction. (Makkonen and Tikanmaki, 2014)

Overall, all authors agree that coefficient of friction decreases with increasing velocity and increases with decreasing temperature for steel sliding on ice. There is not much information about frictional properties of PTFE sliding on ice. However, Makkonen and Tikanmaki (2014) simulated PMMA sliding on ice, which might be considered similar to PTFE. The coefficient of friction was generally lower than for steel sliding over ice, but the trend was very similar, as shown in Figure 2.25.

2.4. Summary and Predictions

It is expected that, in addition to the breakaway force needed to be overcome on clean bearings for the slider to start moving, the adhesive strength of the ice to stainless steel needs to be overcome too. Hence, a larger force to start the slider's movement is

expected. When the sliding surface of an FPS bearing is lubricated with water (e.g. a very tiny layer of water), a reduction in the sliding friction coefficient is expected. In some of the tests conducted by Wang et al. (2019) dry friction was about 3 times higher than water lubricated friction in PTFE – Steel interfaces. Mens and Gee (1991) found a less noticeable reduction of the coefficient of friction for polymer – polymer interface. Jia et al. (2005) found the dry coefficient of friction to be between 1.50 and 3 times larger than wet coefficient of friction in polymer – steel interfaces.

Based on limited information in the literature, the effect of water lubrication on the breakaway friction in polymer – steel interfaces is difficult to predict. However, the study conducted by Benabdallah (2007) showed that wet friction coefficient was 60% higher than dry coefficient of friction.

The strength and physical properties of the ice and the bond between ice and substrate were discussed as a starting point to predict the force required for the ice or bond to break, hence allowing the slider to move. A large variation was observed throughout the literature on ice and bond ice-substrate interface, which depended greatly on the temperature, type of ice, type of test, freezing time and freezing rate. However, most authors agree that a lower freezing rate creates a stronger bond between ice and base material because it allows the interface to accommodate differential thermal deformations. Tests conducted by Makkonen et al (2012) showed that for ice bonded to steel, the peak strength occurred at a temperature of -15°C and for ice bonded to Teflon it occurred at temperature of -20°C.

On the tests conducted by Tappan Zee Constructors (2017), which are the only known tests of an FPS bearing subjected to ice contamination, the hysteresis loop showed a spike in the force that represented the resistance before the ice was dislodged. The peak force due to ice resistance was lower than the force at the design displacement; however, the ice breakaway strength may have been affected by very rapid freezing.

Chapter 3. Test Set Up

As stated in Chapter 1, four FPS bearings will be tested separately using a shake table to assess the effects of water and ice contamination on their hysteretic force-deformation response. For ice contamination tests, the bearing will be axially loaded first, and then water inside the bearing will be frozen in place using dry ice. A steel frame (A-frame) to transmit the axial load from the hydraulic ram to the bearings has been designed and fabricated. An insulation box will be placed around the bearing and filled with dry ice after filling the bearing with water. This sequencing is required to prevent ice cracking due to the application of axial loading.

3.1. Test Bearings

Four bearings will be tested: 1 SPB from Robertson River Bridge and 3 DPB from Susitna River Bridge. Both bridges located in Alaska. Abutment bearings were chosen from both bridges because the design axial load of the bearings is compatible with the capacity of UNR's shake table.

3.1.1. Robertson River Bridge Bearings

Robertson River Bridge is located at Mile Point 123.2 of Alaska Highway. The bridge has 12 spans with maximum span length of 200 ft, and total length of 1980 ft. The overall width of the bridge is 27.9 ft. The superstructure is a steel truss as can be seen in

Figures 3.1 and 3.2, Figure 3.2 also shows dimensions of the superstructure. The total weight of the bridge is 7020 kips, excluding bearings and substructure.

Figure 3.1. Robertson River Bridge (Alaska DOT, 2018)

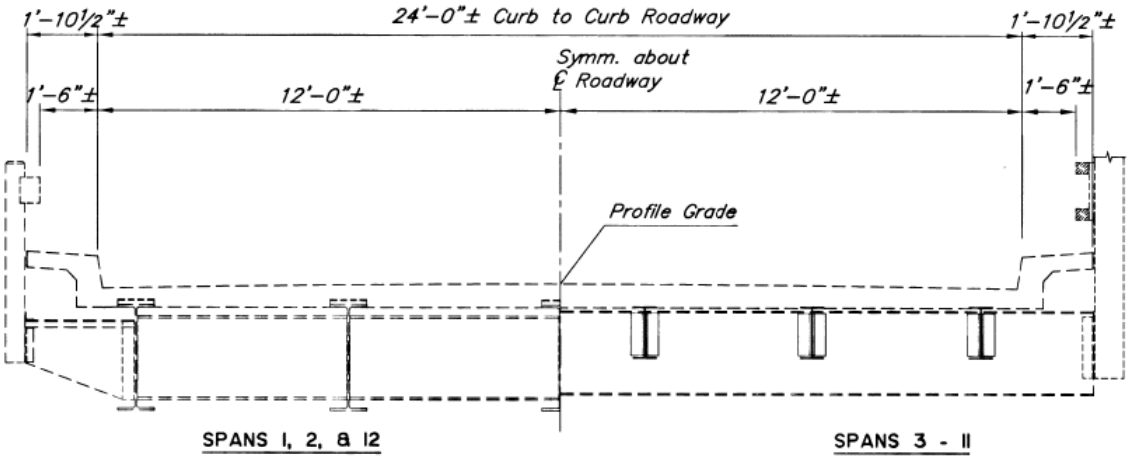

Figure 3.2. Robertson river bridge cross section (Alaska DOT, 2002)

After the bridge's construction in 1944 it was retrofitted in 2004 for the updated seismic demands at the bridge location by installing 3 types of SPB: Type 1A in piers 3 and 12, Type 2 in pier 2 and abutments, and Type 1 for the rest of the piers. A total of 56 SPB were installed to retrofit the bridge. For this study, EPS will manufacture 1 SPB with the same properties and geometry as Type 2. Table 3.1 identifies Type 2 bearing properties with reference to the general bearing cross-section shown in Figure 3.3. The dimensions of Robertson Type 2 bearing are identified in the cross section drawing of Figure 3.4.

Table 3.1. Robertson Bridge bearing type 2 properties

Displacement Capacity (in)	d_1	±6
Effective Radius (in)	R_1	61
Dynamic Period (s)	T	2.50
Coefficient of friction	μ_1	0.10
Min. Rotation Requirement (degrees)	-	2
Max. D+L Load (kips)	-	47

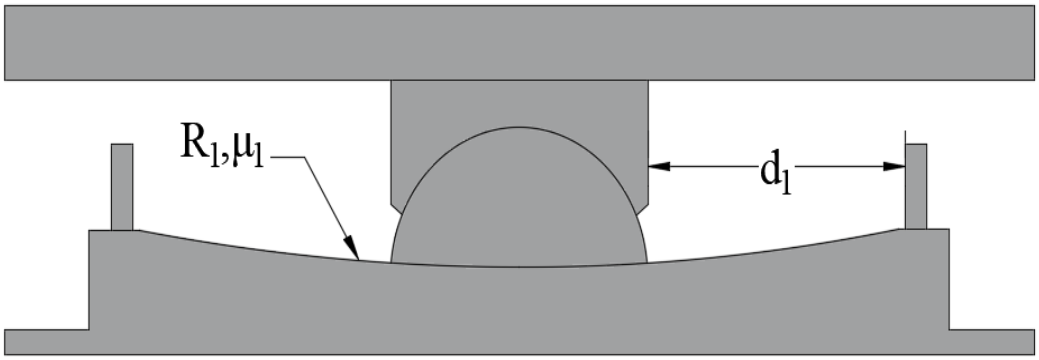

Figure 3.3. Generalized cross section of an SPB

The dynamic period is calculated using the following equation, using the parameters shown in Table 3.1:

$$T = 2\pi \sqrt{\frac{R_1}{g}} \tag{3.1}$$

where g is the acceleration of gravity.

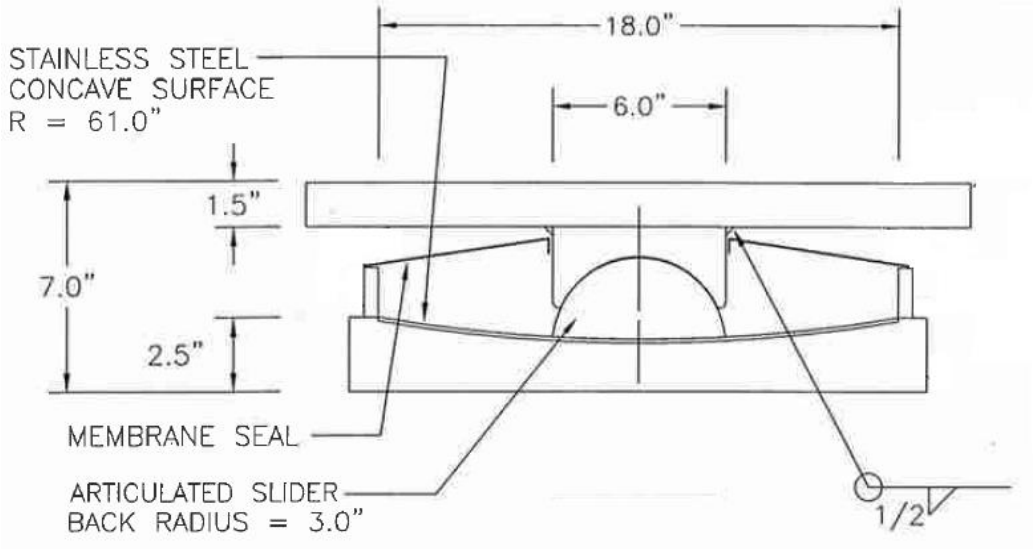

Figure 3.4. Robertson Bridge bearing cross section

In order to design the test set up and more specifically the A-frame, shear force and displacement demands in the bearing were calculated using two approaches. First, the design specifications for the bearing were reconstructed from available information, following the 1999 AASTHO Guide Specifications for Seismic Isolation (AASHTO, 1999), which was the governing code for the original design of the bearings. Second, the design specifications were determined using the 2010 AASTHO Guide Specifications for Seismic Isolation (AASHTO, 2010), or as "if designed today" to assess if the original design is in compliance with the current code. The design parameters for both approaches

is shown in Table 3.2. Since the bearings have sufficient capacity, the design parameters corresponding to the current AASHTO 2010 specifications will be used in the test program.

Table 3.2. Robertson Bridge bearing design parameters

	AASHTO 1999	**AASHTO 2010**	
Spectral Parameters			
AS*	0.32	-	g
S_s	-	0.4164	g
S_1	-	0.2302	g
Soil type	-	D	-
PGA	-	0.1751	g
S_{DS}	-	0.61081	g
S_{D1}	-	0.4465	g
Bearing Response			
W**	18	18	kips
K_{eff}	1.191	0.739	kips/in
T_{eff}	1.243	1.57789	s
B_{eff}	0.479	0.38256	-
B_L	1.979	1.7	-
D	2.01	4.052	in
F	2.393	2.995	kips
*Represents acceleration coefficient amplified by site coefficient. ** Max D+L capacity is 47 kips			

Bearing's displacement D is given by the following equations, for AASHTO 1999 and AASHTO 2010, respectively:

$$D = \frac{10AST_{eff}}{B_L} \tag{3.2}$$

$$D = \left(\frac{g}{4\pi^2}\right)\frac{S_{D1}T_{eff}}{B_L} \tag{3.3}$$

Bearing's shear force F is given by the following equation, for AASHTO 1999 and AASHTO 2010:

$$F = \mu W + \frac{W}{R} D \tag{3.4}$$

3.1.2. Susitna River Bridge Bearings

Susitna River Bridge is located at Mile Point 104.2 of Alaska Highway. The bridge's total length is 1072 ft, divided over 5 spans. The width of the bridge is 30 ft. The superstructure is a composed as follows: the deck is supported on steel stringers that transfer the load to floor trusses (Figure 3.6), then the truss transfers the load to the girders shown in Figure 3.5; dimensions of the superstructure are shown in Figure 3.6. The total weight of the bridge is 5620 kips, excluding bearings and substructure.

Figure 3.5. Susitna River Bridge (Alaska DOT, 2016)

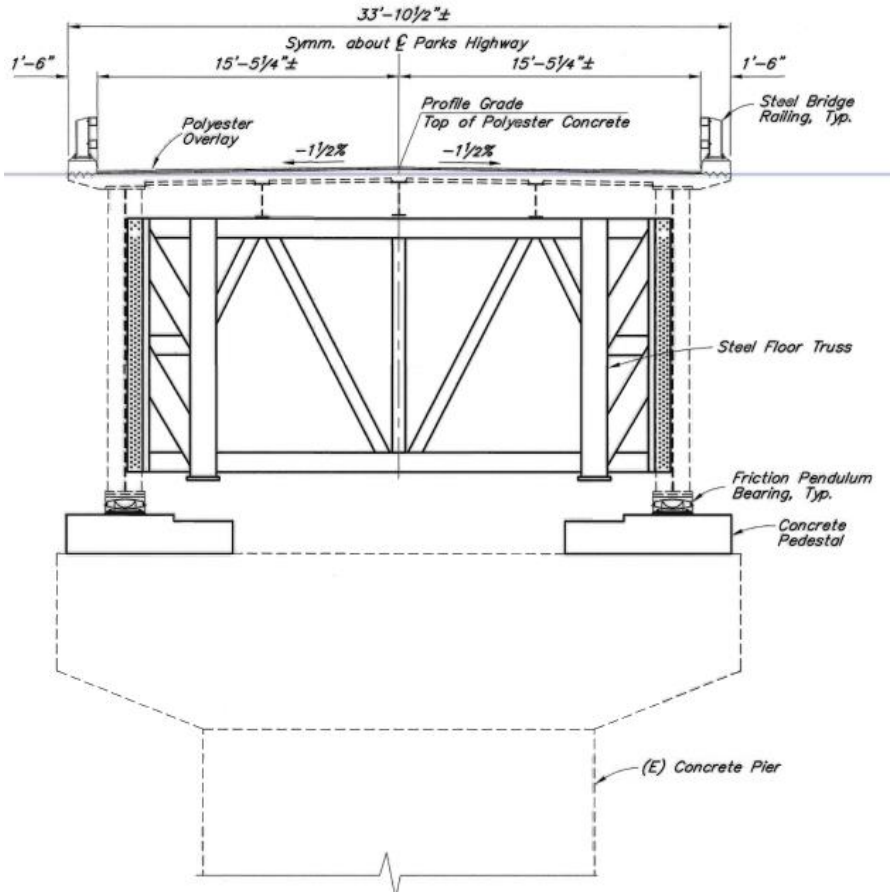

Figure 3.6. Susitna River Bridge cross section (Alaska DOT, 2006)

After the bridge's construction in 1965 it was retrofitted in 2007 for the updated seismic demands at the bridge location by installing 2 types of DPB: Type 1 in the piers, and Type 2 in the abutments. A total of 12 DPB were installed to retrofit the bridge. For this study, 2 abutment bearings (Type 2) bearings will be removed and replaced to permit the formerly in-service bearings to be tested. Additionally, 1 new DPB with the same properties and geometry as Type 2 in-service bearings will be tested to compare the response of a new bearing against the response of formerly in-service bearings. Testing on new and in service bearings will provide a way to assess how the bearings properties change due to environmental in-service conditions such as wear and the freezing – melting

cycle. Properties of the bearings to be tested are shown in Table 3.3, with reference to the generalized cross-section in Figure 3.7. Figure 3.8 shows the dimensions on a cross section of Susitna Bridge Type 2 bearing.

Table 3.3. Susitna Bridge bearing type 2 properties

Displacement Capacity ($2d_1$) (in)	d_T	±11
Effective Radius ($2R_1$-$2h_1$) (in)	R_e	74
Dynamic Period (s)	T	2.75
Coefficient of friction	μ_1	0.075
Min. Rotation Requirement (degrees)	-	2
Max. D+L Load (kips)	-	300

\

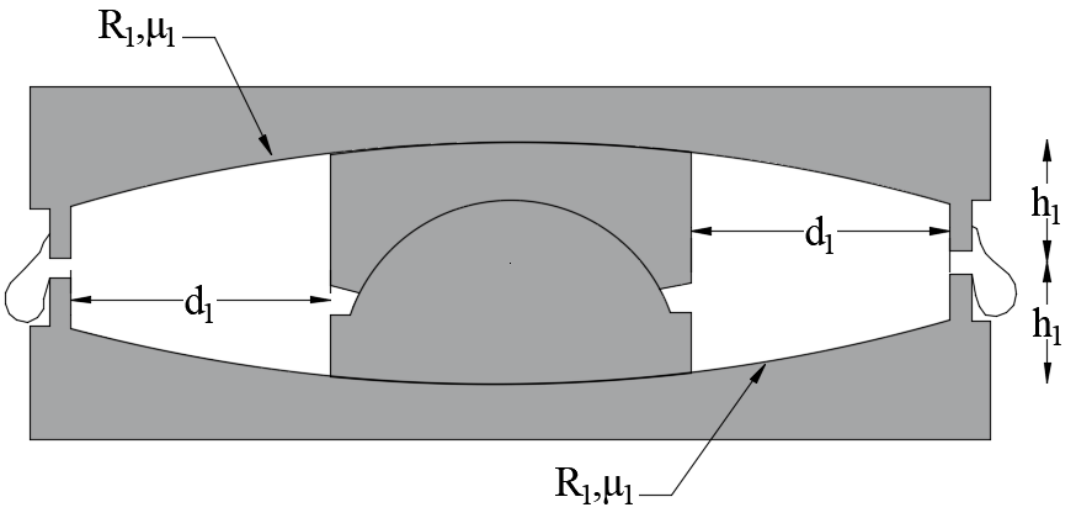

Figure 3.7. General cross section of DPB

Since frictional properties and geometry are the same for both sliding surfaces, Equation 3.1 is used to calculate T for Susitna Bridge bearing.

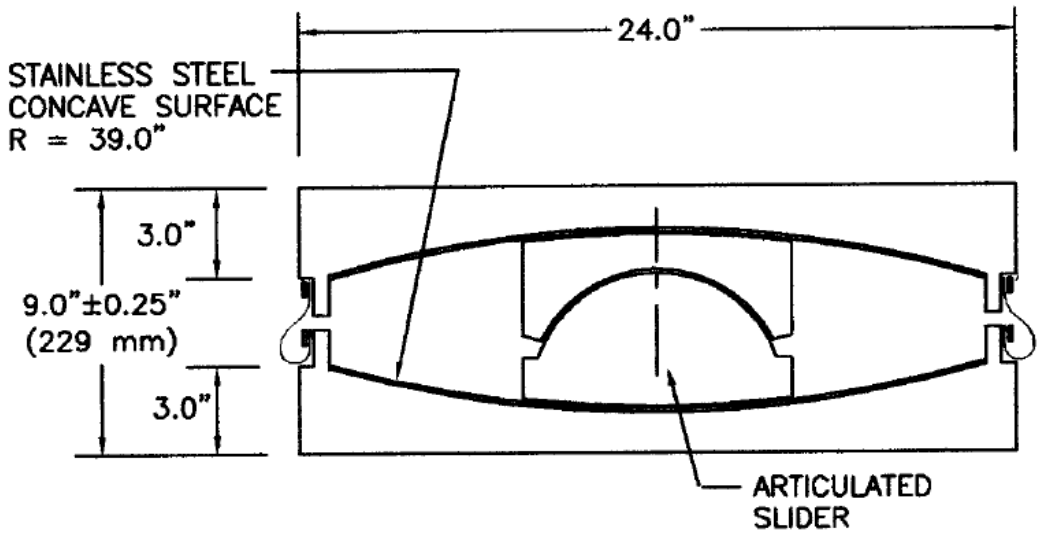

Figure 3.8. Susitna Bridge bearing cross section

The design approaches described above were also applied to derive design parameters for Susitna Bridge bearings. The design parameters for both approaches is shown in Table 3.4.

Table 3.4. Susitna Bridge bearing design parameters

	AASHTO 1999	**AASHTO 2010**	
Spectral Parameters			
AS*	0.32	-	g
S_s	-	0.4164	g
S_1	-	1.025	g
Soil type	-	0.3714	-
PGA	-	B	g
S_{DS}	-	0.4855	g
S_{D1}	-	1.0251	g
Bearing Response			
W**	106	106	kips
$\mathbf{K_{eff}}$	3.887	3.365	kips/in
$\mathbf{T_{eff}}$	4.313	1.743	s
$\mathbf{B_{eff}}$	0.425	0.381	-

B_L	1.906	1.700	-
D	2.576	3.7238	in
F	11.109	12.532	kips
*Represents acceleration coefficient amplified by site coefficient. ** Max D+L capacity is 300 kips			

Equations 3.2 through 3.4 were also used to calculate D and F for Susitna Bridge bearing. Design values used for the design of the test set up components will be discussed in chapter 4.

3.2. Test Set Up Overview

The FPS bearings will be tested using the arrangement shown in Figure 3.9. The test arrangement is designed to use the shake table as an actuator to apply a dynamic displacement history to the bearing, moving the bottom concave plate while keeping the top plate stationary. A cantilevered A-frame restrains the bearing top plate from displacement in any direction. The A-frame rests on the specimen at point C and is pin-connected to rigid wide flange steel columns at points A and B, which constrains the specimen top plate against lateral movement. Also, the pin connections at A and B allow the A-frame to rotate up in order to swap bearings between the tests. Connections A and B will be discussed later on this chapter.

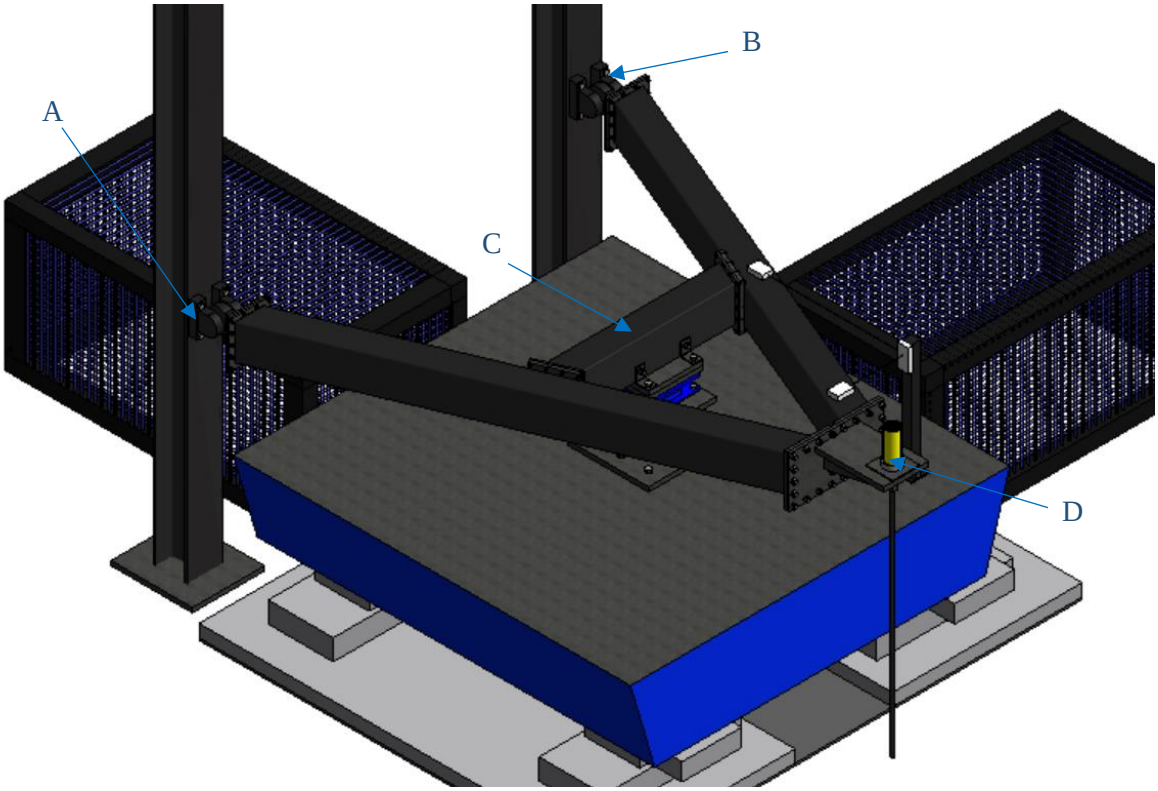

Figure 3.9. Isometric view of test set up arrangement

The A-frame was designed to transmit a controlled axial load to the bearing as well. The relation between the external load at D and the reaction at C is shown in Figure 3.10. The vertical reaction on the bearing at C is approximately twice the load applied at D, such that a 60 ton hydraulic ram is sufficient to apply a 100 kip load at D. A load cell located between the hydraulic ram and the plate assembly at end D measures the axial load provided by the hydraulic ram (Figure 3.11).

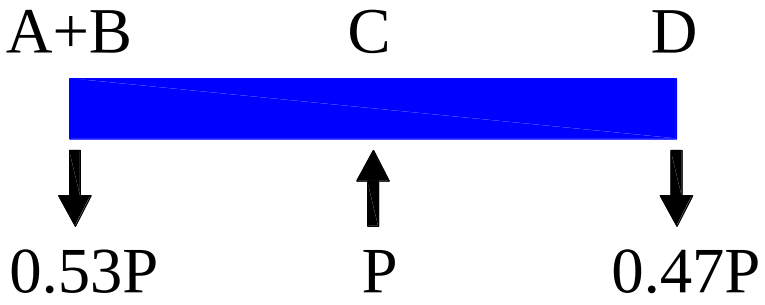

Figure 3.10. Cantilever A-frame free body diagram

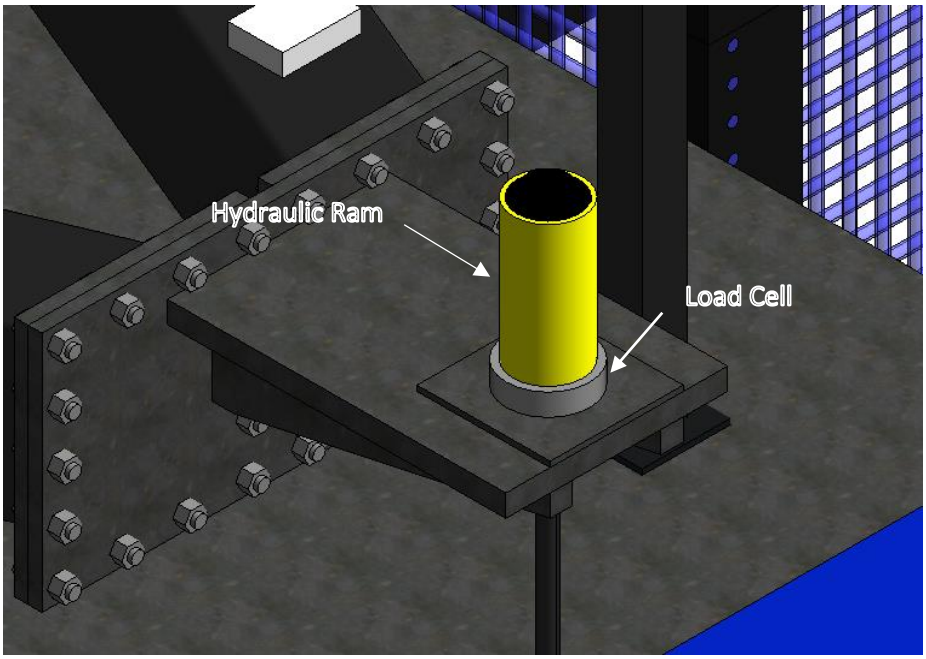

Figure 3.11. Hydraulic ram arrangement

Figure 3.12 shows the elevation view of the bearing load path from the shake table to the A-frame on top of the bearing. The vertical arrangement shown in Figure 3.12 was designed to transmit axial load from the A-frame to the bearing, restrain the bearing top plate from translation in all directions, and facilitate measurement of both shear and axial forces in the bearing. The axial and shear force in the bearing will be measured by a load

cell located beneath it. The vertical arrangement to transmit vertical loads from the A-frame down through the bearing and the load cell consists of the following: A-frame connected to the bearing with a set of angles and adapter plate(s) B3, and bearing connected to the load cell by the adapter plate B2. Plate B1 is a base plate to connect the load cell to the shake table. For the Robertson SPB a second B3 adapter plate is needed to accommodate for the difference in height between the Robertson SPB and the Susitna DPB (Figure 3.12(a)). Only a single B3 adapter plate is used for the Susitna DPB (Figure 3.12(b)).

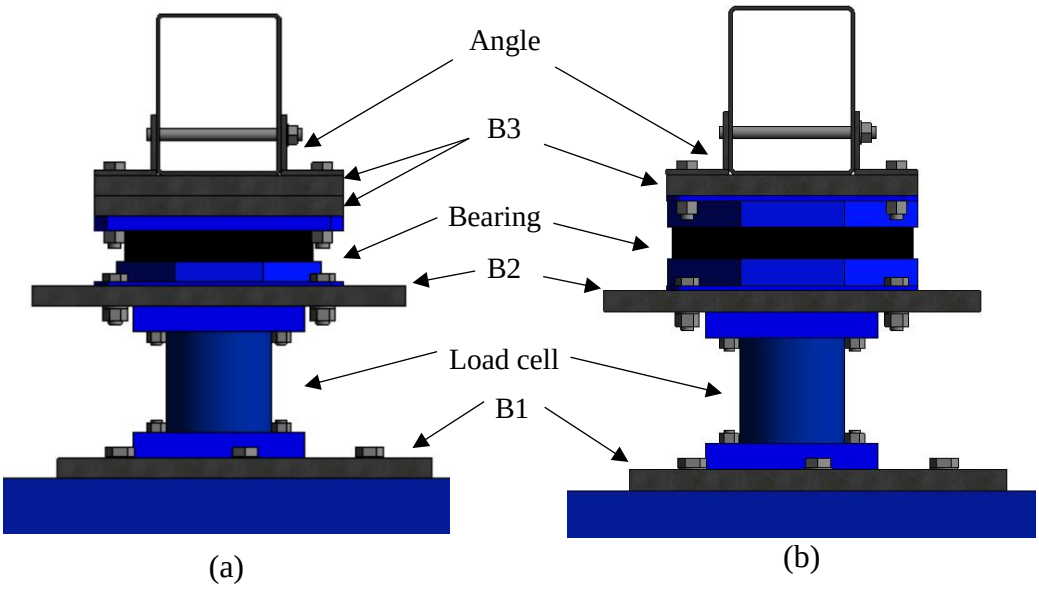

Figure 3.12. Load cell to Bearing to A-frame arrangement (a) Robertson River Bridge bearing (b) Susitna River Bridge bearing

Given the geometry of the sliding surface, the bearing top plate must be able to rotate in order to accommodate the displacements. The pin connections at A and B consists of swivels bolted to the rigid steel columns on one end and to the A-frame on the other end, allowing the A-frame to rotate as needed by the bearing. Adapter plates are used to achieve

the connection between the swivels and the A-frame (Figure 3.13). Further details on the connection design will be presented in Chapter 4.

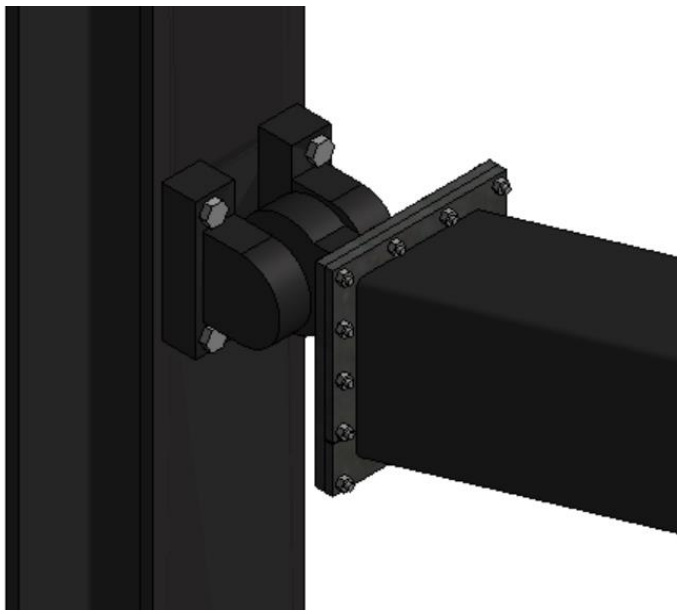

Figure 3.13. Pin Connection at A and B

3.3. Insulation Box Design

To freeze water in the bearings prior to conducting a "frozen bearing" test, a wraparound insulation box assembly will be applied. After being axially loaded, the bearing will be surrounded by an insulating box filled with dry ice and left to freeze until it reaches the target temperature. The insulating box, with dimensions 36 in x 36 in x 11 in, will be made from approximately 2.00 in thick insulating material like polystyrene, polyurethane or fiberglass. The insulation box rests on plate B2 and flushly surrounds plate B3 as shown in Figure 3.14.

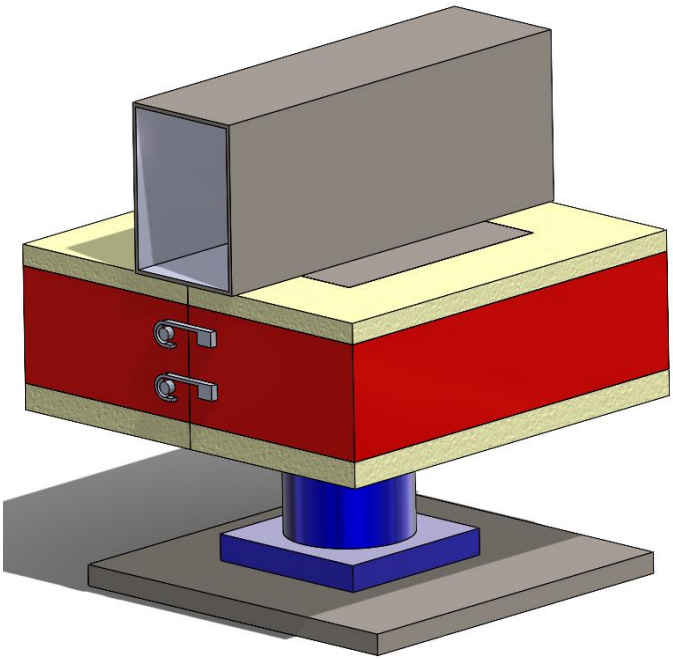

Figure 3.14. Insulation box layout

The insulation box will be constructed in 4 pieces: 2 wall plus bottom pieces and 2 top lid pieces. The lid pieces, which are aligned with the top stationary part of the bearing, will be removed, while the bottom pieces, which are aligned with the bottom moving part of the bearing, will be left in place during seismic testing, Extra insulation foam will be placed inside the box to minimize the amount of dry ice needed and keep the dry ice closer to the bearing. Gaps in the insulation box will be filled using a flexible insulator such as fiberglass pipe wrap. Figure 3.15 shows geometry of the insulation box.

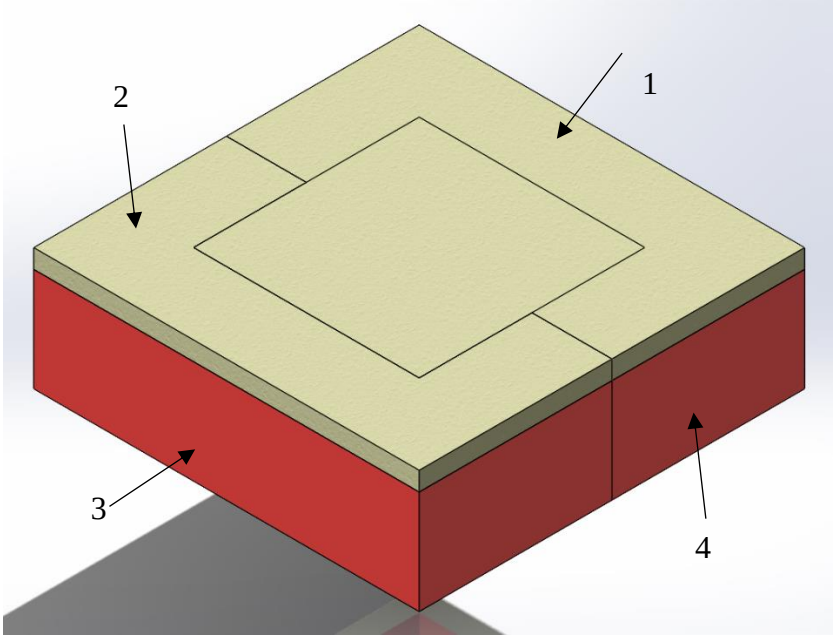

Figure 3.15. Pieces of insulation box

3.4. Instrumentation

As mentioned previously, two load cells are included in the set up to measure the bearing forces. LC01 is a triaxial load cell that measures forces passing through the bearing in three translational directions. LC02 is a uniaxial load cell located underneath the hydraulic ram that measures the vertical force passing through the hydraulic ram. Both load cells are shown in Figure 3.16.

(a) (b)

Figure 3.16. Load cells (a) LC01 (b) LC02

To measure relative displacement in both horizontal directions between shake table and the A-frame two string pots will be used. Since the deformation of the A-frame is negligible when compared with the bearing's displacement, the measured displacements will equate to the total displacements of the bearing. String pots to be used are shown in Figure 3.17.

Figure 3.17. String pots

The string pots will be implemented as shown in Figure 3.18. A small steel column will be used to set the string pots to the shake table and the other side of each string pot will be located on top of the A-frame in both horizontal directions.

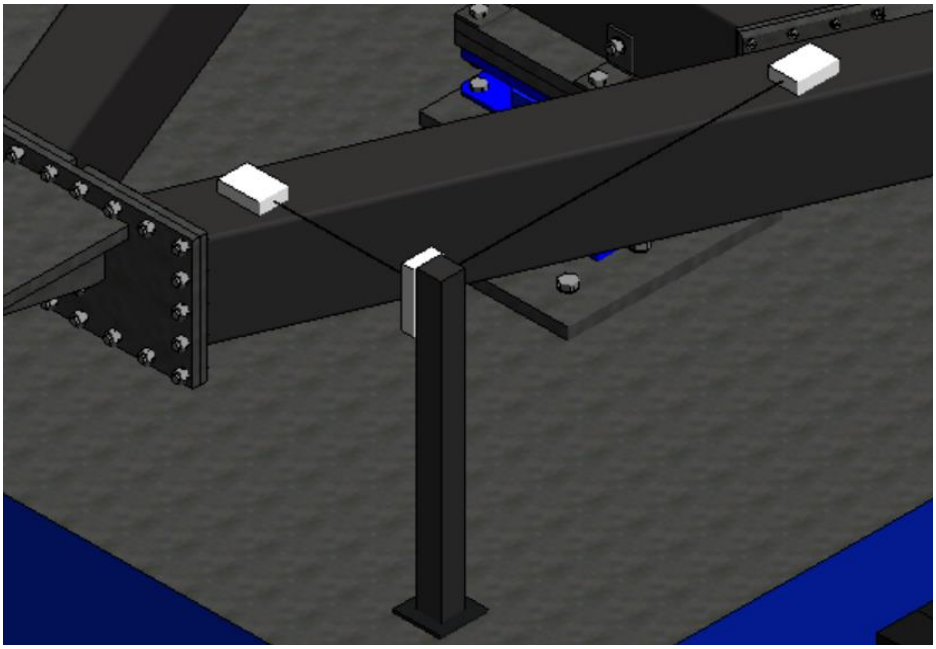

Figure 3.18. String pots set up

Chapter 4. Design of the A-frame

4.1. Geometry

As part of the test set up, an A-frame was designed (Figure 3.7) in order to restrain the bearing top plate and to axially load the bearing. The A-frame consists of three steel HSS 16x12x3/8" elements, two legs with lengths of $15' - 8\frac{3}{8}$", $15' - 8\frac{3}{8}$" a cross element with length $6' - 7\frac{11}{16}$", and a plate assembly. A plan view of the frame is shown in Figure 4.1 and an elevation view is shown in Figure 4.2. On the left end, the legs of the A-frame are connected to rigid W14x176 steel columns, using a swivel to allow for rotation (Details 01 and 02). The cross element is connected to the bearing using four 6x6x1/2" angles bolted on one end to the A-frame and on the other to top adapter plate, as shown in Figure 3.12. On the right end, there is a plate assembly (Detail 04) where the external load is applied using a hydraulic ram, the load is transferred by the A-frame to the bearing as axial load.

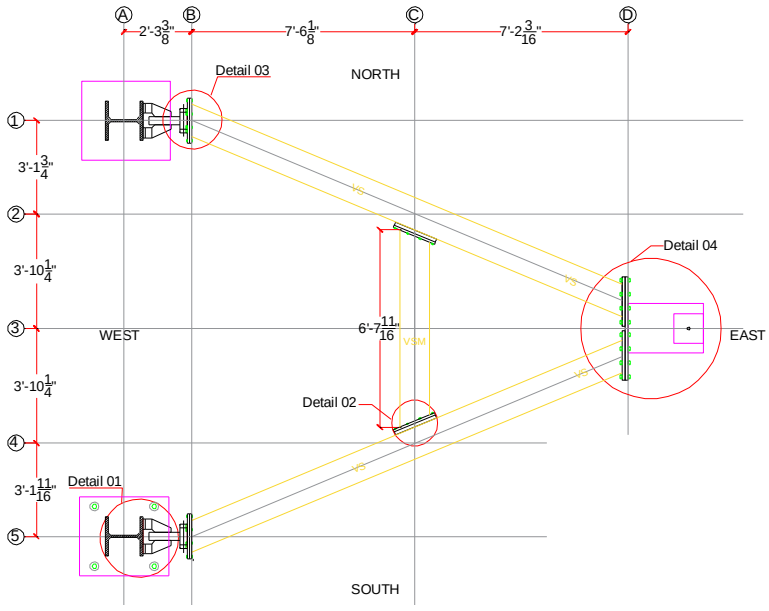

Figure 4.1. A-frame plan view

The A-frame will be connected to the steel column $8' - 5\frac{1}{8}"$ from the ground, as shown in Figure 4.2. However, since the swivels will be bolted directly to the flanges of the steel columns, the height of the set up can be modified to reuse the frame for future testing needs by simply bolting the swivels to the steel columns at a different location.

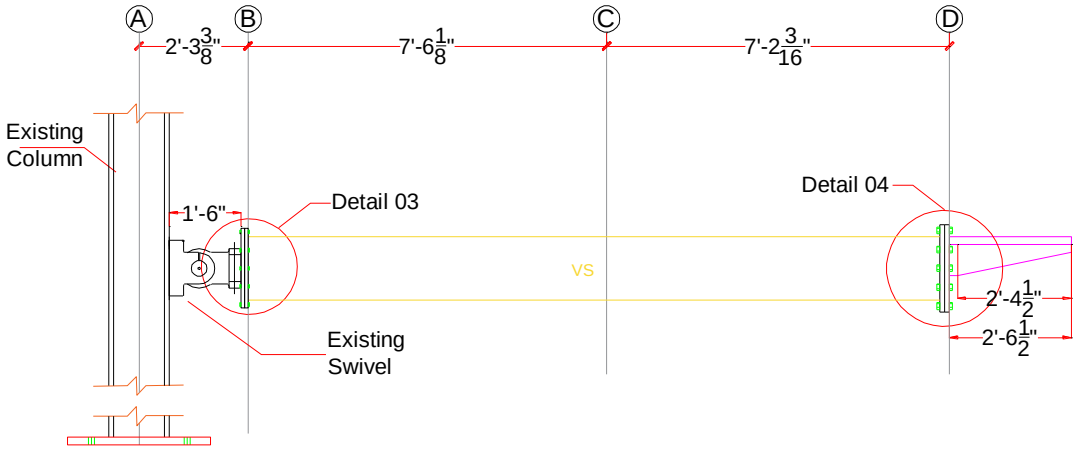

Figure 4.2. A-frame south elevation view

4.2. Loads

4.2.1. Vertical Loads

The A-frame must be able to withstand the axial load on the bearings, 18 and 106 kips for Robertson and Susitna Bridge bearings, respectively. However the shake table's vertical load capacity is 100 kips, hence the design vertical load is 100 kips. A free body diagram of the A-frame was shown in Figure 3.9, which establishes the relationship between the load applied at the plate arrangement (Point D) and the load transmitted to the bearing (Point C). To achieve a reaction of 100 kips on the bearing (Point C), a load of 47 kips should be applied at point D (Detail 04).

4.2.2. Horizontal Loads

Bearings response calculated in Chapter 3 is based on the design displacement. On previous tests of ice filled FPS bearings conducted by Tappan Zee Constructors (Tappan Zee Constructors, 2017), ice contamination did not increase the ultimate shear resistance. However, given that there is still uncertainty on the effect of ice on the bearing's response, the shear force was calculated using the maximum displacement capacity of the bearings to allow for some conservatism. The following equation was used to calculate shear force.

$$V = \mu W + \frac{W}{R}u \tag{4.1}$$

where:

V = Shear Force
μ = Breakaway coefficient of friction
W = Vertical load applied
R = Effective Radius
u = Displacement

Parameters such as u and R were obtained from bearings specifications, shown in the previous chapter in Tables 3.1 and 3.3. For Susitna River Bridge bearings, W is taken as the shake table capacity, 100 kips. For Robertson River Bridge bearing, the maximum axial load capacity of 47 kips was used for W, instead of shake table's capacity. A 5% increase in μW term was assumed for both bearings to account for possible variations in breakaway friction when testing water and ice contamination. Coefficient of friction, μ, was obtained from bearings previous qualification tests done by EPS. The bearing shear force at maximum displacement is shown in Table 4.1.

Table 4.1. Bearings shear force at maximum displacement

	Susitna Bridge Bearing	**Robertson Bridge Bearing**
u (in)	11	6
W (kips)	105	49.35
R (in)	74	61
μ(unitless)	0.07	0.10
V (kips)	22.96	9.79

A factor of safety is calculated by comparing the bearing force based on displacement capacity (Table 4.1) with the design force in Tables 3.2 and 3.4. Factors of safety for Robertson and Susitna Bridge bearings, respectively, were calculated using the following equations:

$$FS_R = \frac{9.79}{2.995} = 3.27 \tag{4.2}$$

$$FS_S = \frac{22.96}{12.53} = 1.83 \tag{4.3}$$

Shear force values shown in Table 4.1 are for unidirectional movement of the bearings. To account for bidirectional movement, the displacement capacity of the slider is applied in the 45° direction from X-axis, as shown in Figure 4.3.

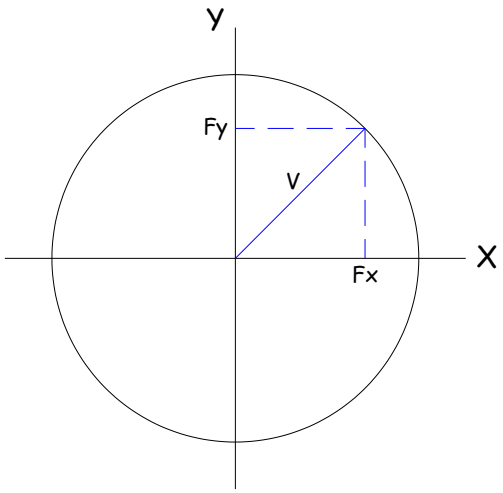

Figure 4.3. Bearing bidirectional movement

With the previous assumption, projected forces Fx and Fy in X and Y directions are calculated for bidirectional loading using the following equation:

$$F_X = F_Y = V\cos(45) \tag{4.4}$$

A summary of horizontal loads is presented in Table 4.2. Note that shear force, unidirectional and bidirectional, for Susitna River Bridge bearing is larger than shear force for Roberson River Bridge. Hence the forces in the Susitna bearing control the design of the A-frame.

Table 4.2. Horizontal forces summary

	Robertson Bridge Bearing	**Susitna Bridge Bearing**
V (kips)	9.79	22.96
Fx (kips)	6.92	16.23
Fy (kips)	6.92	16.23

4.2.3. Load Combinations

In developing load combinations for design, load factors were not applied as the basis for the bearing loads were well established and other sources of conservatism were applied. The vertical load applied to the A-frame is controlled by the hydraulic ram and measured continuously by a load cell, and thus the axial load on the bearing is limited to the values presented in section 4.2.1. Likewise, the ultimate shear based on the displacement capacity of the Susitna River Bridge bearing (22.96 kips), is substantially larger than the design shear for either bearing (safety factor of 1.8 for Susitna and 3.3 for Robertson, per Equations 4.2 and 4.3). Load combinations used are shown below:

(a) D

(b) D ± Vx

(c) D ± Vy

(d) D ± Fx ± Fy

where, D represents dead load, Vx and Vy are maximum horizontal load in x and y due to bearing peak displacement applied unidirectionally in x and y, respectively, and Fx and Fy are maximum horizontal loads in x and y due to bearing peak displacement applied bidirectionally.

4.3. Structural Model

The A-frame was analyzed using CSI software SAP2000. Figure 4.4 shows an extrude view of the model. The model included the major structural members modeled as

frame elements as it was used to select and validate frame section sizes. The A-frame is shown in red and the wide flange steel columns are shown in light blue. Since the model does not include connection details, the connection between the A-frame and columns was modeled as a simple pin connection by releasing the end moments. The connection between the A-frame and the bearing was modeled using a roller connection. The plate arrangement on Detail 4 (Figure 4.1) was modeled by creating a special node at the point of load application/hydraulic ram. This special node and the frame end nodes connected on Detail 04 are tied together using a body constraint (Figure 4.4). A separate model was built to analyze the plate arrangement on Detail 04, which will be discussed later.

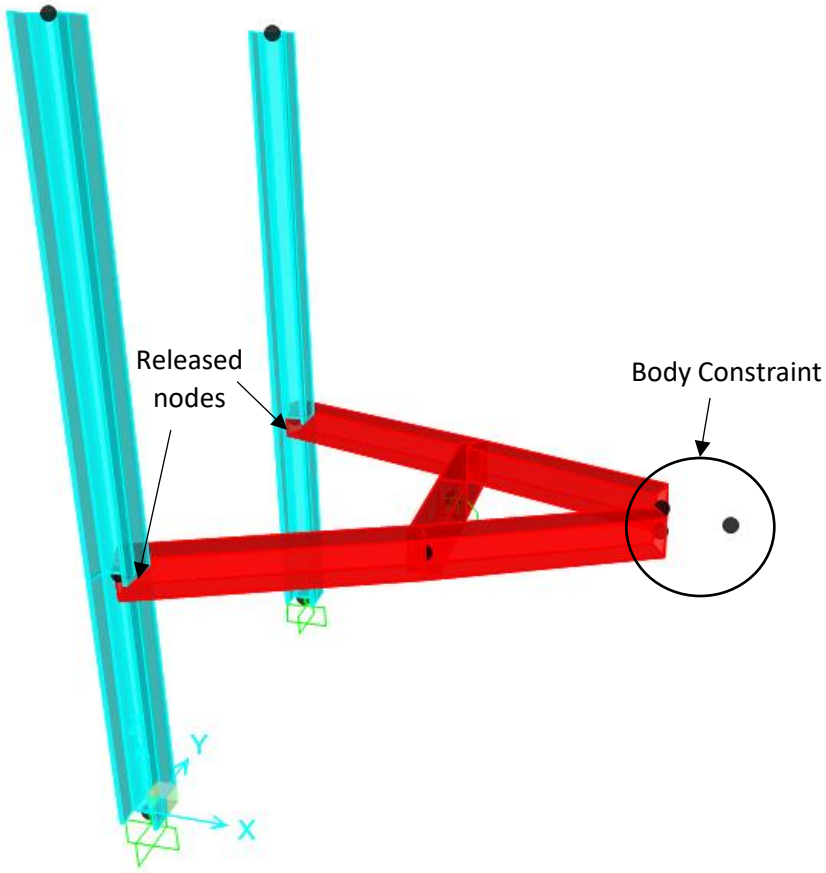

Figure 4.4. A-frame analytical model extrude view

4.4. Design of Frame Leg and Cross Elements

A linear analysis was performed to calculate the internal forces in the elements of the A-frame. To calculate the demands on the structure, the combination of moments that resulted in the highest stress in the elements was chosen. The structure moment envelopes considering all load combinations for strong and weak axis are shown in Figure 4.5; columns are not shown since they are not part of the A-frame design.

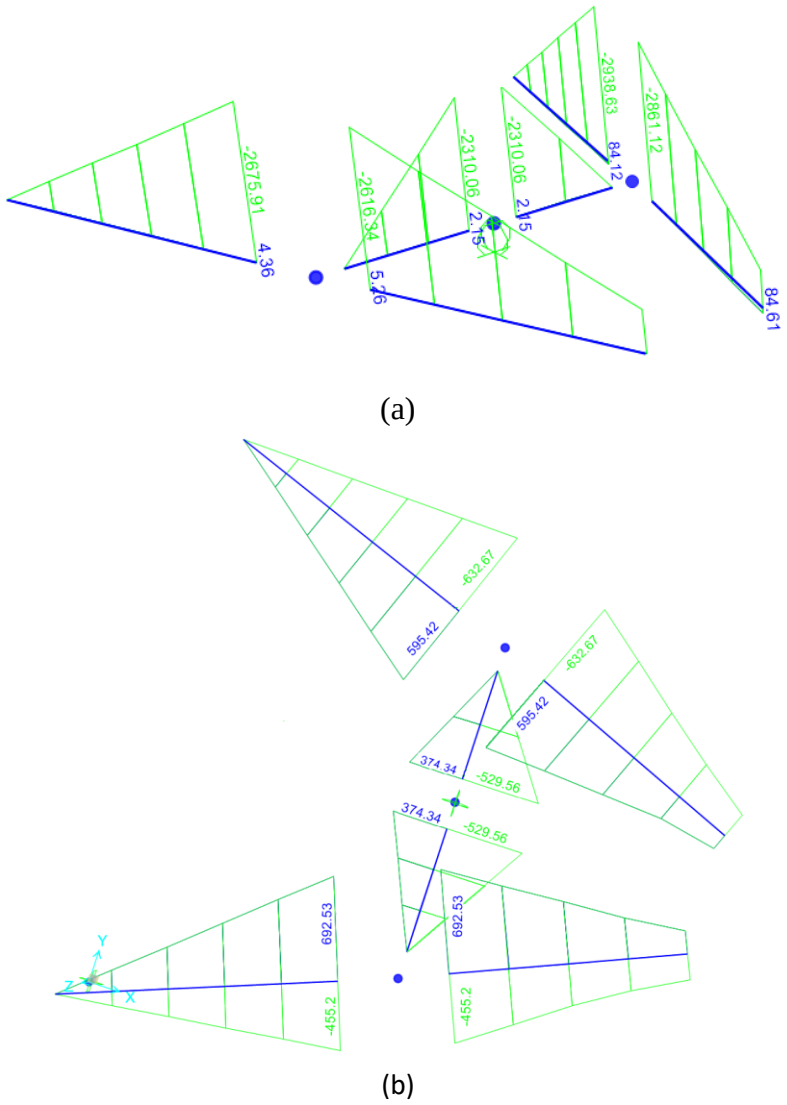

Figure 4.5. A-frame moment envelope diagram, kip-in (a) Strong axis (b) Weak axis

Elements in the A-frame need to resist bending about weak and strong axis separately, and biaxial bending as well. Material and section properties were chosen according to AISC Steel Construction Manual (AISC, 2005). No yielding was allowed in any fiber of the elements and LRFD strength resistance factors were applied to the capacity of the elements. The material used in the design of the elements was ASTM A500 Grade C. Given that HSS sections facilitate simpler connection between the A-frame elements and its connection to the bearings, and that HSS have good flexural resistance in weak and strong axis, the A-frame was designed using HSS sections. HSS 16x12x3/8" was the minimum section to meet the criteria. Section and material properties are shown in Table 4.3.

Table 4.3. Section and material properties

b (in)	12	Width
h (in)	16	Height
t (in)	3/8	Thickness
fy (ksi)	46	Yield strength
fu (ksi)	62	Tensile strength
Sx (in^3)	87.7	Section modulus strong axis
Sy (in^3)	75.3	Section modulus weak axis
Mnx (kips-in)	3630	Moment capacity strong axis
Mny (kips-in)	3117.42	Moment capacity weak axis

To determine demand-capacity ratio for total flexural capacity of the element, each load combination described in section 4.2.3 was evaluated using the following equation:

$$\frac{Mux}{Mnx} + \frac{Myx}{Mny} \leq 1 \tag{4.5}$$

where Mux and Myx are the ultimate moments with respect to strong and weak axis, respectively, and Mnx and Mny are the moment capacity with respect to the strong and weak axis respectively. Load combination D ± Vy, which maximizes stress in the lateral longer elements, controlled the design. Results are shown below.

$$\frac{2675}{3630} + \frac{692}{3117} = 0.96 \leq 1$$

The effect of frame member axial force was negligible, and thus it is not included in the interaction equation. The element is then adequate to resist the loads required by the test set up, without yielding on any fiber of the section.

4.5. Design of Connections

As mentioned previously, the frame was designed with bolted connections between the pieces so that it can be easily assembled on site. Each frame element has a welded plate at the connection location, and then the plates in each connection are bolted together. Welds and bolts have been designed in accordance with AISC 360 (AISC, 2010). Figure 4.6 shows the location of each connection. Material to be used in all connection plates is A36. Bolt material is A325 for connections C1 and C2 and A490 for connection C3. All welds are be

E7018 fillet welds. Table 4.4 shows material properties for the various steel specifications used in the connections.

Table 4.4. Connection material properties

Material	fy (ksi)	fu (ksi)	Use
A36	36	58	Plates
A325	92	120	Bolts in C1 and C2
A490	113	150	Bolts in C3

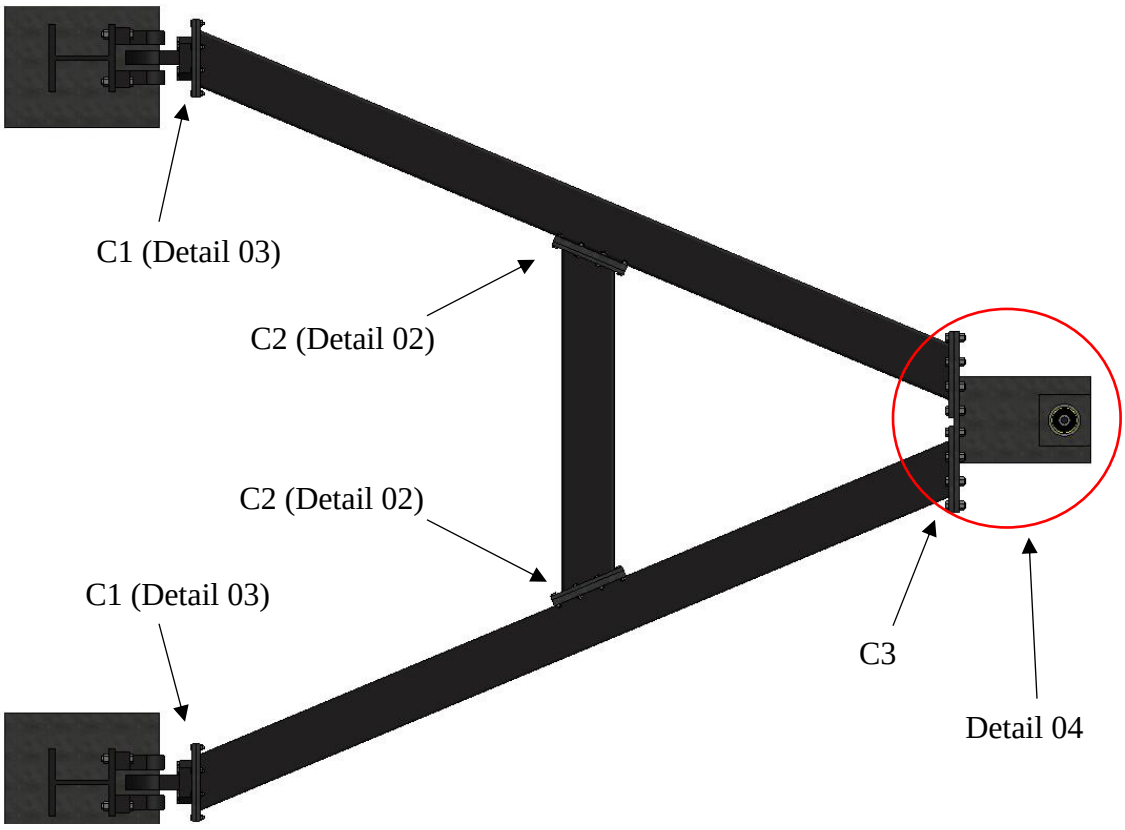

Figure 4.6. Connection locations

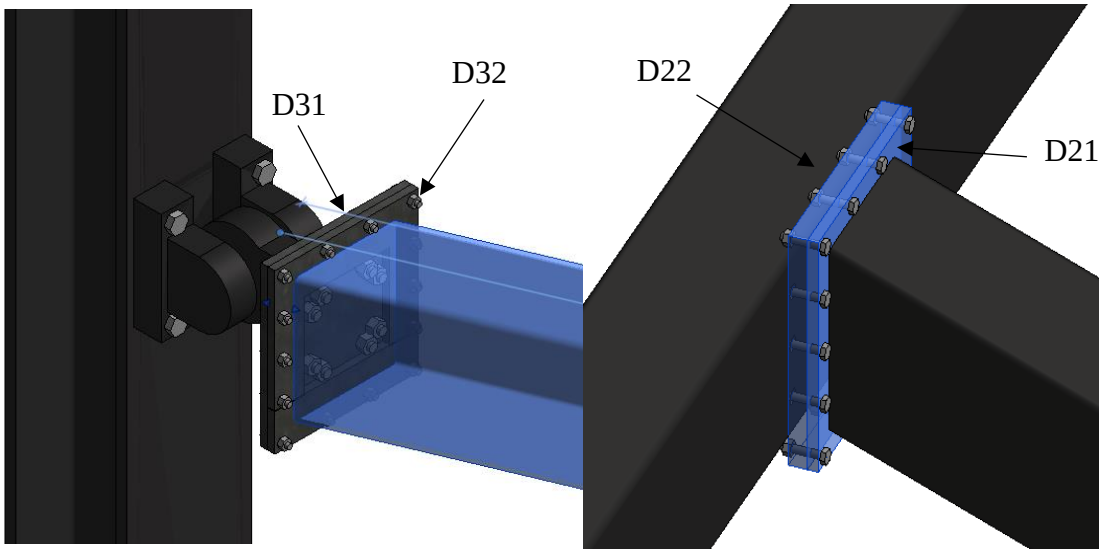

Figure 4.7. Connection details: (a) Connection C1 at Detail 03 (b) Connection C2 at Detail 02

Figure 4.7 shows connections C1 and C2. Connection C1 (Figure 4.7 (a)) consists of a 20x18x7/8" plate (D31) bolted to the swivel using 8 x 1" through bolts, and a hollow 20x18x7/8" plate (D32) welded to the A-frame. For frame assembly, plates D31 and D32 are bolted together using 14 x 5/8" through bolts. Connection C2 (Figure 4.7(b)) consists of a 20x18x1$\frac{3}{8}$" plate (D22) with 14 x 5/8" tapped holes, welded to the leg of the A-frame; and a 20x18x$\frac{7}{8}$" plate (D21) welded to the center element of the A-frame; for frame assembly plate D21 is bolted to plate D22. The following equations (Nord-Lock Group, 2015) were used to calculate minimum thread length in the connection:

$$L_{eth} = \frac{R_m^s}{R_e^{th}} \frac{2A_s}{0.6\pi d} \tag{4.4}$$

$$L_{es} = \frac{R_m^s}{R_e^s} \frac{2A_s}{0.6\pi(d - 0.6495p)} \quad (4.5)$$

where,

R_m^s = Bolt ultimate strength
A_s = Stress surface
R_e^{th} = Plate yield strength
d = Bolt diameter
R_e^s = Bolt yield strength
p = Distance between threads

The maximum of L_{eth} and L_{es} determines the thread length, and minimum thread length was the governing parameter when choosing the thickness of plate D22. Lengths L_{eth} and L_{es} were found to be 1.28 and 0.53 in, respectively. Hence, D22 plate thickness of 1-3/8" was found to be sufficient.

4.6. Finite Element Analysis of Detail 04

4.6.1. Model Description

Figure 4.8 shows connection C3 and the plate arrangement on Detail 04. For connection C3, a plate D41 is welded to each leg of the A-frame, and plate D43, which receives the load from the hydraulic ram, is welded to plate D42. For frame assembly, plate D42 is connected to the two plates D41 of the A-frame by 28 high strength A490 1" bolts. The hydraulic ram (not shown in Figure 4.8) will be directed through the hole on the small blue plate to transfer the load through end D to the frame. Plate D43 is supported by two stiffeners below to withstand the load imposed by the hydraulic ram.

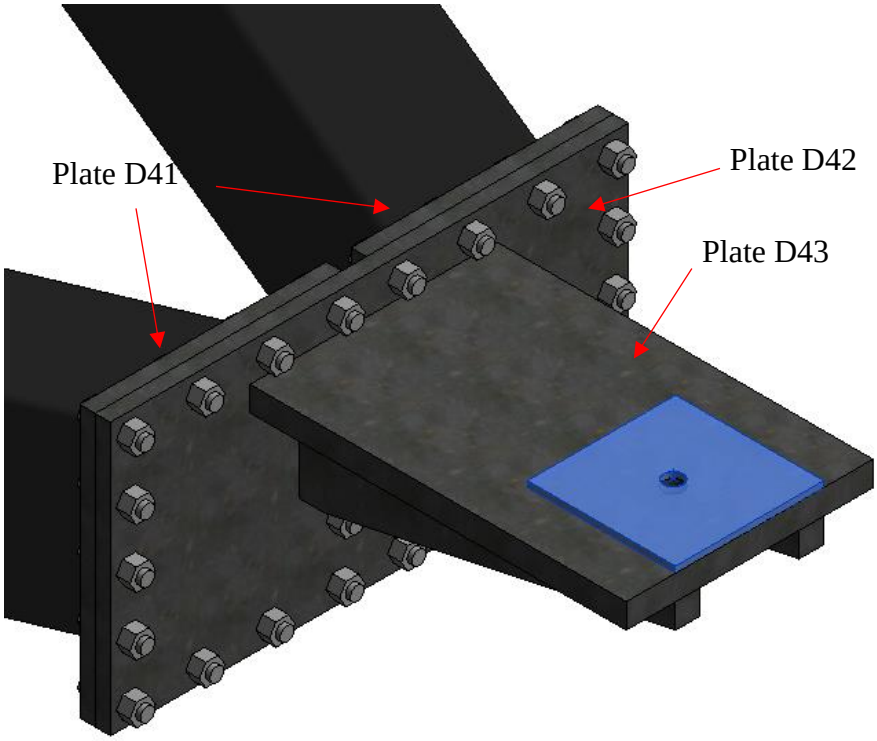

Figure 4.8. Connection C3 and plate arrangement on end D

The eccentricity between the location of the hydraulic ram and plate D42 (24 in), generates a large moment in the connection between plates D43 and D42. Also, Plate D43 and stiffeners are asymmetric with respect to plate D42, such that the forces are not uniformly distributed along the bolts and stress concentration is expected close to the welded connection on plate D42. Hence, a separate finite element model was created using SAP2000 to calculate stress on plates, bolts and welds on the plate arrangement on Detail 04.

In the SAP model, all plates and stiffeners were modeled using shell elements. Plates D43 and D42 were modeled while plate D41 was not included as it was considered

part of the A-frame and not part of the plate arrangement on end D. Displacement in all directions was restrained at the bolt locations to model the connection with the A-frame. Figure 4.9 illustrates the SAP2000 model.

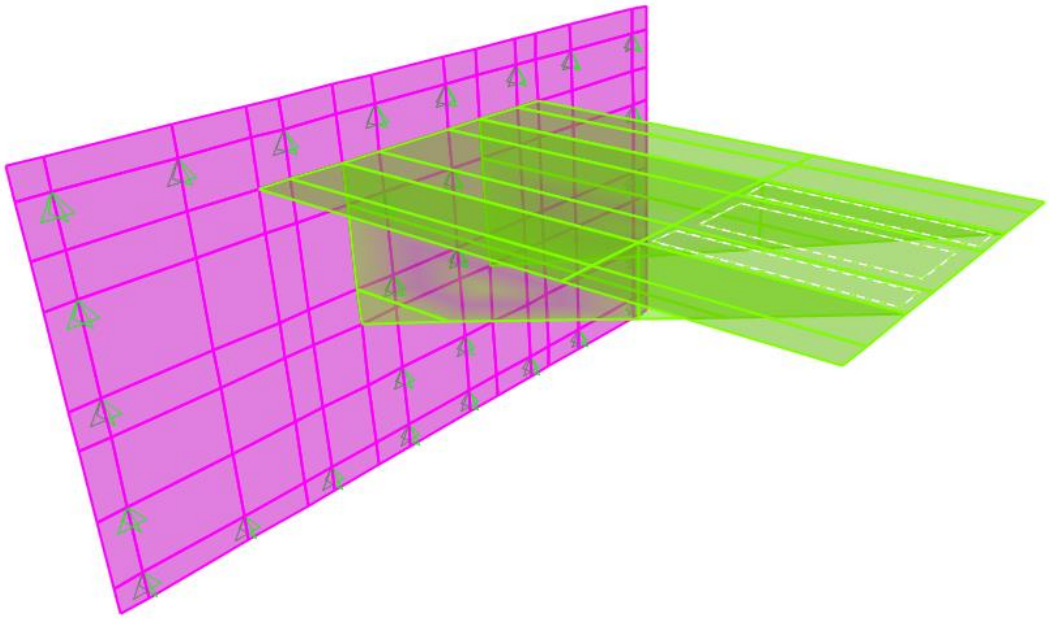

Figure 4.9. Plate arrangement on Detail 04 structural model

A load of 0.417 kips/in^2 was applied over the highlighted shell area of 120 in^2 (Figure 4.9), equivalent to the resultant load of 50 kips to be applied by the hydraulic ram. No influence of the horizontal loads was considered in this model.

4.6.2. Results and Design

For the bolts design, the reactions on the pin supports were used as the ultimate load on the bolts and tension shear interaction was analyzed using the following equation (AISC 360, 2010):

$$F'_{nt} = 1.3F_{nt} - \frac{F_{nt}}{\emptyset F_{nv}} f_{rv} \leq F_{nt} \quad (4.6)$$

where,

F'_{nt} = Nominal tensile stress modified to include effects of shear stress
F_{nt} = Nominal tensile stress
F_{nv} = Nominal shear stress
f_{rv} = Required shear stress
$\emptyset$ = Strength reduction factor, 0.75 for shear.

Figure 4.10 shows the reactions on each bolt. The bolt size was selected based on the maximum stress to any bolt, which is highlighted in Figure 4.10. The 1" diameter A407 bolts were chosen for Detail 04, which had a demand to capacity ratio of 0.49.

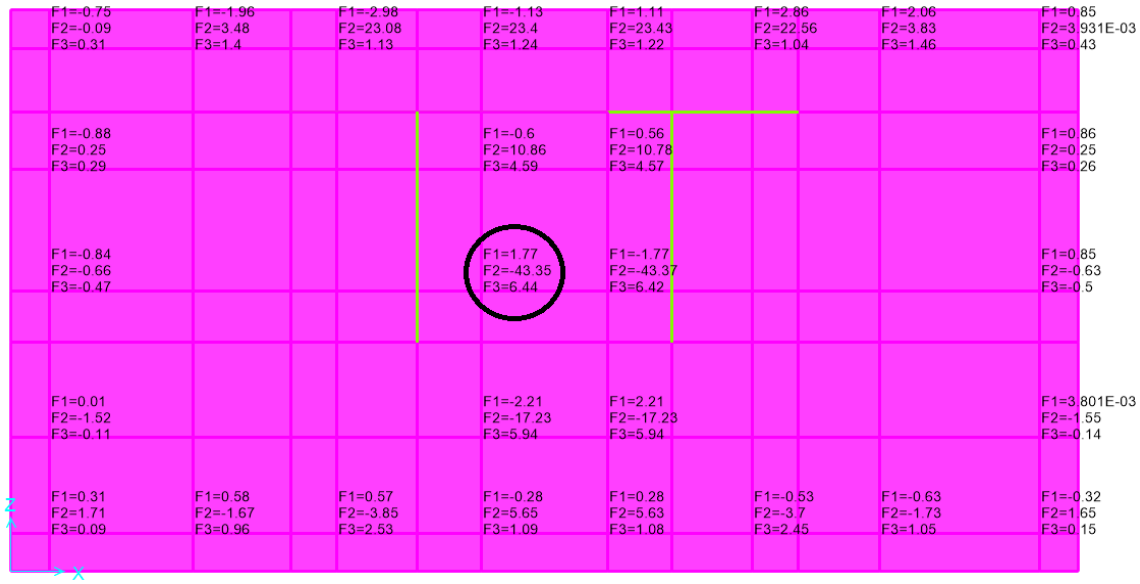

Figure 4.10. Reaction on bolts

Principal stresses on all the plates were also checked against the capacity of the section. Figures 4.11 and 4.12 show maximum and minimum stresses in plates D43, D42 and stiffeners normalized by the yielding stress of the steel elements.

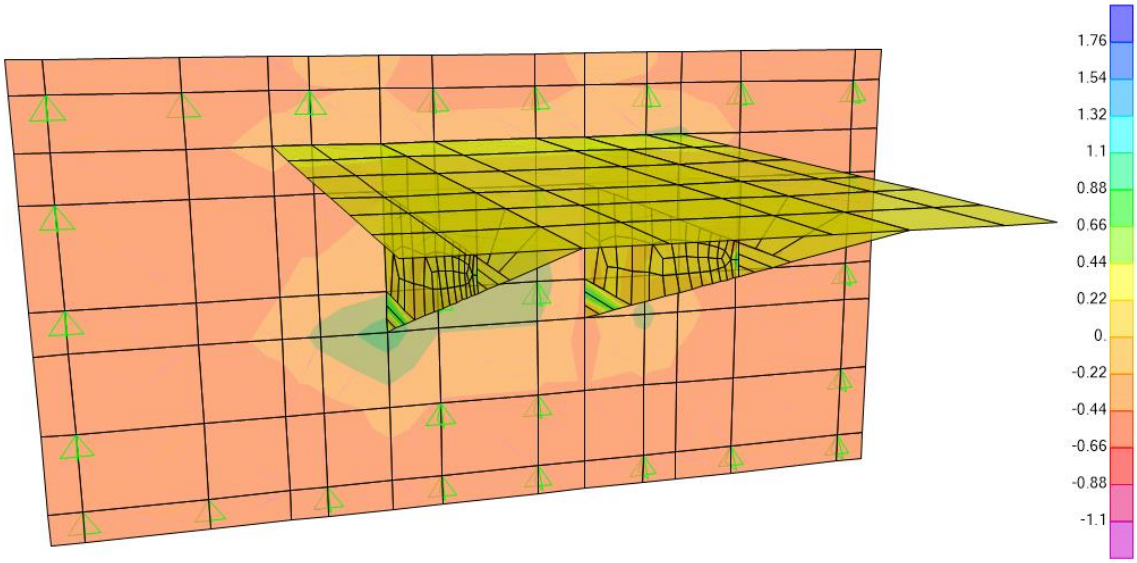

Figure 4.11. Normalized maximum principal stresses

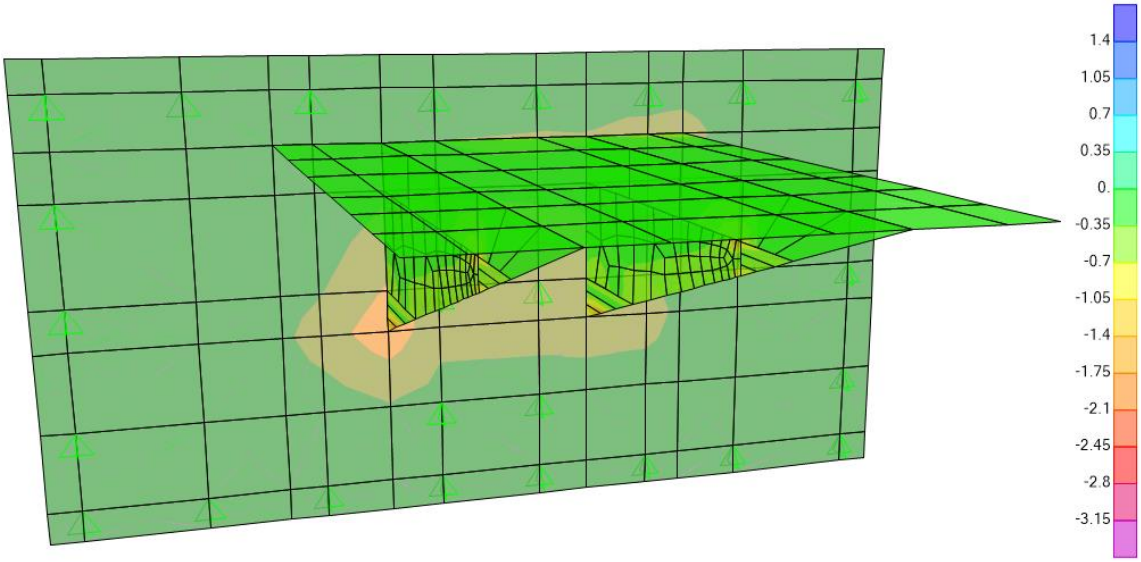

Figure 4.12. Normalized minimum principal stresses

The finite element output forces were not used to design welds. Welds were designed following AISC Steel Construction Manual (AISC, 2011), considering all the welds as a system. Flexural stress due to load eccentricity was combined with axial stress

due to the load to determine the total stress in the weld section. Then, weld capacity was calculated according to (AISC, 2010):

$$R_n = \emptyset 0.60 F_{EXX} A_w \quad (4.7)$$

where,

F_{EXX} = Filler metal classification strength
A_w = Welding effective area
$\emptyset$ = Strength reduction factor: 0.75.

An 7/16" E7011 weld was selected for plate D43 and stiffeners to plate D42 all around the perimeter of the connection, which produced a demand to capacity ratio of 0.99.

Chapter 5. Thermal Analysis

As described in previous chapters, part of the scope of this project is to assess how ice contamination affects the behavior of FPS bearings. To freeze water inside the bearings, an insulation box (introduced in Chapter 3) will be wrapped around the bearing and continuously filled with dry ice until the water freezes and reaches the target temperature. Hence, a finite volume model was built to asses if the insulation box will be effective to freeze water inside the bearing to the target temperature. Then, if the approach is feasible, determine the optimal insulation arrangement, the time needed for the water to freeze and the amount of dry ice needed.

5.1. Heat Transfer Mechanisms

There are 3 types of heat transfer mechanisms: conduction, convection and radiation. These three mechanisms are described in this section to explain what is happening in the system during the freezing and defreezing process. In the finite volume modeling, the main mechanism of heat transfer that takes place is conduction, but radiation is also considered within the domain of the model. Convection is only indirectly represented within the boundary conditions of the model.

5.1.1. Conduction

Heat conduction occurs within solid objects or stationary fluids. Energy transfers from molecules with higher molecular energy to molecules with lower molecular energy, hence the heat flows from higher temperature zones to lower temperature zones.

The Fourier law of heat conduction is (Bejan, 1993):

$$q_x = -kA\frac{\partial T}{\partial x} \tag{5.1}$$

This equation assumes that the heat flow q_x is proportional to the change in temperature T, with a proportionality constant, which means $q = C\,(T_x - T_{x+\Delta x})$. Moreover, C is proportional to $A/\Delta x$, or $C = kA/\Delta x$, where k is the solid thermal conductivity. Then, Equation 5.1 is obtained in the limit as $\Delta x \to 0$.

The first law of thermodynamics is described by following Equation:

$$q_x - q_{x+\Delta x} - \omega = \frac{\partial E}{\partial t} \tag{5.2}$$

where ω is the work done by the system and E is internal energy. In order to develop the conduction equation, Fourier's law is substituted into Equation 5.2, where ω becomes the internal heat generation and E is defined as:

$$E = (\rho A \Delta x)u \tag{5.3}$$

where ρ is density of the body. Then the specific internal energy u is proportional to the temperature change, hence $du = c\,dT$, where c is the specific heat of the body. Replacing E in Equation 5.2, the conduction equation for unidirectional heat transfer is obtained.

$$\frac{\partial}{\partial x}\left(k\frac{\partial T}{\partial x}\right) + \dot{q} = \rho c\frac{\partial T}{\partial t} \tag{5.4}$$

Equation 5.4 can be easily be extended for a 3-dimensional problem by including heat flux in three directions, obtaining:

$$\frac{\partial}{\partial x}\left(k\frac{\partial T}{\partial x}\right)+\frac{\partial}{\partial y}\left(k\frac{\partial T}{\partial y}\right)+\frac{\partial}{\partial z}\left(k\frac{\partial T}{\partial z}\right)+\dot{q}=\rho c\frac{\partial T}{\partial t} \tag{5.5}$$

5.1.2. Convection

Convective heat transfer is defined as the heat transfer process that is carried out by flow of a fluid or vapor. Energy is transported by the fluid into a solid object (or stationary fluid) or vice versa, depending on which is at a lower temperature (Bejan, 1993). Convective heat transfer is classified as natural convection when the fluid flows due to gravity or buoyancy effects, and forced convection when the fluid flow is forced around a solid of interest (e.g by using a fan).

The traditional approach to calculate the convective heat flow consists of calculating the local heat flow $q"$ using the following equation:

$$q" = h(T_w - T_\infty) \tag{5.6}$$

Local heat flow is proportional to the difference in temperature between the surface of the body T_w and the free-stream temperature T_∞. Heat transfer coefficient h depends greatly on the fluid characteristics, temperature distribution near the body surface and the fluid velocity. Depending on the previously mentioned variables, h can range from 1 to 106 W/m^3K. Sample ranges for heat transfer coefficient depending on the type of fluid and flow regime are shown in Figure 5.1. Equation 5.6 is then integrated over the surface of the solid to get the total convective heat flux.

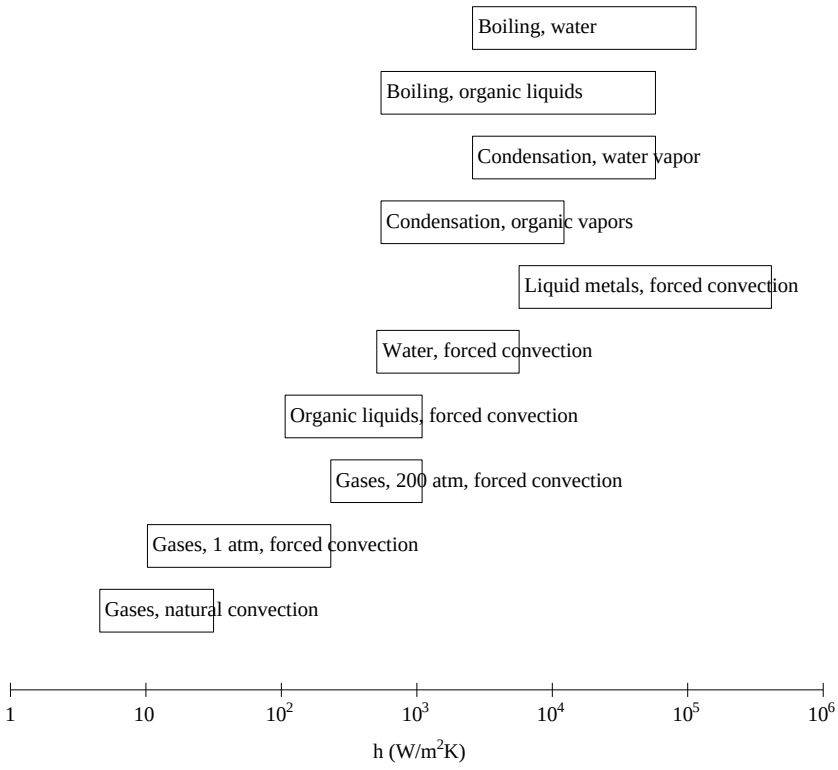

Figure 5.1. Heat transfer coefficient for different fluids and flow regimes (Bejan, 1993)

Given that natural convection was not expected to have a meaningful impact in water temperature and including it would have increased the complexity of the model, natural convection was not considered within the domain of the finite volume model. However, natural convection was considered as part of the boundary conditions, as will be described later in this chapter.

5.1.3. Radiation

Radiation is a heat transfer mechanism that requires no medium or direct contact between two bodies. Heat transfer occurs through electromagnetic waves, warmer surface

emanates heat into colder surfaces (Bejan, 1993). An ideal radiator or black body emits energy E_b according to:

$$E_b = \epsilon\sigma T_b^4 \tag{5.7}$$

Equation 5.6 suggests that E_b is proportional to the body temperature T_b taken to the fourth power, and the proportionality constant σ is known as Stefan-Boltzmann constant, which has a value of 5.67×10^{-8} W/m^{2}K^4. However, the intensity of radiation emitted by a real surface (gray surface) is only a fraction of the radiation emitted by a black body. Thus, Equation 5.6 is multiplied by emissivity ϵ, a unitless coefficient between 0 and 1 that for a given surface, represents the fraction of radiation relative to a black body. As a body emits radiation, it also absorbs radiation at a rate given by:

$$G_{abs} = \alpha\sigma T_b^4 \tag{5.8}$$

Moreover, if a body is assumed to be surrounded by a much larger body (Figure 5.2) and if absorptivity α is assumed to be equal to ϵ, then the net radiation heat flux on body A can be calculated using the following equation:

$$q_{rad} = \epsilon\sigma A(T_a^4 - T_{surr}^4) \tag{5.9}$$

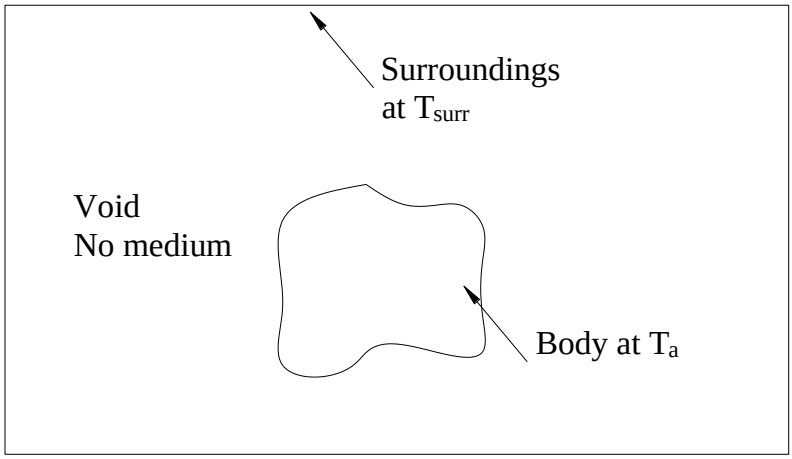

Figure 5.2. Solid body inside a void being irradiated by surroundings

Equation 5.9 is a very simplified approximation of radiative heat transfer that limits the system to two bodies, one surrounding the other one, exchanging heat through radiation. The net heat flux in body A, q_{rad}, is then the radiation that the body emits minus the radiation that is absorbed by the body.

5.2. Finite Volume Model

The equations presented in section 5.1 are a good approximation for simple 1-dimensional, steady state problems with a single body or a very simple geometry. However, solving the transient conduction equation analytically is impossible for the insulated isolation bearing problem posed here, given that fluids properties are not constant with respect to time, temperature and space. Also, in case of radiative heat transfer, several bodies radiate toward several surfaces, and Equation 5.9 is not sufficient to account for all

the radiative heat transfer in the system. Hence, a finite volume model was built using ANSYS Fluent 2020.

The geometry of the finite volume model includes the Robertson Bridge bearing and all elements in the load path (Figure 3.12a), up to and including part of the middle element of the A-frame. Given the symmetry of the set up, only a quarter of the bearing was modeled to reduce the number of elements, as shown in Figure 5.3.

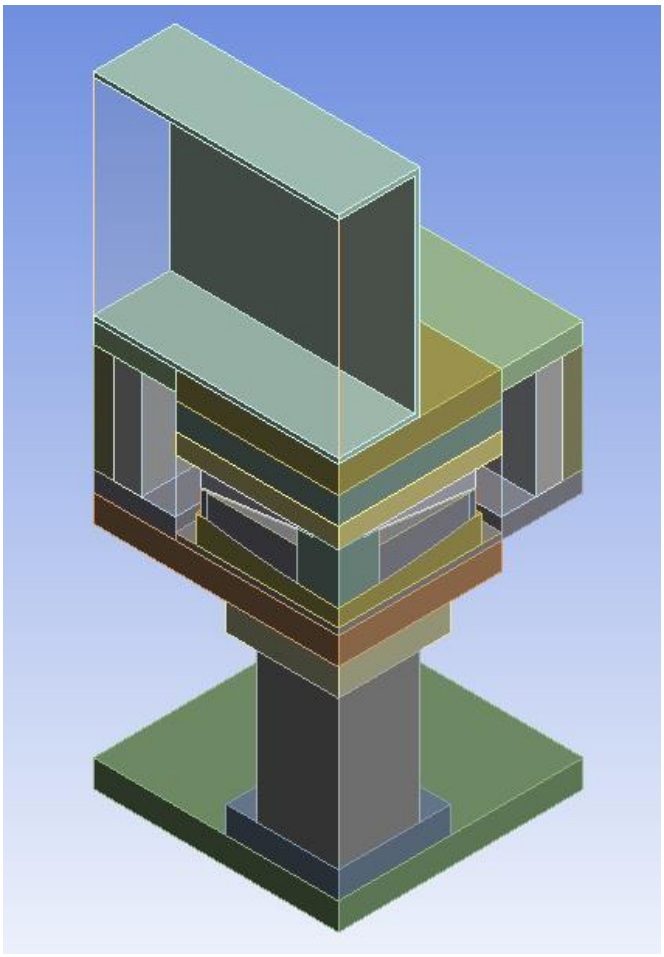

Figure 5.3. ANSYS Fluent model geometry

A symmetry boundary condition was assigned to the symmetry faces to account for the rest of the geometry. To reduce the number of elements and help the convergence of the solution, some elements with highly irregular shapes were represented with a more regular geometry (e.g. the bearing slider was modeled as a cylinder from the concave surface up to the bearing top plate). Also, to avoid convergence problems, geometry was slightly modified to avoid sharp corners. For example, a sharp air corner caused by the inner seal shown in red (Figure 5.4(a)), has been modified in the model geometry (Figure 5.4(b)).

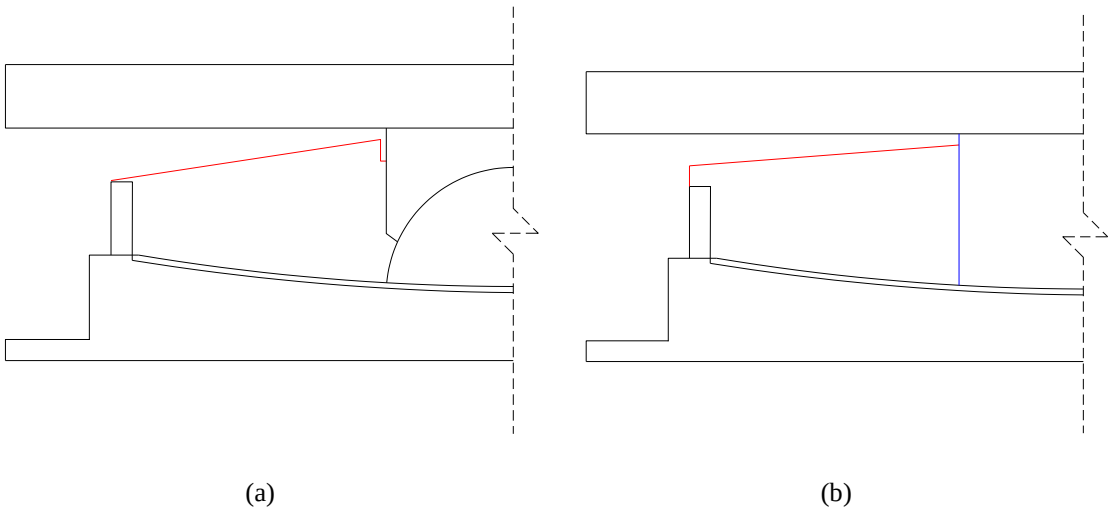

(a) (b)

Figure 5.4. Robertson bridge bearing inner seal and slider (a) Original geometry (b) Model modification

The domain of the model included all physical elements shown in Figure 5.3. The model domain boundaries were set to be consistent with the physical geometry, meaning that external air surrounding the bearing insulation box was not modeled. As will be described later in this chapter, dry ice was modeled using two different approaches and one of those approaches required the domain and boundaries to be slightly modified.

Within the model domain, conduction and radiation heat transfer mechanisms were applied. Natural convection was not expected to considerably affect the results given the limited fluid within the bearing insulation box. Also, convergence is harder to achieve when including natural convection in the model. As a result, natural convection was not included within the domain, but was considered when defining boundary conditions.

5.2.1. Material Properties

The material properties that were considered in the model were specific heat capacity, thermal conductivity, density and emissivity for radiation. The variation with temperature was not significant for solid materials, hence constant values were considered. Table 5.1 shows the properties of solid materials.

Table 5.1. Solid material properties

Material	Specific Heat (J/kg K)	Thermal conductivity (W/m K)	Density (kg/m^3)	Emissivity	Location
SS316	510	16.2	7990	0.35	Slider & Concave surface
ASTM A36	470	50	7850	0.35	Adapter plates
ASTM A536	490	36	7100	0.35	Bearing top and bot plates
ASTM A500 grC	450	36	7850	0.35	A-frame
EPDM	2000	0.2	1000	0.6	Bearing seal
Polyurethane	2000	0.026	30	0.6	Insulation box
Fiberglass	700	0.035	1440	0.6	Additional insulation
Dry Ice	1392	0.20	1000	0.97	Dry ice

In addition to the materials listed in Table 5.1, a modified ASTM A36 material was used to model the load cell, where the thermal conductivity was modified from 50 to 13 W/m K, to account for the hollow section of the load cell.

Water phase change was not modeled; however, variable water properties were applied in the finite volume model to account for the variation in properties, especially as it transforms between solid and liquid phase. Figures 5.5 and 5.6 show plots of specific heat and thermal conductivity, respectively. Since natural convection was not considered in the model, constant density was used.

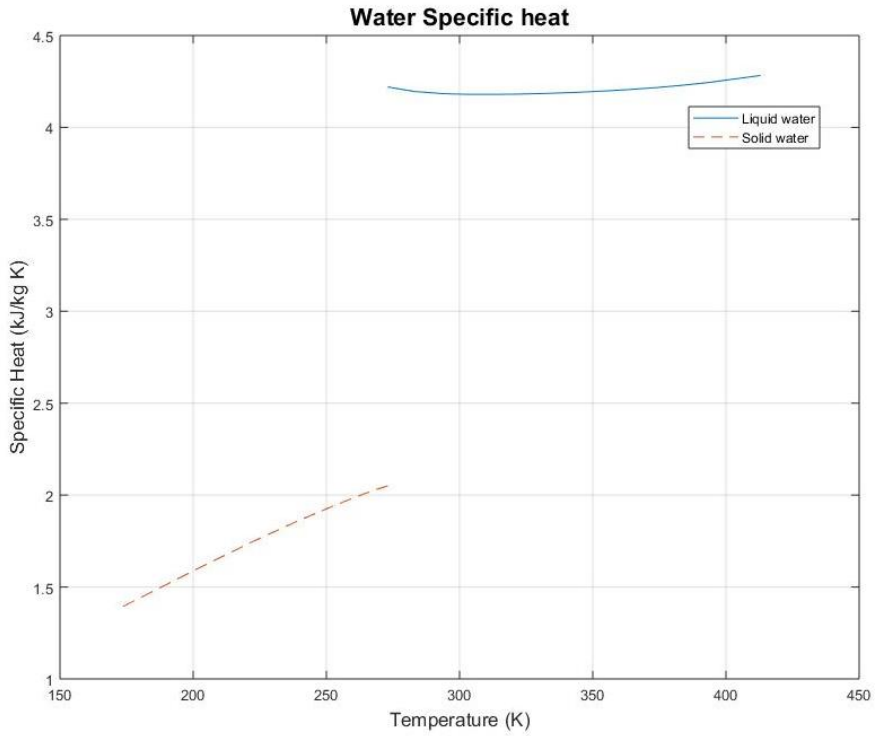

Figure 5.5. Water specific heat as a function of temperature (Engineering Toolbox, 2018)

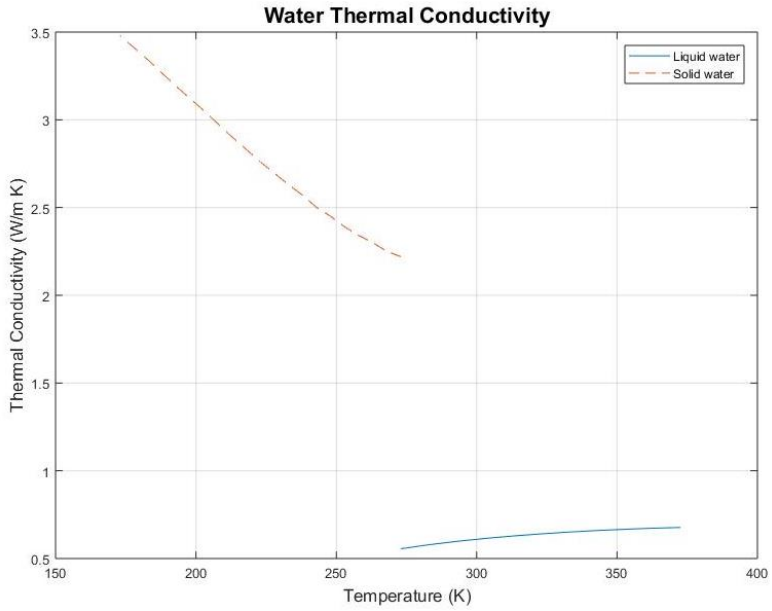

Figure 5.6. Water thermal conductivity as a function of temperature (Engineering Toolbox, 2004)

As with water properties, variable air properties were used as well. Figures 5.7 and 5.8 show plots of specific heat and thermal conductivity, respectively.

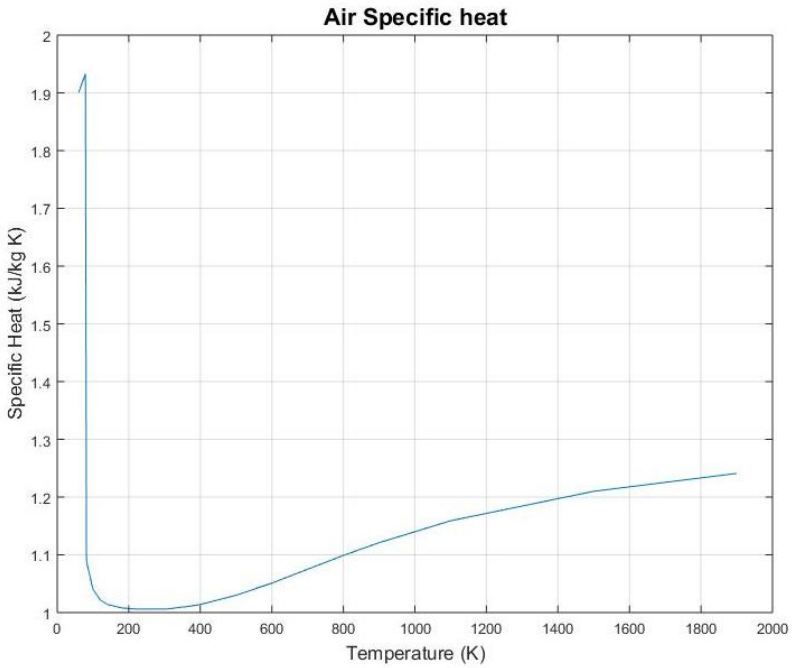

Figure 5.7. Air specific heat as a function of temperature (Engineering Toolbox, 2004)

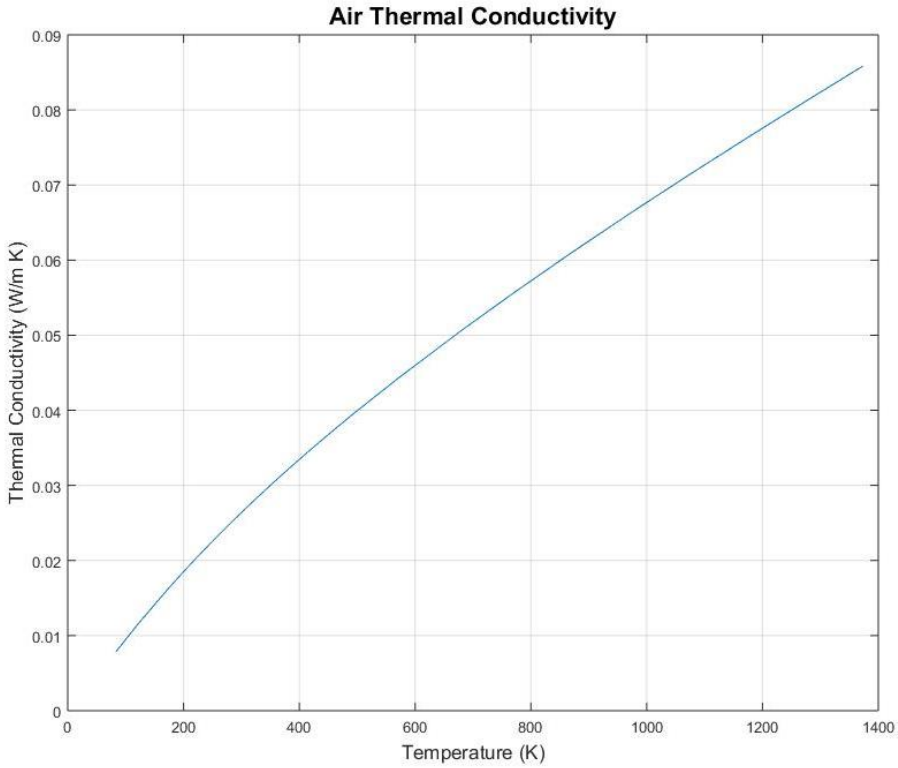

Figure 5.8. Air thermal conductivity as a function of temperature (Engineering Toolbox, 2009)

The functions shown in Figures 5.5 through 5.8 were implemented in ANSYS Fluent as a set of data points. The values are interpolated by ANSYS based on the temperature at each iteration.

5.2.2. Radiation Model

In the thermal finite volume analysis, conduction and radiation effects are evaluated by separate equations, and the total heat flux is the sum of the conductive and radiative heat flux. At each iteration, the conduction energy equation (Equation 5.4) is applied first,

which leads to a revised temperature estimate. This temperature is then used to compute the radiation heat flux.

As mentioned in section 5.1.3, Equation 5.9 is a very simplified approximation of the radiative heat transfer. In a more complex system, radiation is not absorbed or emitted by a single body, hence scattering of radiation across all bodies in the system needs to be considered. In addition, Equation 5.9 does not consider any variation in the radiation intensity, which depends on position and direction.

The model used to calculate radiative heat transfer was Discrete Ordinates (DO). In radiative heat transfer, any point in the domain receives radiation "beams" from an infinite number of directions. In the model, a finite number of radiation beams from different directions are aimed at a given point in the domain (ANSYS Inc, 2009). ANSYS Fluent discretizes the directions into octants (each one with an angle of 45 degrees), and each octant can be further discretized by the user. In this model, each octant direction was discretized into 3 segments, leading to 48 total beam directions. The following radiative transport equation is solved numerically.

$$\nabla \cdot (I(\vec{r},\vec{s})\vec{s}) + (a+\sigma_s)I(\vec{r},\vec{s}) = an^2\frac{\sigma T^4}{\pi} + \frac{\sigma_p}{4\pi}\int_0^{4\pi} I(\vec{r},\vec{s}^t)\Phi(\vec{r},\vec{s}^t)\,d\Omega' \qquad (5.10)$$

Equation 5.10 is in essence a radiative energy balance. The first term in Equation 5.10 is the rate at which the intensity of the beam $I(\vec{r},\vec{s})$, which is a function of position $\vec{r}$ and direction $\vec{s}$, changes in the direction $\vec{s}$. The second term is an "absorption and scattering" term that defines how much radiation is absorbed and scattered in the mesh

cells as the beam moves along, hence reducing the intensity of the beam. Absorption and scattering are determined by the absorption coefficient a and the scattering coefficient coefficient σ_s, respectively. The first term on the right hand side accounts for the radiation emitted by each cell of the mesh, which depends on the absorption coefficient and the refraction index n. As the beam moves along the intensity is increased by radiation emitted by different cells. The last term of Equation 5.10 accounts for scattering of different beams over the beam in the direction analyzed as determined by the phase function $\Phi(\vec{r}, \vec{s}^t)$. Since DO method discretizes the beam directions into a finite number of directions, the integral in the last term becomes a summation. Equation 5.10 is solved for all directions and for all cells that participate in radiation. Values of emissivity for materials in the model were included in Table 5.1, since n is a function of emissivity.

5.2.3. Boundary Conditions

Assigned boundary conditions (BC) are shown in Figure 5.9. Three different types of boundary conditions were applied. Symmetry boundary conditions are applied to surfaces along the lines of symmetry, and mirror the domain (including material properties, geometry, initial conditions and boundary conditions) with respect to the surface to which the symmetry boundary condition is assigned. For boundary condition assignment, the shake table was assumed to be a meter thick SS316 solid plate, with no air gaps inside and with air flowing below it. Hence, a convection boundary condition was assigned to the surface of the bottom plate in contact with the shake table. The convective heat transfer coefficient *h* for the bottom boundary was calculated using the following equation:

$$h = \frac{k}{L} \tag{5.11}$$

where L, the height of the shake table, was assumed to be 1 meter and thermal conductivity k was assumed to be 16 W/m^{2}K, a common value for steel. The shake table was assumed to be solid, without any air spaces inside.

Mixed boundary conditions, which assume convection, conduction, and radiation are all taking place at the boundary, were assigend to the rest of the external boundaries in contact with outside air. In Figure 5.9, the zones highlighted in green are the surfaces with mixed boundary conditions, and the zones highlighted in red are zones with symmetry boundary condition.

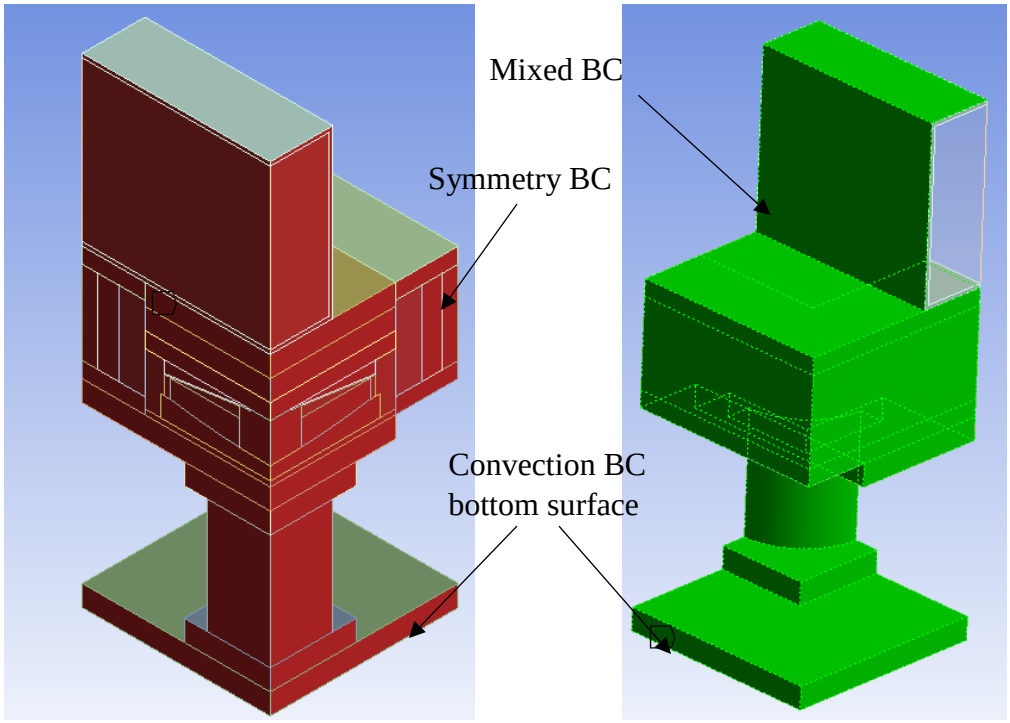

Figure 5.9. Boundary conditions: (a) Symmetry and (b) Mixed

The values for heat transfer coefficient and radiation temperature for the different types of boundary conditions are shown in Table 5.2. No heat transfer was considered in the surfaces of the A-frame connected to the rest of the A-frame, hence a mixed boundary condition with heat transfer coefficient of 0 W/m^2K was considered.

Table 5.2. Boundary condition parameters

Boundary Condition	Heat transfer coefficient (W/m^2 K)	Radiation Temperature (°K)
Mixed	3	293
Convection	16	-

5.2.4. Dry Ice Modelling

The process though which CO_2 (dry ice) changes phase directly from solid to gas is called sublimation. Cooling is achieved as dry ice absorbs energy from the system in order to sublimate. Dry ice sublimation was not directly modeled to optimize the modeling effort and avoid the advanced programming required within ANSYS Fluent. Hence, two approaches to model cooling with dry ice were implemented. In Approach 1, the dry ice is treated as an energy source with a fixed negative value that cools down the system by drawing energy from it. This approach is valid if the source term is accurate. However, selecting the source term value is challenging due to uncertainties in dry ice sublimation, contributed by the surrounding temperature, amount of dry ice and insulation arrangement. For approach 2, the surfaces in contact with dry ice are considered to be fixed at the dry

ice sublimation temperature. This approach is valid if dry ice is continually in contact with the surfaces, which is accurate as long as the dry ice is replaced as it is consumed.

5.2.4.1. Approach 1: Source Term

As described before, for this approach the dry ice was considered as a negative energy source since it is absorbing energy from the system. The dry ice was modeled as a solid with the properties listed in Table 5.1. The following equation was used to calculate the rate at which the dry ice zone absorbs energy from the system:

$$E = \frac{W S_r h_s}{V} \tag{5.12}$$

Values for each parameter in Equation 5.12 are listed in Table 5.3

Table 5.3. Dry ice properties

Weight (W)	89.002	kg
Sublimation rate (S_r)	2.0%	(%weight)/hour
Heat of sublimation (h_s)	571	kJ/kg
Volume (V)	0.089	m^3

Given that dry ice sublimates continuously, hence reducing it's weight, the value of *E* was averaged over 12 hours resulting in approximately -2800 W/m^3.

5.2.4.2. Approach 2: Temperature Boundary Condition

For the second approach, dry ice was not modeled as part of the geometry. Instead, the dry ice was removed from the domain, and new domain boundaries were generated on the surfaces that were previously with the dry ice solid. Figure 5.10 shows the new model geometry after removing dry ice zone from the domain. Since dry ice sublimates continuously, surfaces in contact with dry ice should be close to the sublimation temperature (-109.7 °F or 194.5 °K). These surfaces – red lines in Figure 5.10 - were fixed to the sublimation temperature by assigning a temperature boundary condition. Since the dry ice does not fill the insulation box completely, a mixed boundary condition (parameters as shown in Table 5.2) was assigned along yellow lines and a "no heat transfer" boundary condition was assigned along green lines. This approach also assumes the dry ice is replaced continuously as it is consumed.

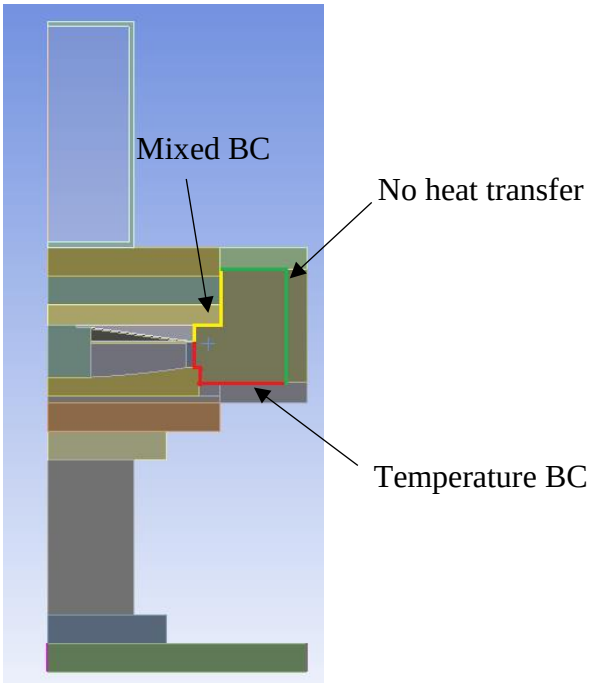

Figure 5.10. Approach 2 boundary conditions

5.2.5. Model Trials

The model was executed a total of 19 times, with different variations of initial temperature, dry ice modelling and boundary conditions. The model was set to simulate 24 hours of cooling, which is the upper bound cooling time that could be permitted. The target temperature of the ice was -30°F; the simulation was expected to estimate if and how quickly the target temperature could be reached, but also to track the evolution of temperature over the 24 hour time frame. The insulation box material was conservatively assumed to be fiberglass.

From the 19 trials, the first 12 were useful to identify boundary conditions that were significant, effects of varying initial temperature in water and steel elements. This presentation will focus on results from the 7 last trials with significant variations. Table 5.4 shows the variations in these trials. “Dry ice modeling” (column 2 in Table 5.4) lists the dry ice modeling approach used. When Temperature BC approach (CT) is applied, “Dry ice” (column 3) lists the assumed temperature at the boundary in K. The last column in Table 5.4 list any change in insulation arrangement made for each trial. These variations were considered to compare both approaches to model dry ice, analyze the time it takes to reach target temperature using different surface temperatures for dry ice approach 2 modeling and to assess the influence of insulation layer on top and below the bearings.

Table 5.4. Variations in analysis trials

Trial	Dry ice modelling	Boundary Conditions	Other conditions
		Dry ice	
13	ST=-2800	N/A	An extra layer of insulation surrounding the load cell and adapter plates
14	ST=-2800	N/A	Additional rubber layers on top and bottom of the bearing
15	CT	T-194	Additional rubber layers on top and bottom of the bearing
16	CT	T-194	No additional insulation other than the insulation box
17	CT	T-203	No additional insulation other than the insulation box
18	CT	T-213	No additional insulation other than the insulation box
19	CT	T-233	No additional insulation other than the insulation box

Nomenclature:

ST = Source Term approach
CT = Temperature BC approach
M = Mixed boundary condition
C = Convection boundary condition
T = Temperature boundary condition

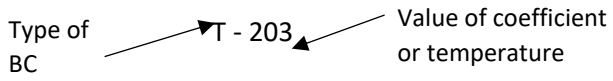

5.3. Finite Volume Model Predictions

5.3.1. Dry Ice Modeling Approaches

As listed in Table 5.4, trials 14 and 15 correspond to trials using Source Term approach and Temperature BC approach to model dry ice, respectively, with all other variables identical. Plots of average water temperature using both approaches are shown in Figure 5.11. The predictions by the two modeling approaches are very different from each other. In Source Term approach, water temperature initially increases slightly, due to the difference in temperature between the water and the rest of the elements in the model. Then, after 2 hours, it begins decreasing linearly, and reaches about 25°F after 24 hours,

which is much higher than target temperature -30°F. On the other hand, when modeling dry ice using Temperature BC approach, the temperature decreases rapidly during the first 3 hours to about -90°F, and then an asymptotic behavior is observed until the end of the simulation at 24 hours. In contrast with Source Term approach, in Temperature BC approach, the target temperature of -30°F was reached in less than an hour.

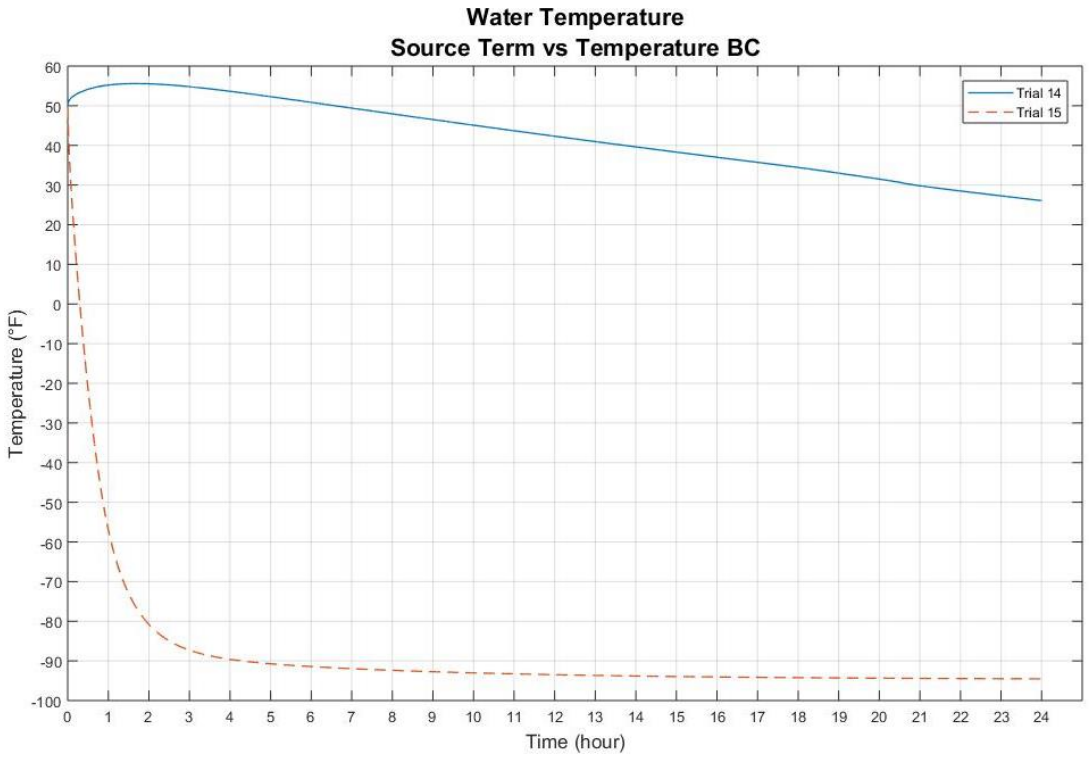

Figure 5.11. Water average temperature for Trial 14: Source Term vs Trial 15: Temperature BC

For the Source Term approach the dry ice – modeled as a solid within the domain – is part of the thermal mass, and the energy is drawn from the dry ice in addition to other parts of the model domain. As a consequence, the temperature of the dry ice mass is not properly maintained. Figure 5.12 shows the temperature contours on the model domain after 24 hours for Source Term (trial 14). The pink lines in Figure 5.12 show that at the

boundaries of the dry ice zone, the temperature is up to 40 degrees higher than the sublimation temperature. Since dry ice is continuously sublimating, any surface in direct contact with dry ice should be close to sublimation temperature (-109.5 °F or 194°K). Hence, in addition to the extra thermal mass considered in Source Term approach, it can be concluded that Source Term approach is conservative due to the relatively high temperature of the surfaces in contact with dry ice.

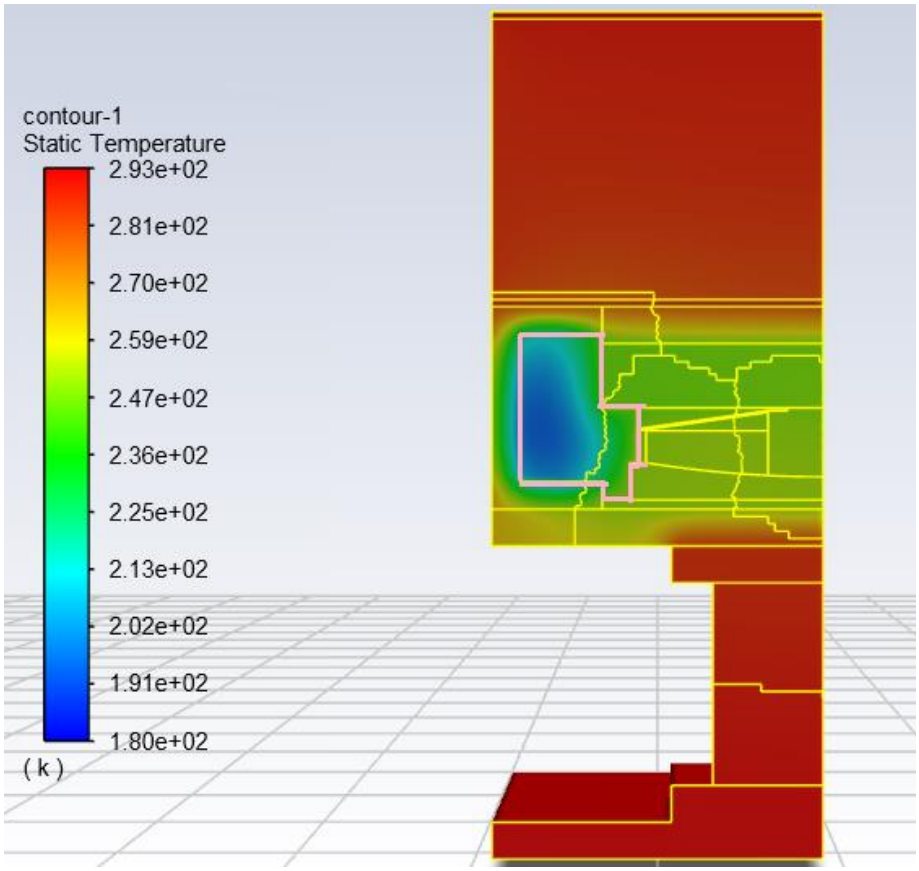

Figure 5.12. Trial 14 temperature contour at t = 24 hours

Ideally, with perfect insulation, Temperature BC dry ice modeling approach is believed to be closer to reality than Source Term approach, since it directly models the expectation that surfaces in contact with dry ice should be very close to sublimation

temperature. However, small gaps in the insulation arrangement and dry ice sublimation are expected, and the box cannot be continuously filled with dry ice. Hence, Temperature BC approach is expected to be a little unconservative.

5.3.2. Insulation Above and Below the Bearings

It is desirable to isolate the components that need to be chilled from those that do no. Hence, the effect of different insulation arrangements is studied next. Since Temperature BC indirectly assumes good insulation around the bearing, Source Term is more useful to identify potential variations due to different insulation arrangements. In trial 13, insulation around the load cell and adapter plates was applied in addition to the insulation box. In trial 14, in addition to the insulation box, a layer of insulation was applied directly on top and below the bearing, which can be applied physically between the bearing and the adapter plates by modifying the setup in Figure 3.12. Both trials used the Source Term approach. Figure 5.13 shows plots of average water temperature for trials 13 and 14. As expected, water temperature decreases faster with extra insulation on top and below the bearing (trial 14); however, in both cases temperature is decreasing linearly.

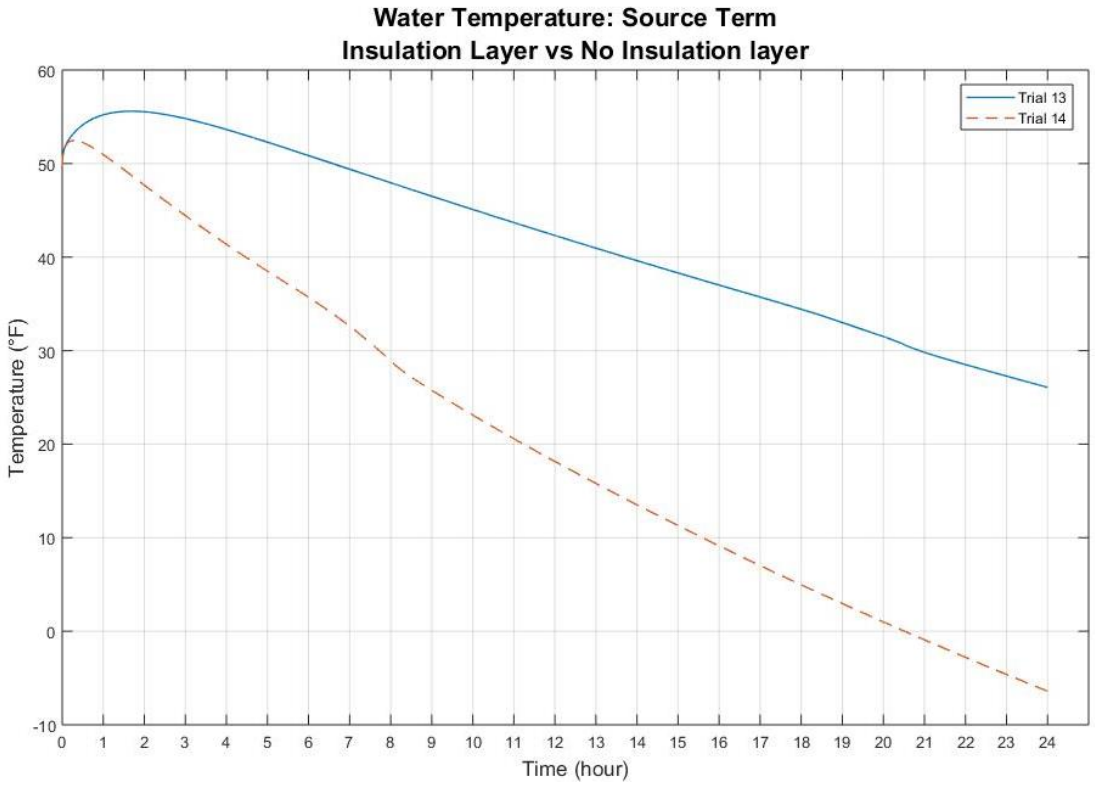

Figure 5.13. Water average temperature for Source Term approach: Insulation on top and bottom of bearing (trial 14) and Insulation around load cell (trial 13)

Trials 15 and 16 used the temperature BC approach, wherein extra insulation on top and bottom was considered in trial 15, and for trial 16 only the insulation box was considered. As shown in Figure 5.14, the effect of the extra insulation layers on the average water temperature is predicted to be negligible when the temperature BC approach is used. For a better measure of the effect of insulation, the heat transfer rate in the insulation layer for trial 15 (-49.38 W) was compared to the heat transfer rate in the steel plate for trial 16 (-114.92 W). These values confirm the benefit of adding the extra insulation layer since the heat transfer rate without the extra insulation layers on top and bottom of the bearing in trial 16 is almost twice as with insulation layers in trial 15; hence, incorporating extra insulation is expected to consume less dry ice over time. This effect can also be appreciated

in Figure 5.15, which shows the temperature contours at 24 hours for trials 15 and 16. In trial 16, the cooling extends to all components of the setup, while in trial 15 the cooling is confined to the bearing inside the insulation box and additional insulation layers.

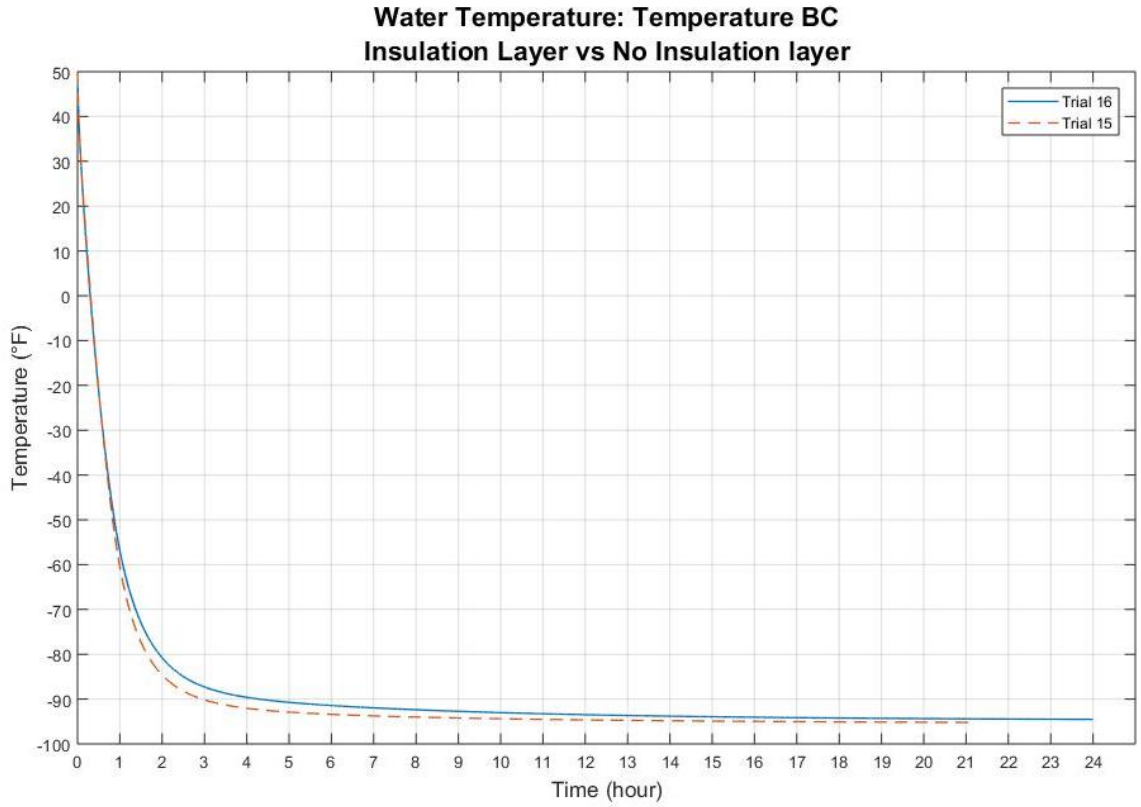

Figure 5.14. Average water average vs time with Temperature BC approach for Trial 15 (extra insulation) vs. Trial 16 (insulation box only)

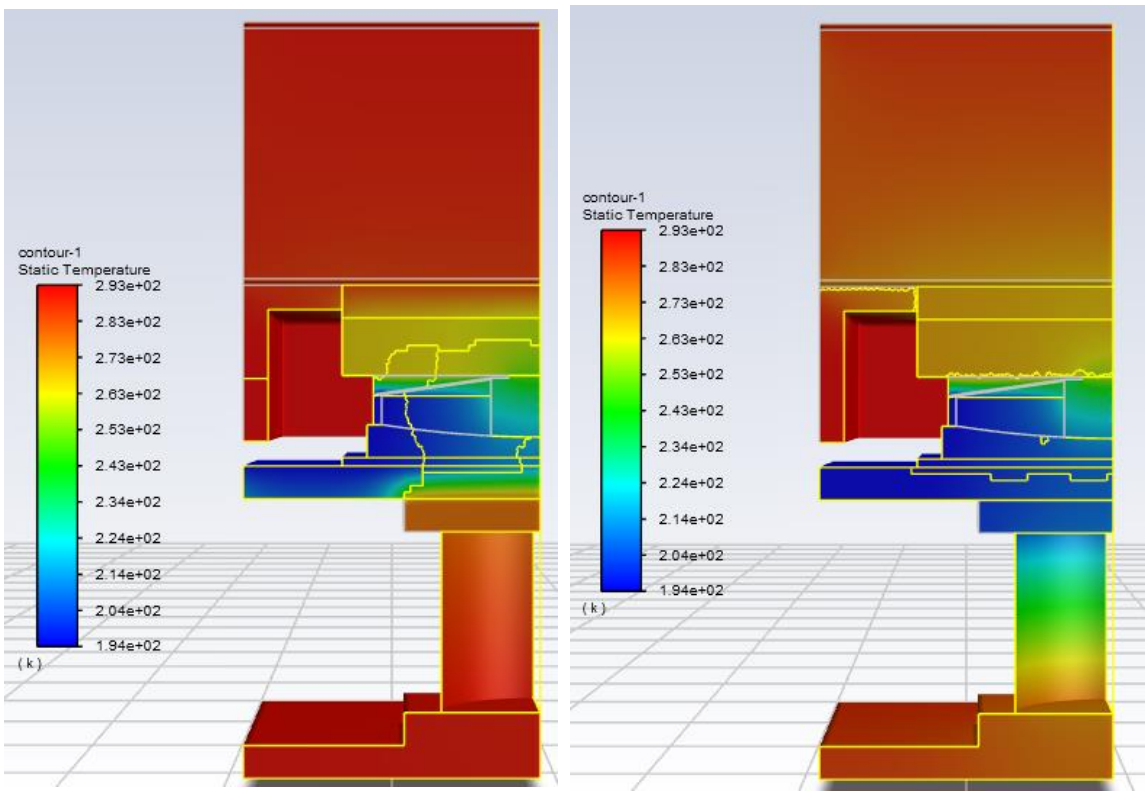

(a) (b)

Figure 5.15. Temperature contours at t=24 hours for (a) Trial 15 and (b) Trial 16

5.3.3. Effect of Surface Temperature

When using temperature BC approach to model dry ice, the exact temperature of surfaces in direct contact with dry ice is unknown but expected to be close to -109.5 °F (194 °K). However, due to the uncertainty, trials 16 to 19 varied the temperature of surfaces in contact with dry ice to assess the effect of surface temperature on the time needed to reach a water temperature of -30°F. Figure 5.16 shows average water temperature versus time for different values of assumed surface temperature.

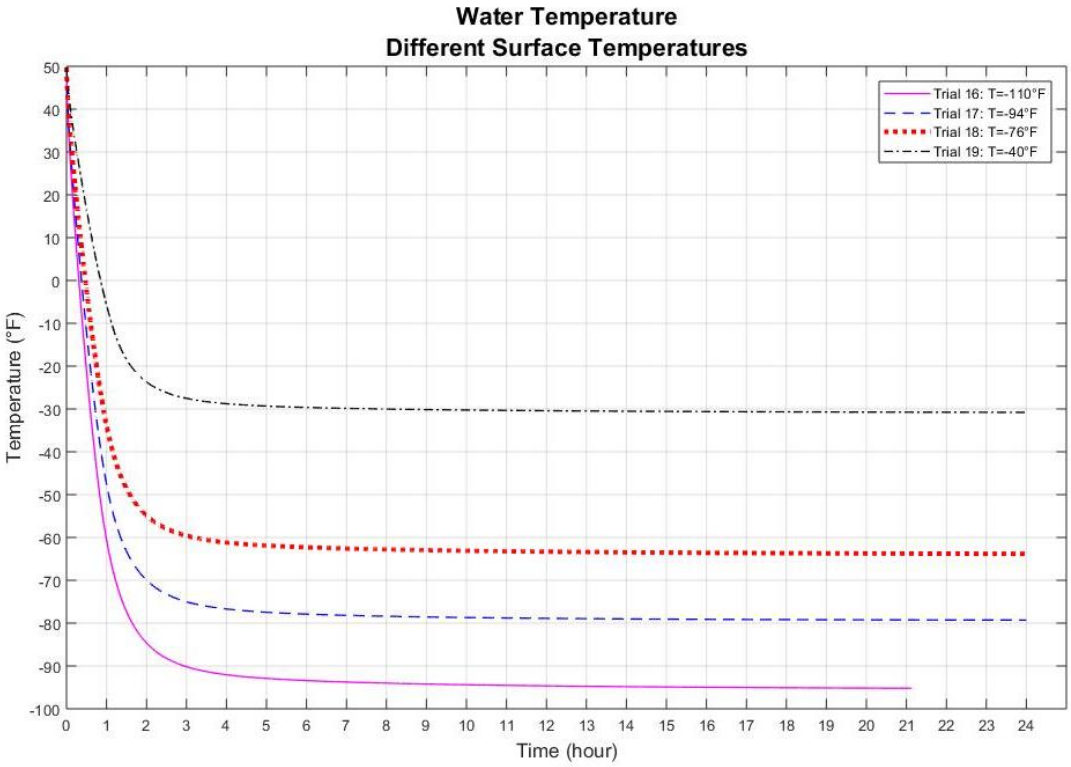

Figure 5.16. Average water temperature for trials 16, 17, 18 and 19

For all trials, an asymptotic behavior was observed wherein the temperature approached a constant, close to the assumed surface temperature, which was expected since the water temperature cannot go below the surface temperature. For all trials, the asymptotic behavior occurred after about 5 hours and water temperature was stable between 10 and 15°F higher than the trial surface temperature. In addition, about two thirds of the temperature drop occurred within the first hour. For trials with temperatures between -110 and -76°F, the time needed to reach -30°F is not significantly affected by the surface temperature, and varies from about 30 minutes at -110°F to 1 hour at -76°F. For trial 19 (surface temperature at -40°F), -30°F was the asymptotic temperature, and thus was reached after about 5 hours.

5.4. Freezing Test: First Trial

Given the uncertainty in variables such as dry ice sublimation rate, effectiveness of insulation arrangement and temperature of surfaces in direct contact with dry ice, a freezing test was conducted to validate the finite volume model predictions. The Robertson Bridge bearing was used for the freezing test, consistent with the finite volume model. An insulation box with similar geometry to the insulation box envisioned for the shake table tests was built. The bearing was placed within the box, filled with water, and surrounded by dry ice. Temperature was monitored in the water/ice zone and other bearing surfaces for 21 hours using a system of thermocouples, and periodic inspections were performed.

5.4.1. Insulation Box Geometry and Setup

The insulation box was built using 4 in thick sandwich insulation panels, meaning the insulation was sandwiched by a thin steel layer on each side. The external dimensions of the box were 41 in. x 36 in. x 17 in. As shown in Figure 5.17, polystyrene insulation blocks were used to reduce the volume of dry ice around the bearing.

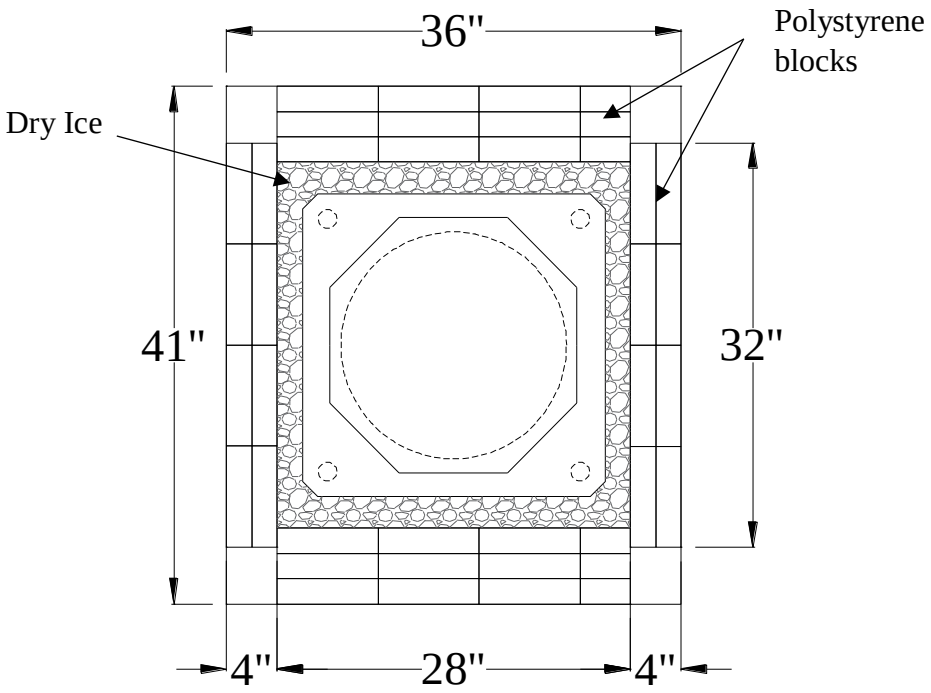

Figure 5.17. Insulation box plan view

To prepare the bearing, its exterior seal was removed and two holes were cut on the interior seal. The bearing was placed on top of a layer of insulation. A pre-calculated volume of water was inserted into the interior of the bearing through a tube extended through the interior hole. The bearing was filled with water up to the top of the ring, as shown in Figure 5.18.

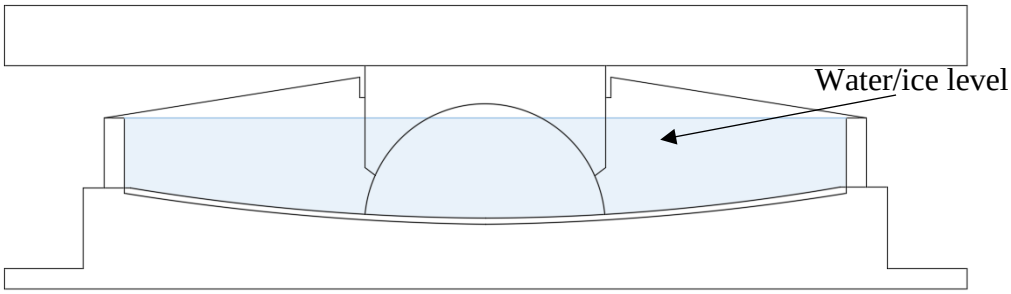

Figure 5.18. Water level inside the bearing

Next, the walls of the box were assembled around the bearing and after filling it with dry ice, a lid was placed on top. Gaps between adjacent walls were filled using polyurethane spray foam and fiberglass wrap insulation as much as possible. A total of 60 pounds of dry ice was poured inside the insulation box, distributed evenly around the bearing, as shown in Figure 5.19.

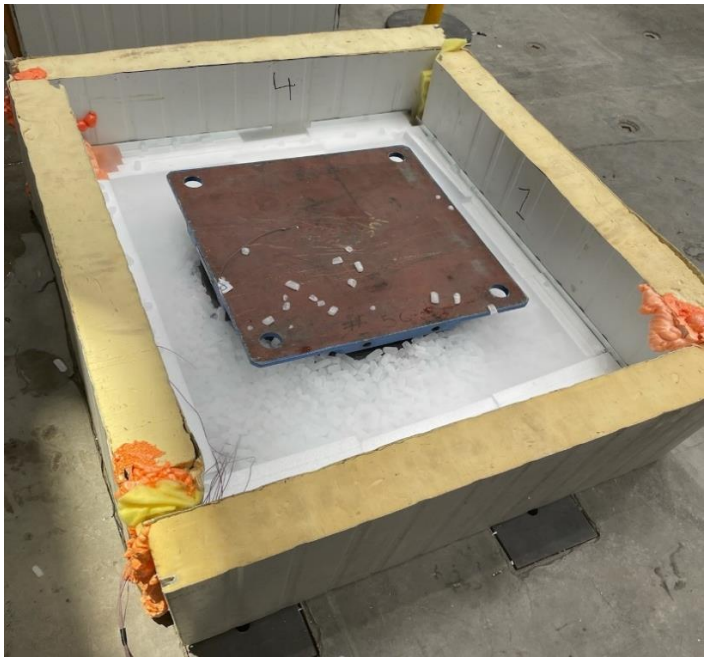

Figure 5.19. Insulation box filled with dry ice

5.4.2. Temperature Measurement System

To assess the temperature variation in and around the bearing, a total of 9 type "T" thermocouples were used to monitor temperature. From those 9 thermocouples, 7 were soldered on various bearing surfaces. The remaining 2 were placed inside the bearing to measure the water temperature, and were directed through holes cut on opposite sides of the inner seal. These thermocouples were not fixed to any surface and their exact location was unknown, but the ends were assumed to rest in the water/ice layer. The location of all thermocouples is shown in Figure 5.20 and listed in Table 5.5.

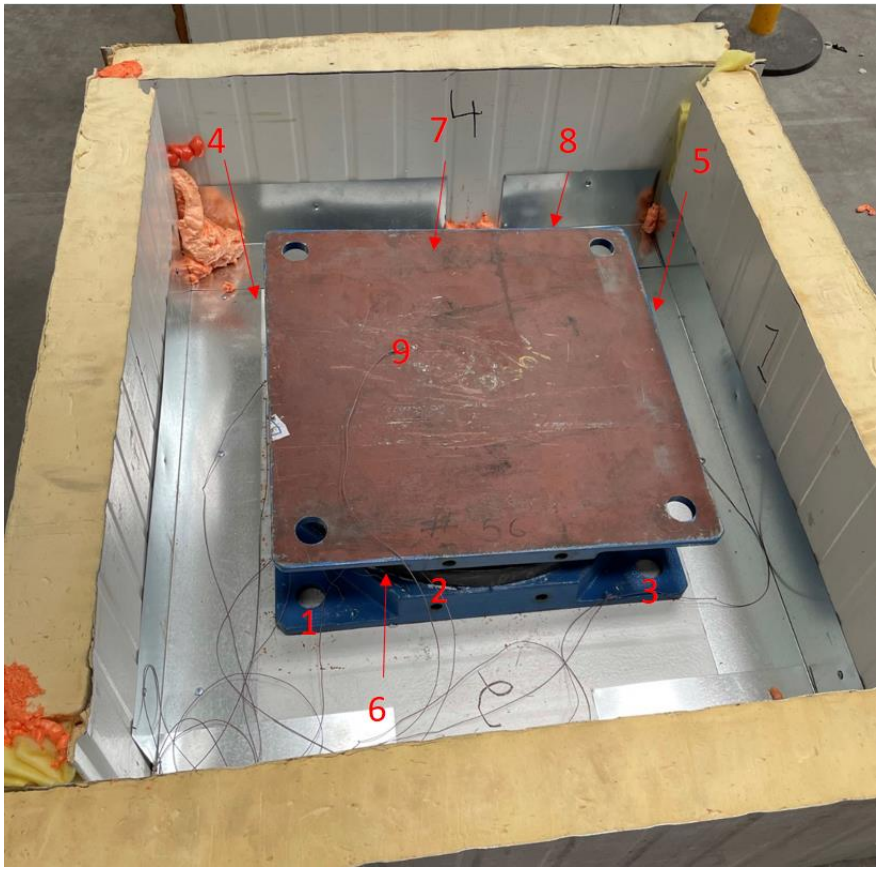

Figure 5.20. Thermocouples location

Table 5.5. Thermocouples legend

Thermocouple Location	Legend
1	Bottom Plate 1
2	Concave surf. Ext 1
3	Bottom Plate 2
4	Bottom Plate 3
5	Bottom Plate 4
6	Water 1
7	Water 2
8	Concave surf. Ext 2
9	Top Plate Ext

Temperature measurements were taken every 30 seconds starting right before filling the bearing was filled with water. Measurement data was parsed into the following time spans: (a) before filling the box with dry ice, (b) while filling the box with dry ice, (c) closed box filled with dry ice and (d) open box while defreezing. Temperature measurements started at 11:00 am and for time spans (a), (b) and (c), the last measurement was taken at approximately 12:00 am. For time span (d), temperature measurements started at 9:00 am, 9 hours after the last temperature measurement for time span (c); hence, there was a gap of 9 hours where no data was recorded.

5.4.3. Experimental Results and Finite Volume Model Comparison

Temperature measurements taken while the bearing was being filled with water were used to assess the initial temperature conditions and to evaluate if thermocouples were

working properly. Figure 5.21 shows temperature measurements while filling the bearing with water.

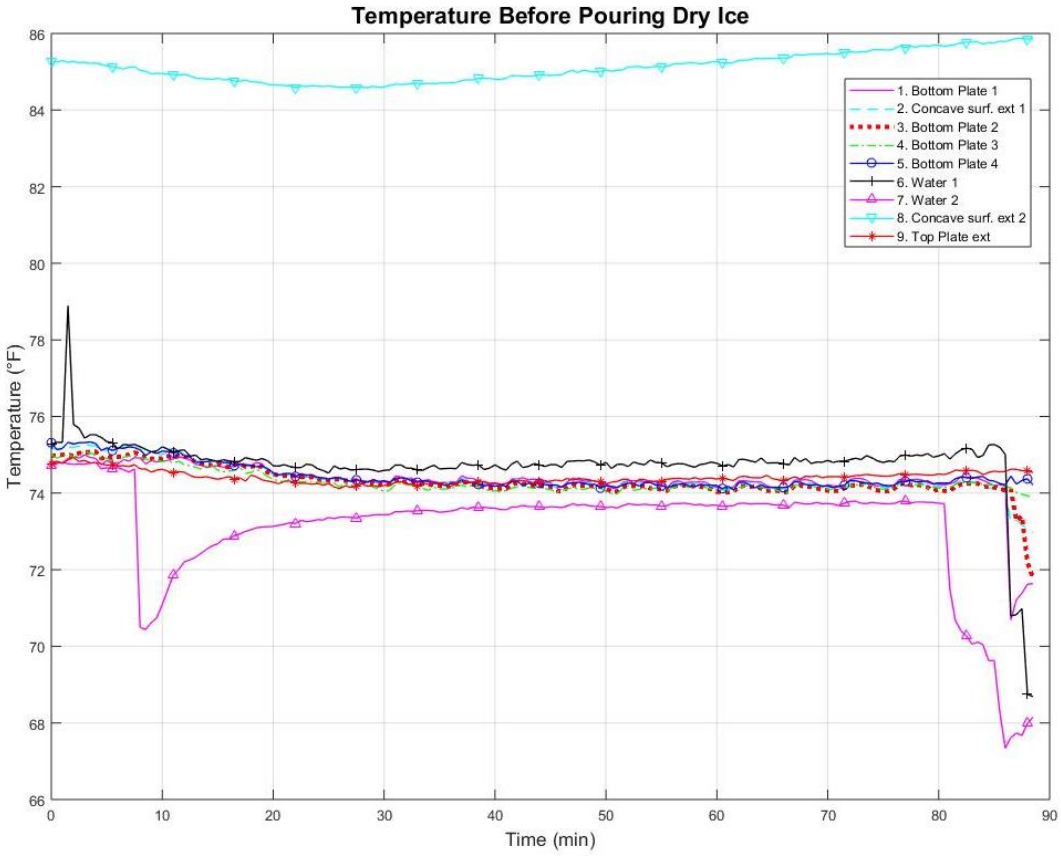

Figure 5.21. Temperature measurements while filling the bearing with water

The temperature initial conditions used in the finite volume model were 70°F or 293°K for all elements but water, which was set with an initial temperature of 50°F (283°K). However, sensor 7 shows a decrease in water temperature from 75°F (297°K) to 70.7°F (294.5°K) and after approximately 10 minutes it went up to 73.4°F (296°K). Sensors 6 and 7 show a minimum temperature of 68°F (293°K), which is higher than the assumed initial temperature for the finite volume model of 50°F (283°K). Since the thermocouples measuring water temperature (6 and 7) were floating, they may read

inconsistent temperature. Also, the reading from the thermocouple 8 was disregarded since the temperature readings in this thermocouple varied by 25% with respect to the rest of the thermocouples.

Temperature readings in Figure 5.22 correspond to the time span where the box was being filled with dry ice. As expected, water temperature remains constant while dry ice is being poured, due to the solids between dry ice and water (concave surface, bearing ring, plates, etc.). However, water was no longer increasing to room temperature. There was a rapid decrease in temperature around the bearing, but only thermocouples 2, 4 and 5 recorded temperatures approaching the sublimation temperature of dry ice. Thermocouples 3 and 1 recorded temperatures 30 to 40 degrees higher than sublimation temperature, which suggests that only some of the locations were in direct contact with dry ice. Gaps in between dry ice pellets may prevent all surfaces from reaching the sublimation temperature. Temperature BC approach to model dry ice is shown to be unconservative since a large variation in temperature within the surfaces in contact with dry ice was observed.

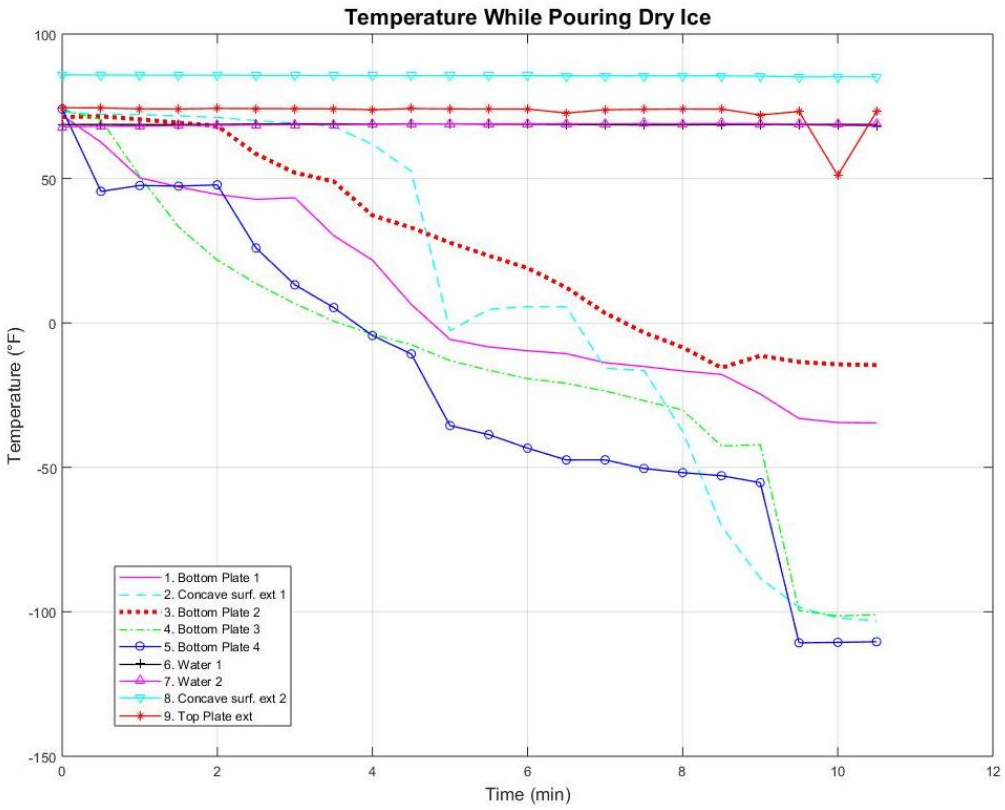

Figure 5.22. Temperature measurements while filling the box with dry ice

Figure 5.23 shows the temperature measurements after the box was filled with dry ice and the freezing process had begun. Readings in thermocouples 2, 4 and 5 suggested a dry ice sublimation rate, as temperature readings start to rise after 2-3 hours due to a drop in the level of dry ice in the container. Also, water reached the freezing point after approximately 2 hours and remained at that temperature for about 2.5 hours, during which the phase changed from liquid to solid. Afterwards, water temperature decreased to 5°F (258°K) after 7 more hours. Temperature on the bearing surfaces had also risen to about 5°F, suggesting all dry ice had sublimated, and the bearing temperature could not be lowered further.

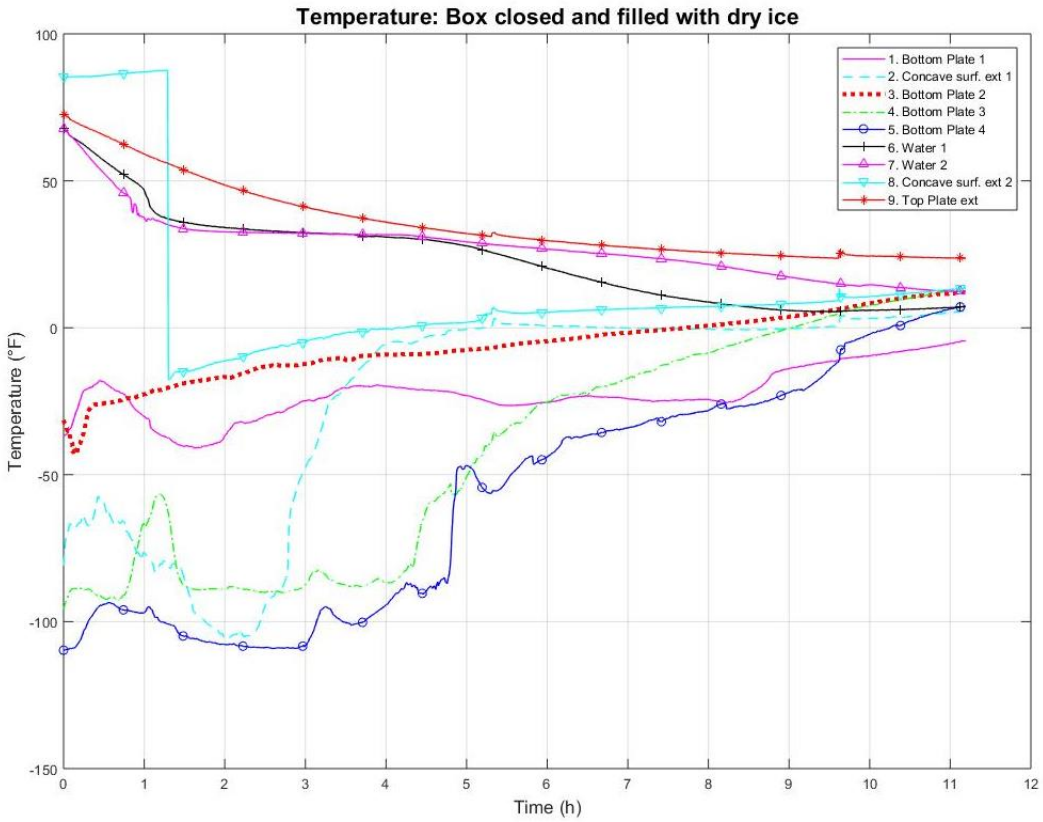

Figure 5.23. Temperature measurements during freezing process

The temperature was measured after the box was opened to determine how long the water will remain frozen. These temperature readings are shown in Figure 5.24. As mentioned earlier in this chapter, there was a 9 hour gap, where no temperature was recorded, which explains the abrupt temperature change from Figure 5.23 to Figure 5.24. Within the first hour, both thermocouples inside the bearing (6 and 7) still recorded temperatures below freezing point. After that, thermocouple 6 recorded temperatures above freezing point, while temperature recorded by thermocouple 7 was still below 0. This temperature difference suggests that part of the ice had already melted and some of it was still frozen.

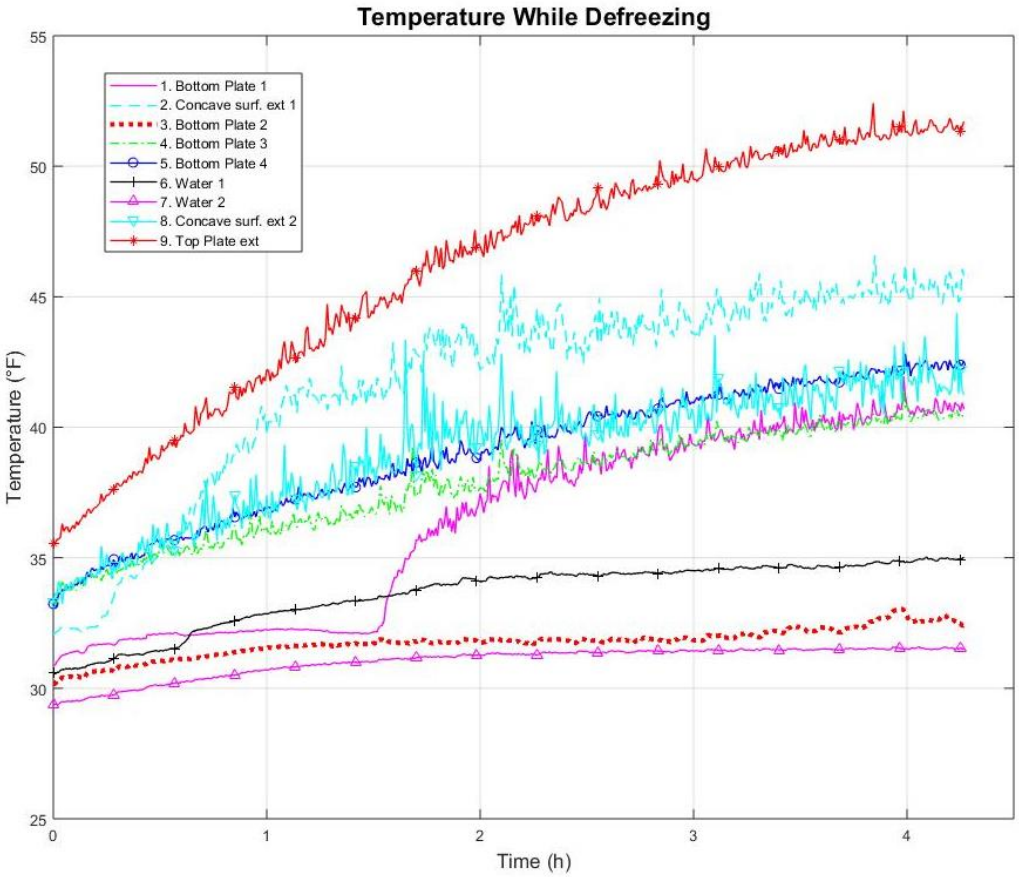

Figure 5.24. Temperature measurements after opening insulation box

Figure 5.25 compares finite volume model trials 14, 15 and readings from thermocouples 6 and 7 (thermocouples located inside the dry ice). Finite volume model trials 14 and 15 correspond to simulations with insulation layer on top and bottom of the bearing, for Source Term and Temperature BC dry ice modelling approaches, respectively. Since phase change was not considered in the finite volume model, the observed 2.5 hour phase transition (constant temperature) was not shown in the model prediction plots. Temperature readings from sensors 6 and 7 are between the two model predictions.

However, in the experimental test there was a 5 inch air gap on top of the bearing, which was not considered in the model. As stated earlier in this chapter, natural convection was not considered in the model, but with a significant air gap the bearing was heated through natural convection. Also, some air gaps were observed in the insulation box, which probably enhanced the air flow in the insulation box, hence heating the system.

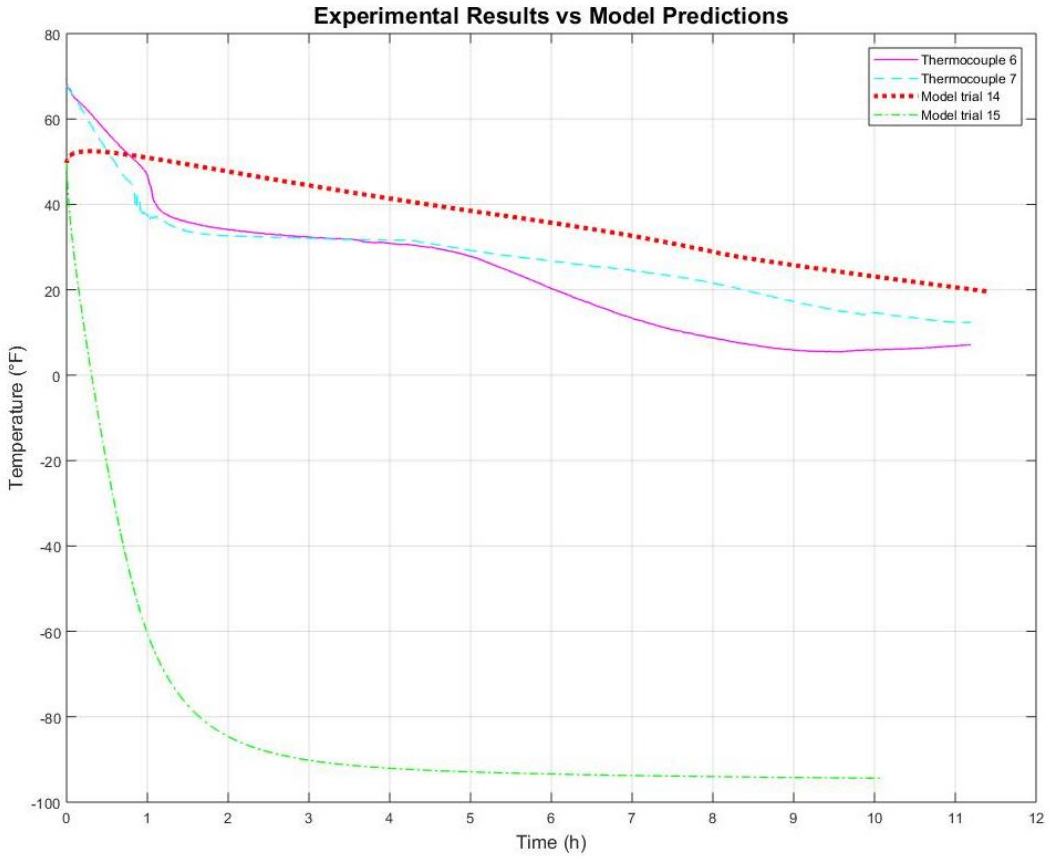

Figure 5.25. Comparison between experimental results and finite volume model predictions

5.4.4. Dry Ice Consumption

The insulation box and dry ice consumption was inspected after 6, 10 and 21 hours. The amount of dry ice at the beginning of the experiment is shown in Figure 5.26.

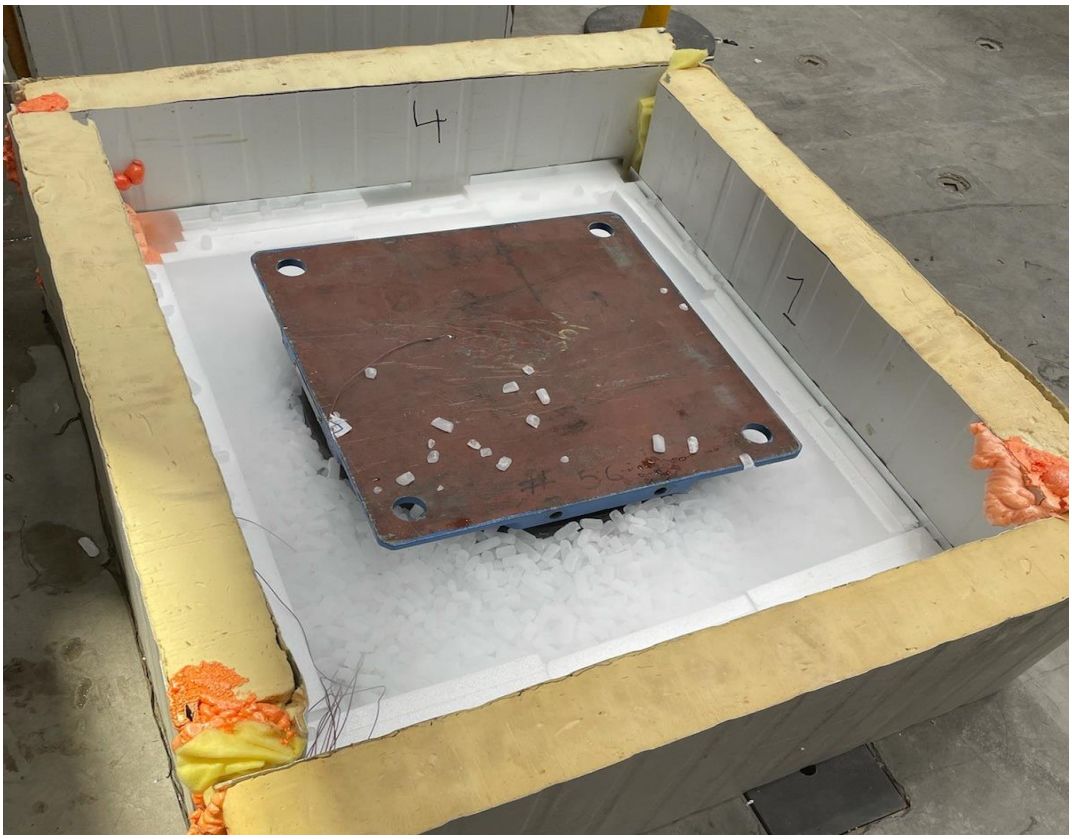

Figure 5.26. Dry ice in insulation box at the beginning of experiment

Figure 5.27 shows the insulation box after 6, 10 and 21 hours. After 6 hours (Figure 5.27a), it is estimated that only about 1/3 of the dry ice remained. After 10 hours (Figure 5.27b), it is estimated that only about 1/8 of the initial amount of dry ice remained. However, from 6 to 10 hours dry ice sublimated at a lower rate compared to the first 6 hours of experiment, likely because the water was already frozen and less energy was needed to decrease the temperature of water. The final inspection of the insulation box occurred after 21 hours. As shown in Figure 5.27c, the dry ice had completely sublimated. Hence, as a best case scenario, the sublimation rate in this test was 60 lbs per 21 hours, or approximately 3 lbs/h. The sublimation rate assumed before the test was 2% of dry ice

weight per hour, or a peak rate of 1.2 lbs/hour for 60 lbs. Hence, the observed rate was 238% higher than the one assumed in the finite volume model.

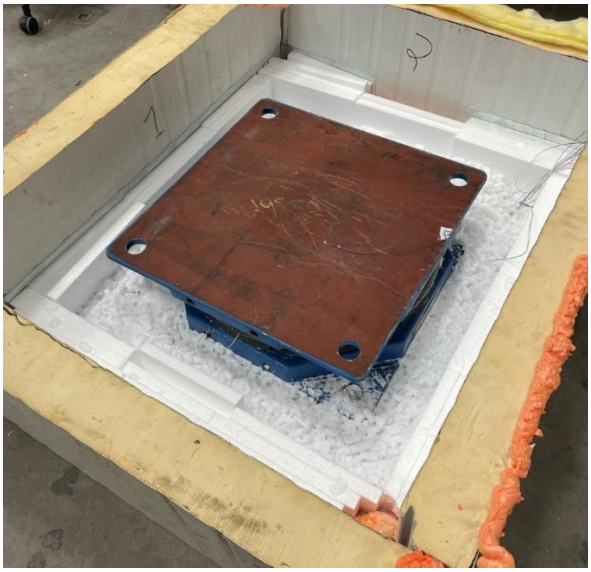

(a)

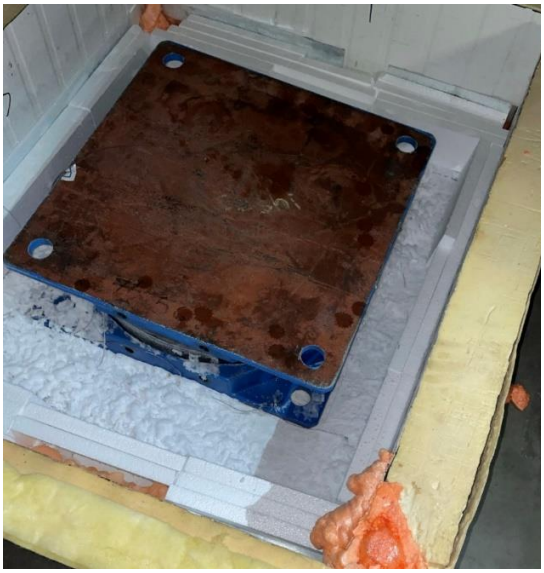

(b)

(c)

Figure 5.27. Amount of dry ice after (a) 6 hours, (b) 10 hours and (c) 21 hours

5.5. Freezing Test: Second Trial

In the first freezing test, the target temperature of -30°F was not reached. Hence, the set up and procedure was slightly modified for a second freezing test. The dry ice consumption in the first test was much higher than anticipated, so in the second test the dry ice was to be replenished after several hours.

5.5.1. Test Set up

The arrangement for the second test was very similar to that of the first test with the following differences: 1) the top piece of the box was reduced to fit within the box as shown in Figure 5.28a, hence reducing the air gap on top of the bearing, 2) additional polystyrene blocks were used to cover air gaps, and 3) the level of dry ice was raised to cover more of the bearing surface. Also, dry ice was sourced from a different location and the resulting product was formed in larger blocks instead of pellets, as shown in Figure 28b.

(a) (b)

Figure 5.28. Second freezing test set up: (a) Closed box and (b) Open box

The thermocouples were located in the same place as shown in section 5.4.2. However, two more thermocouples were added at the top of the outer ring, at opposite sides of the box, to monitor the dry ice level in the box through temperature changes in the sensors. The box was initially filled with 70 lbs of dry ice.

5.5.2. Experimental Results and Finite Volume Model Comparison

Temperature readings in Figure 5.29 correspond to the time span where the box was being filled with dry ice. Like the first test, water temperature remained constant while dry ice was being added, but at room temperature. The temperature on bearing sensors decreased at a lower rate than in the first test, and reached a low of -20°F, in contrast with -110°F from the first test. Thermocouples 10 and 4 recorded temperatures above freezing point, which suggests that there were bigger air gaps between dry ice cubes compared to the dry ice pellets used in the first test. Temperature BC approach to model dry ice is shown to be unconservative since none of the sensors recorded temperatures near sublimation temperature of dry ice.

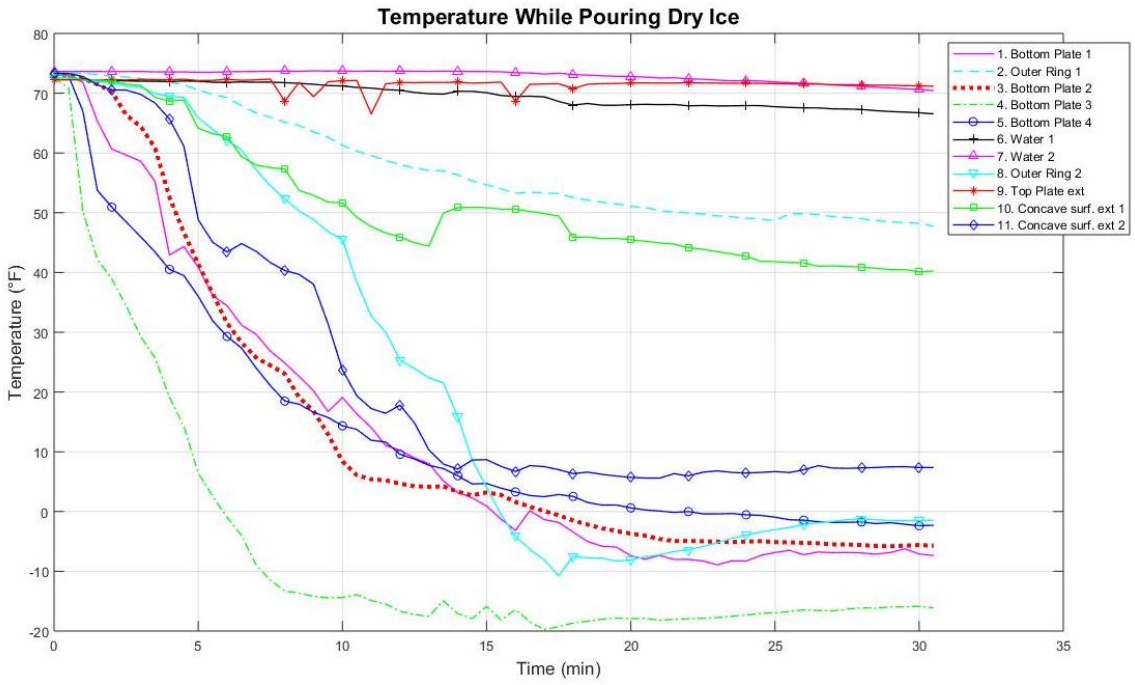

Figure 5.29. Temperature measurements while filling the box with dry ice

Figure 5.30 shows the temperature measurements during freezing. The minimum temperature of surfaces in contact with dry ice (sensors 1, 3, 4 and 5) was about -20°F. The freezing rate was lower than the first test and phase change took longer than in the first test, 5 hours in contrast with 2.5 hours. However, a sudden drop in temperature was observed at 6 hours, right after the box was refilled with dry ice. Subsequently, the water was able to reach a minimum temperature of -50°F, far lower than the water temperature in the first freezing test (-15°F).

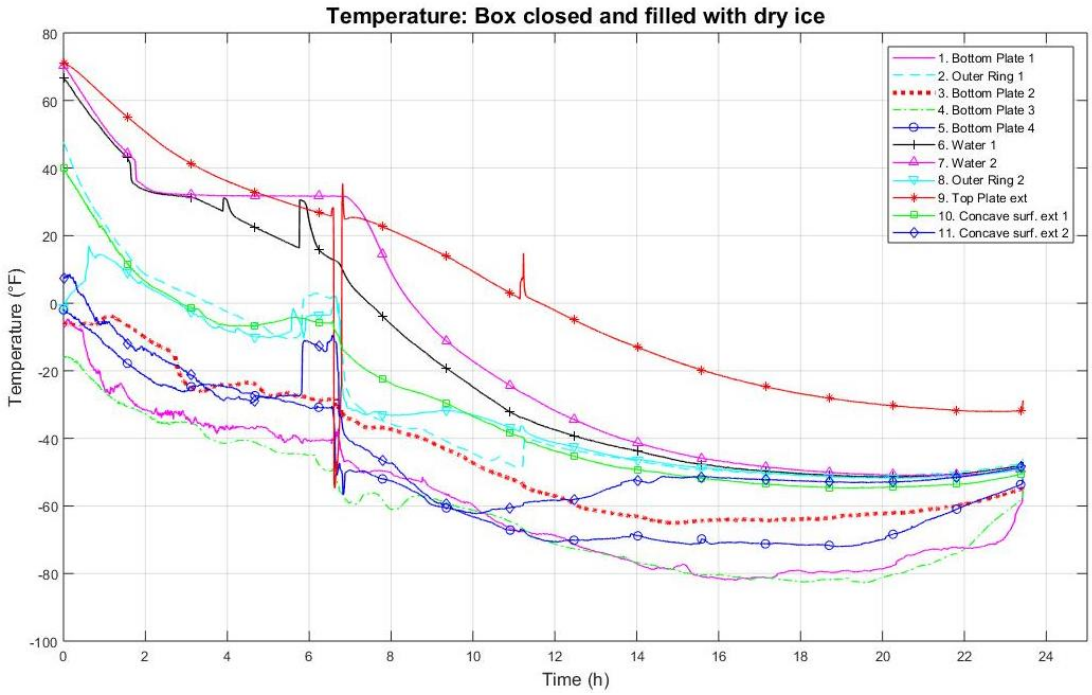

Figure 5.30. Temperature measurements during freezing process

The box was opened after 23 hours and Figure 5.31 shows temperatures taken with the box open. Measurements from sensors 6 and 7 show that water temperature remained below -30°F for 2.5 hours. The temperature readings of all sensors was very similar during defreezing, which suggests that all components warm up uniformly at the same heating rate.

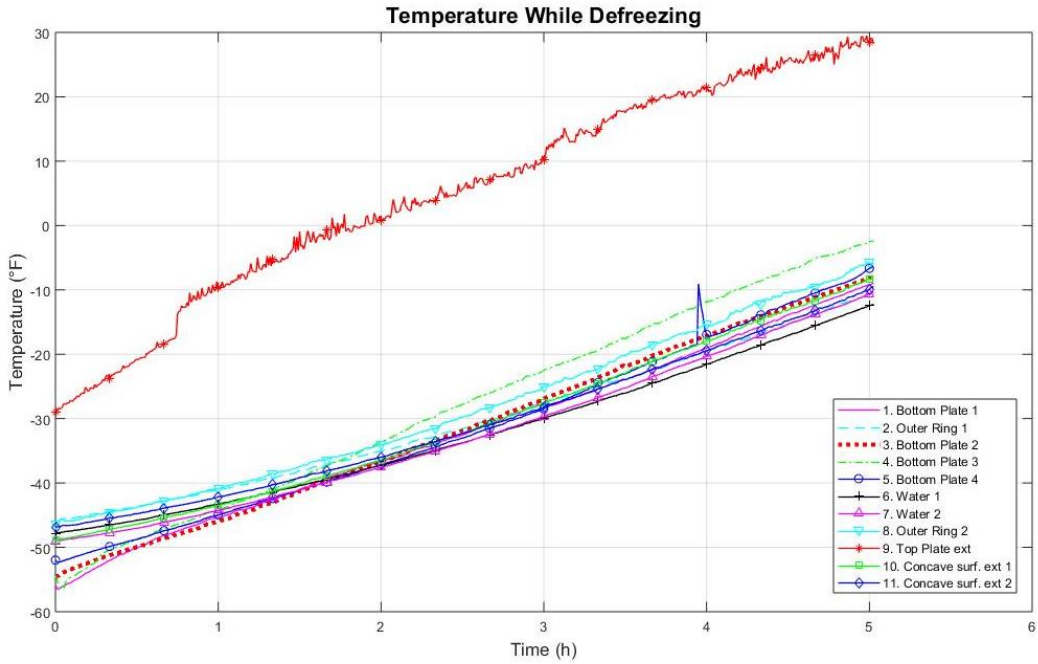

Figure 5.31. Temperature measurements after opening insulation box

Figure 5.32 compares finite volume model trials 14, 15 and readings from thermocouples 6 and 7 (thermocouples located inside the dry ice) for both freezing tests. Finite volume model trials 14 and 15 correspond to simulations with insulation layer on top and bottom of the bearing, for Source Term and Temperature BC dry ice modelling approaches, respectively. In both freezing tests, the phase change time where water registers a constant freezing temperature is apparent. Phase change is not considered in the model, hence modeling results do not show a time frame with constant freezing temperature. For both freezing tests, temperature readings from sensors 6 and 7 are between the predictions using both methods to model dry ice. However, the temperature path from the first test more closely resembles the Source Term approach. In contrast, the trajectory of the second test was closer to Temperature BC approach, but the final temperature after 24 hours was an average of the two model predictions.

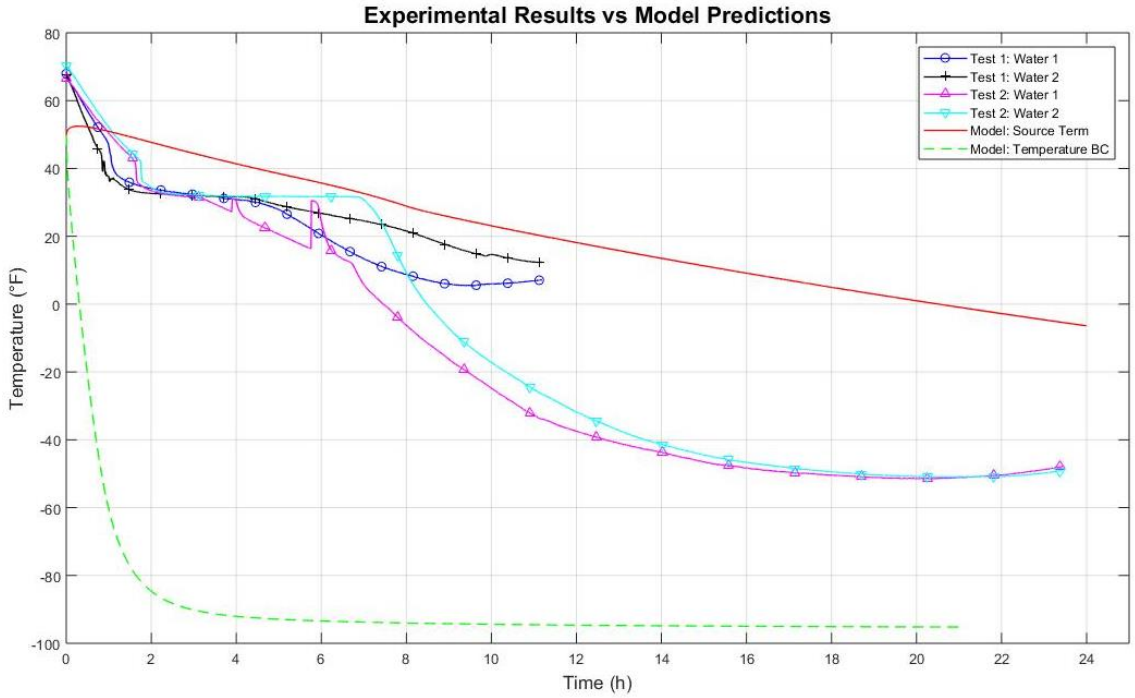

Figure 5.32. Comparison between experimental results and finite volume model predictions

Refilling the box with dry ice for second test improved the cooling of the system and made it possible to reach a lower temperature than in the first test.

5.5.3. Dry Ice Consumption

The insulation box and dry ice consumption was inspected after 6, 11 and 23 hours. The amount of dry ice at the beginning of the experiment is shown in Figure 5.33.

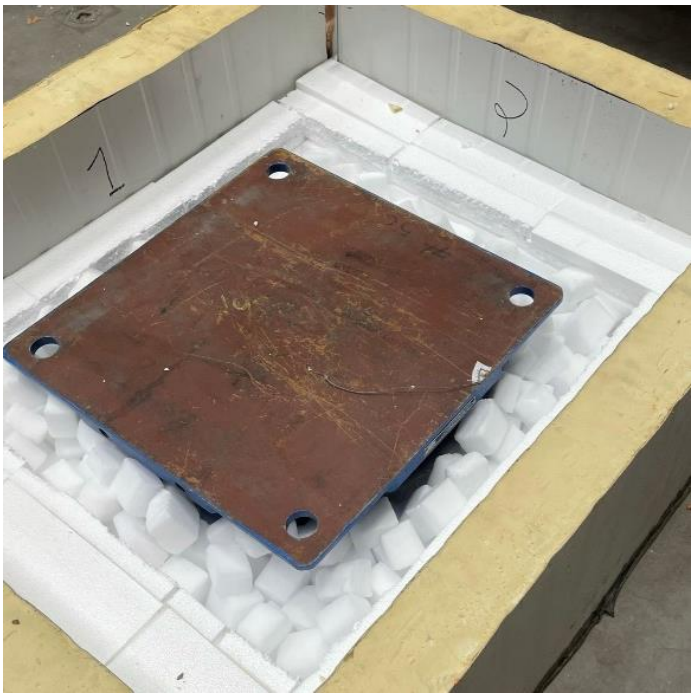

Figure 5.33. Dry ice in insulation box at the beginning of second experiment

Figure 5.34 shows the insulation box after 6, 11 and 23. The amount of dry ice was measured by inspection after 6, 11 and 23 hours into the experiment. After 6 hours (Figure 5.34a), about 1/2 of the dry ice remained and as mentioned before, the box was refilled to initial level. After 11 hours (Figure 5.34b), about 2/3 of the initial amount of dry ice remained, which suggests that dry ice was sublimating at a lower rate compared to the first 6 hours of experiment, which is in agreement with the findings of the first test. The final inspection of the insulation box occurred after 23 hours. As shown in Figure 5.34c, about 1/10 of the dry ice had not sublimated. Hence, the average sublimation rate before and during phase change was about 5.8 lb/hour, and about 3.7 lbs/hour after refilling. When compared with the sublimation rate assumed in the model, the sublimation rate observed in the second test was 308% higher.

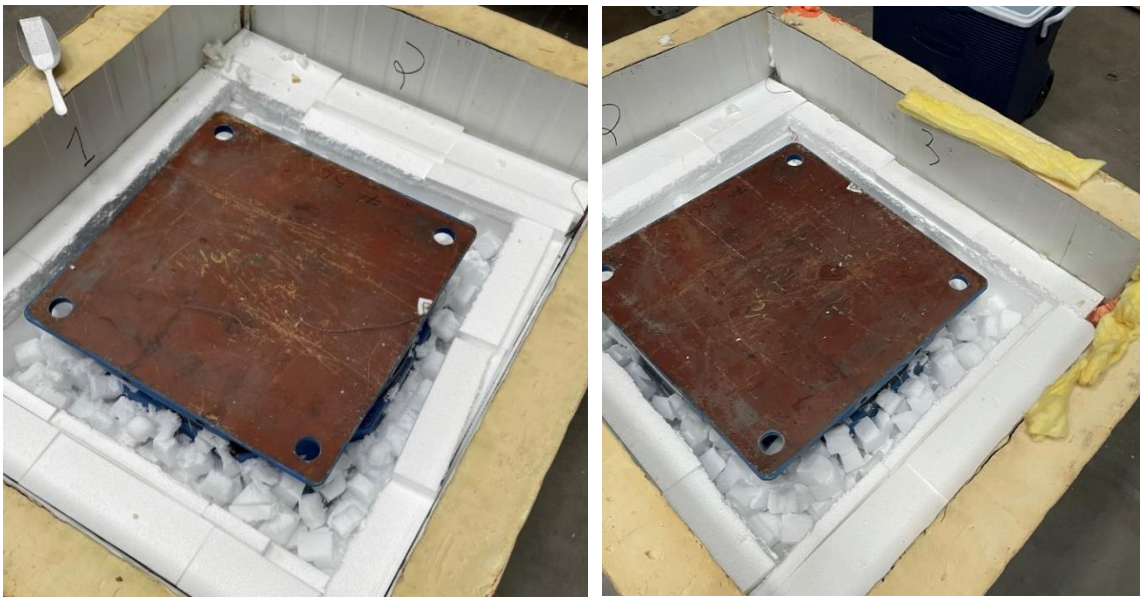

(a) (b)

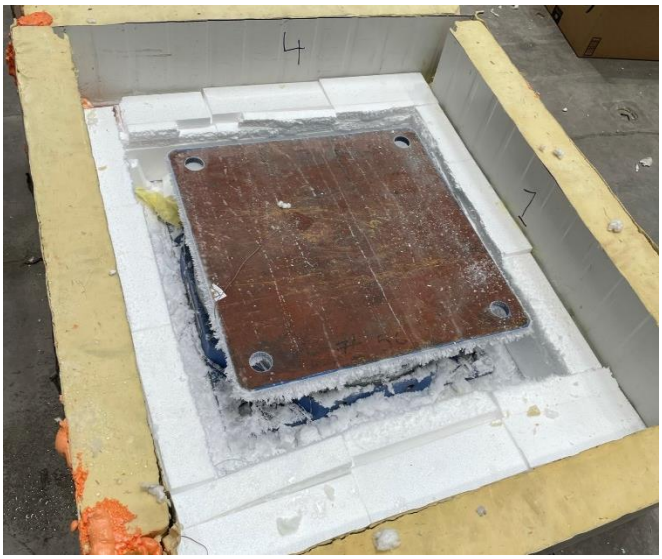

(c)

Figure 5.33. Amount of dry ice in second experiment after (a) 6 hours, (b) 11 hours & (c) 23 hours

5.6. Conclusions

Neither of the dry ice modelling approaches accurately represented the cooling capacity of dry ice. Temperature readings from sensors 6 and 7, from both tests, suggest that Source Term approach underestimated dry ice cooling capabilities, while Temperature BC approach overestimated dry ice cooling capacity. The temperature reached inside the bearing was not as low as the one predicted using Temperature BC approach for either test. The assumption that surface in contact with dry ice is at sublimation temperature was not accurate since only 3 out of 6 sensors registered temperatures close to sublimation on test 1 and none was close to sublimation on test 2.

The accuracy of the Source Term approach can be improved by modifying the source term to reflect the observed sublimation rate as a function of water temperature, i.e., increasing the rate when water is above or below freezing point, and decreasing the rate when water is at freezing point. A similar approach can be taken to calibrate Temperature BC approach, where the boundary conditions can be modified to a function that follows the readings from sensors 1, 2, 3, 4, 5 and 8.

In the freezing tests, phase change took about 2 and 4 hours. Hence, even with an accurate representation of dry ice cooling, if water phase change (energy for water to transform from liquid to solid) is not represented in the finite volume model, the time to reach target temperature prediction will always be inaccurate.

Chapter 6. Conclusions

Literature review revealed that a slow freezing process is required to achieve the maximum adhesive and cohesive ice strength. Once the ice is broken, friction coefficient may be higher than a clean bearing due to third body effects. Water lubrication increases the breakaway friction coefficient but decreases sliding friction coefficient when compared to a dry bearing.

Test set up and frame design was presented. The actual shear force in the frame is unknown as it will depend on how ice contamination affects the bearings frictional properties. To be conservative, the frame was designed for the shear force at the bearing displacement capacity.

The freezing tests revealed that big air spaces inside the box are likely to increase the dry ice consumption, making it harder to reach lower temperatures. However, the planned setup for the shake table test includes plates on top of the bearing connected to the A-frame and inherently no air gaps on top of the bearing.

The dry ice-filled insulation box can achieve the target temperature in the bearing within an acceptable – neither too short or too long – time frame. The higher dry ice consumption rate was observed during phase change, which was complete after 4-6 hours, time after which a consumption of about 50% of the initial amount of dry ice was observed. The slow freezing facilitated by dry ice is beneficial because it allows the interface to accommodate for differential thermal deformations, producing a stronger bond between ice and stainless steel in the concave surface.

When comparing the feezing tests with the finite volume model, Source Term approach turned out to be conservative, hence the source term value needs to be revised to account for the actual freezing rate. In contrast, Temperature BC approach proved to be unconservative, hence the temperature boundary condition value needs to be modified to the observed temperature for a more accurate representation. Phase change needs to be considered in the model for an accurate representation of reality. There is no important difference in freezing time for water initial temperature of 50°F (283°K) versus 68°F (293°K); hence, it is more practical to fill the bearing with water at room temperature.

Both experimental tests were conducted using an insulation layer on top and bottom of the bearing, reaching a minimum temperature of -50°F in the second test. Hence, insulation layers on top and bottom of the bearing will be included in the final insulation arrangement design. These insulation layers will be part of the load path, so they need to be of a material with good thermal properties and enough capacity to withstand axial and shear force produced during the shake table test, such as rubber or structural fiber glass reinforced polymer (FRP). Also, the effects of low temperature on the load cell are unknown, hence it is desirable to include an insulation layer below the bearing to avoid low temperatures in the load cell.

Air gaps in the insulation box will be minimized to avoid natural convection as much as possible and to keep the dry ice closer to the bearing. Polystyrene blocks proved to be an effective way to fill the air gaps inside the box. The insulation box will need to be filled with dry ice at least 8 to 12 hours prior to shake table test. Then, , after 4-6 hours, the insulation box will need to be refilled with about 50% of the initial dry ice amount.

References

American Association of State Highway and Transportation Officials. (1999). *Guide Specifications for Seismic Isolation Design*.

American Association of State Highway and Transportation Officials. (2010). *Guide Specifications for Seismic Isolation Design*.

American Institute of Steel Construction. *ANSI/AISC 360-10 Specification for structural steel buildings*. AISC, 2010.

American Institute of Steel Construction. (2005). *Steel Construction Manual. ANSI/AISC 360-16: Specification for structural steel buildings.* (n.d.).

Andrews, E. H., & Stevenson, A. (1978). Fracture energy of epoxy resin under plane strain conditions. *Composites, 10*(1), 49-50. doi:10.1016/0010-4361(79)90408-7.

Andrews, E. H., & Lockington, N. A. (1983). The cohesive and adhesive strength of ice. *Journal of Materials Science, 18*(5), 1455-1465. doi:10.1007/bf01111965.

ANSYS, Inc. (2016) ANSYS Fluent User's Guide, Release 17.2.

Bejan, A. (1993). *Heat Transfer*. John Wiley & Sons, Inc.

Bell's Travels Guide. (n.d.). Alaska Highway Road Log. https://www.bellsalaska.com/road%20logs/alaska-highway-log.pdf.

Benabdallah, H. S. (2007). Static friction coefficient of some plastics against steel and aluminum under different contact conditions. Tribology International, 40(1), 64-73.

Campbell, T. I., Pucchio, J. B., Roeder, C. W. and Stanton, J. F. (1991), "Frictional Characteristics of PTFE Used in Slide Surfaces of Bridge Bearings", Proc. 3rd World Congress on Joint Sealing and Bearing Systems for Concrete Structures, Toronto, Ontario, Canada, Vol. 2 of Preprints (published by the National Center for Earthquake Engineering Research, Buffalo, NY), 847-870.

Constantinou, M. C., Mokha, A. S. and Reinhorn, A. M. (1990), "Experimental and Analytical Study of a Combined Sliding Disc Bearing and Helical Steel Spring Isolation System", Report NCEER-90-0019, National Center for Earthquake Engineering Research, Buffalo, NY.

Constantinou, M. C., Tsopelas, P., Kim, Y-S. and Okamoto, S. (1993), " NCEERTaisei Corporation Research Program on Sliding Seismic Isolation Systems for Bridges:

Experimental and Analytical Study of a Friction Pendulum System (FPS), 404 Report NCEER-93-0020, National Center for Earthquake Engineering Research, Buffalo, NY.

Constantinou, M.C., Tsopelas, P., Kasalanati, A. and Wolff, E.D. (1999), "Property Modification Factors for Seismic Isolation Bearings", Report No. MCEER-99-0012, Multidisciplinary Center for Earthquake Engineering Research, Buffalo, NY.

Constantinou M. C., Whittaker A.S., Kalpakidis Y., Fenz D.M., Warn G.P. (2007). "Performance of Seismic Isolation Hardware under Service and Seismic Loading." Technical Rep. MCEER-07-0012. Multidisciplinary Center for Earthqueake Engineering Research, State Univ. of New York at Buffalo, NY.

Dolce, M, Cardone, D. and Croatto, F. (2005), "Frictional Behavior of Steel-PTFE Interfaces for Seismic Isolation," *Bulletin of Earthquake Engineering*, Vol.3, No. 1, 75-99.

Dosch, H., Lied, A., & Bilgram, J. (1995). Glancing-angle X-ray scattering studies of the premelting of ice surfaces. *Surface Science, 327*(1-2), 145-164. doi:10.1016/0039-6028(94)00801-9.

Eggert, H. and Kauschke, W (2002), Structural Bearings, Ernst & Sohn, Berlin, Germany.

Engineering ToolBox, (2004). Ice - Thermal Properties. Available at: https://www.engineeringtoolbox.com/ice-thermal-properties-d_576.html

Engineering ToolBox, (2004). Air - Specific Heat at Constant Pressure and Varying Temperature. Available at: https://www.engineeringtoolbox.com/air-specific-heat-capacity-d_705.html

Engineering ToolBox, (2009). Air - Thermal Conductivity. Available at: https://www.engineeringtoolbox.com/air-properties-viscosity-conductivity-heat-capacity-d_1509.html

Engineering ToolBox, (2018). Water - Thermal Conductivity. [online] Available at: https://www.engineeringtoolbox.com/water-liquid-gas-thermal-conductivity-temperature-pressure-d_2012.html

Fortin, G., Beisswenger, A., & Perron, J. (2010). Centrifuge Adhesion Test to Evaluate Icephobic Coatings. *AIAA Atmospheric and Space Environments Conference*. doi:10.2514/6.2010-7837.

Fortin, G., & Perron, J. (2012). Ice Adhesion Models to Predict Shear Stress at Shedding. *Journal of Adhesion Science and Technology, 26*(4-5), 523-553. doi:10.1163/016942411x574835.

Furukawa, Y., Yamamoto, M., & Kuroda, T. (1987). Ellipsometric study of the transition layer on the surface of an ice crystal. *Journal of Crystal Growth, 82*(4), 665-677. doi:10.1016/s0022-0248(87)80012-x.

Gillich, G. R., Iancu, V., Gillich, N., Korka, Z. I., Chioncel, C. P., & Hatiegan, C. (2018). Decoupling the structure from the ground motion during earthquakes by employing friction pendulums. *IOP Conference Series: Materials Science and Engineering, 294*, 012025. doi:10.1088/1757-899x/294/1/012025.

Golchin, A., Simmons, G., Glavatskih, S., & Prakash, B. (2013). Tribological behaviour of polymeric materials in water-lubricated contacts. *Proceedings of the Institution of Mechanical Engineers, Part J: Journal of Engineering Tribology, 227*(8), 811-825. doi:10.1177/1350650113476441.

Hwang, J.S., Chang, K.C. and Lee, G.C. (1990) Quasi-static and dynamic characteristics of PTFE-stainless interfaces. Journal of Structural Engineering 116(10), 2747–2762.

Jia, J., Chen, J., Zhou, H., Hu, L., & Chen, L. (2005). Comparative investigation on the wear and transfer behaviors of carbon fiber reinforced polymer composites under dry sliding and water lubrication. *Composites Science and Technology, 65*(7-8), 1139-1147.

Jordaan, I. J., & Timco, G. W. (1988). Dynamics of the Ice-Crushing Process. *Journal of Glaciology, 34*(118), 318-326. doi:10.3189/s0022143000007085.

Kauschke, W. and Baigent, M. (1986), "Improvements in the Long Term Durability of Bearings in Bridges, Especially of PTFE Slide Bearings", *Proc. 2nd World Congress on Joint Sealing and Bearing Systems for Concrete Structures,* American Concrete Institute, Detroit, Michigan, Publication SP-94, Vol. 2, 577-612.

Kietzig, A., Hatzikiriakos, S. G., & Englezos, P. (2010). Physics of ice friction. *Journal of Applied Physics, 107*(8), 081101. doi:10.1063/1.3340792.

Long, J. E. (1969), "The Performance of PTFE in Bridge Bearings", Civil Engineering and Public Works Review, UK, May, 459-462.

Long, J. E. (1974), *Bearings in Structural Engineering*, J. Wiley & Sons, New York.

Makkonen, L. (2012). Ice Adhesion —Theory, Measurements and Countermeasures. *Journal of Adhesion Science and Technology, 26*(4-5), 413-445. doi:10.1163/016942411x574583.

Makkonen, L., & Tikanmäki, M. (2014). Modeling the friction of ice. *Cold Regions Science and Technology, 102*, 84-93. doi:10.1016/j.coldregions.2014.03.002.

Marmo, B. A., Blackford, J. R., & Jeffree, C. E. (2005). Ice friction, wear features and their dependence on sliding velocity and temperature. *Journal of Glaciology, 51*(174), 391-398. doi:10.3189/172756505781829304.

Mens, J., & Gee, A. D. (1991). Friction and wear behaviour of 18 polymers in contact with steel in environments of air and water. *Wear, 149*(1-2), 255-268.

Mokha, A., Constantinou, M. C. and Reinhorn, A. M. (1988), "Teflon Bearings in Aseismic Base Isolation: Experimental Studies and Mathematical Modeling", Report NCEER-88-0038, National Center for Earthquake Engineering Research, Buffalo, NY.

Mokha, A. S., Constantinou, M. C. and Reinhorn, A. M. (1990), "Experimental Study and Analytical Prediction of Earthquake Response of a Sliding Isolation System with a Spherical Surface", Report NCEER-90-0020, National Center for Earthquake Engineering Research, Buffalo, NY.

Negussey, D., & Anasthas, N. (2001, December). Young's modulus of EPS geofoam by simple bending test. In 3rd international conference on geofoam blocks in construction applications, Salt Lake City, USA (pp. 10-12).

Nord Lock Group. (n.d.). *The experts: Thread engagement in a tapped hole*. Nord. https://www.nord-lock.com/insights/bolting-tips/2015/the-experts-thread-engagement-in-a-tapped-hole/.

Petrenko, V. F., & Whitworth, R. W. (1999). Adhesion and Friction. In *Physics of ice* (pp. 314-318). Oxford: Oxford University Press.

Raraty, L. E., & Tabor, D. (1958). The adhesion and strength properties of ice. Proceedings of the Royal Society of London. Series A, Mathematical and PhysicalSciences, Vol. 245, No. 1241, pp 184-201. doi:10.1016/0043-1648(59)90092-4.

State of Alaska Department of Transportation and Public Facilities. (2017, February 23). 2017 Bridge Inventory Report. https://dot.alaska.gov/stwddes/desbridge/assets/pdf/2017bridgeinventory.pdf.

Sukhorukov, S., & Marchenko, A. (2014). Geometrical stick–slip between ice and steel. *Cold Regions Science and Technology, 100*, 8-19. doi:10.1016/j.coldregions.2013.12.007.

Tappan Zee Constructors (2017). FPT Bearing QC Inspection Report: Proof Testing of Affected Bearings.

Taylor, M. E. (1972), "PTFE in Highway Bridge Bearings", Report LR 491, Transport and Road Research Laboratory, Department of the Environment, UK.

Tsopelas, P., Constantinou, M. C., Kim, Y-S. and Okamoto, S. (1996), "Experimental Study of FPS System in Bridge Seismic Isolation", *Earthquake Engineering and Structural Dynamics*, Vol. 25, 65-78.

Velkavrh, I., Lungevičs, J., Jansons, E., Klien, S., Voyer, J., & Ausserer, F. (2019). The Influence of Isotropic Surface Roughness of Steel Sliders on Ice Friction Under Different Testing Conditions. *Lubricants, 7*(12), 106. doi:10.3390/lubricants7120106.

Wang, J., Yan, F., & Xue, Q. (2009). Tribological behavior of PTFE sliding against steel in sea water. *Wear, 267*(9-10), 1634-1641.

WSDOT Bridge and Structures (2015). SR522 Seismic Isolation Bearings.

Zhao, G., Ma, Y., Li, Y., Su, L., & Zhou, F. (2019). An Experimental Study on the Behavior Deterioration Trend of Friction Pendulum Bearings with Corrosion Time for Offshore Isolated Bridges. *IOP Conference Series: Earth and Environmental Science*, 304, 042025.